Fabrication of ferroelectric based MEMS structures for electronically switchable bulk acoustic wave resonators

By Tian Le Wang

This thesis is submitted to Materials Department, Imperial College London for the degree of Doctor Of Philosophy

Feburary 2014

Abstract

The thesis describes the research carried out into fabrication of multilayer microwave capacitance structure with ferroelectric films in paraelectric state; and confirmation of the possibility to develop on their base an electronically switchable bulk acoustic wave (BAW) resonator. Different eigenmodes of acoustic resonances can be excited and switched electronically through the application to ferroelectric layers of the resonator unidirectional or oppositely directed dc biased electric fields..

The resonator was fabricated out of a $SrRuO_3/SrTiO_3/SrRuO_3/YSZ$ multilayer structure deposited on top of Si substrate. Pulsed Laser Deposition, Magnetron Sputtering, Photolithography, Argon Ion Beam Milling, and Reactive Ion Etching were the fabrication methods used to make this resonator.

This novel device is a demonstrator that will contribute to the telecommunications industry's demand for flexibility in both microwave frequency switching and tuning. The Si MEMS concept of this resonator allows easy circuit board integration into many electronics products.

Preface

This thesis is the author's own work and is submitted for the degree of Doctor of Philosophy at Imperial College London.

Parts of this thesis have either been published, presented at conferences,accepted for publication or are in the preparation for submission.

T.Wang; P.K.Petrov; N.M.Alford; A.K.Mikhaylov; S.V.Ptashnik; S.V.Zinoviev and A.B.Kozyrev, *Electronically switchable bulk acoustic wave resonator based on paraelectric state ferroelectric films.* Electronics Letters, 2011. **47**(24)

T.Wang; P.K. Petrov and N.M. Alford, *Deep reactive ion etching of silicon for MEMS applications*, Poster Presenation at VS3 Nanostructured Metal Oxide Thin Films, Coventry, UK 2012

T.Wang; P.K. Petrov and N.M. Alford, *Alternative deep reactive ion etching of silicon using metal masks.* MRS Conference 2012 Symposium DD, Boston, USA

P.K.Petrov;T.Wang;N.M.Alford A.K.Mikhaylov; S.V.Ptashnik; S.V.Zinoviev and A.B.Kozyrev, *Free-standing nanoscale functional oxides multlilayer structure for electronically switchable bulk acoustic wave resonators.* EMRS Conference 2013 Symposium H, Strasbourg, France

T.Wang; P.K.Petrov and N.M.Alford, *Alternative deep reactive ion etching of silicon using metal masks.* Journal of Micromechanics and Microengineering, 2014

The copyright of this thesis rests with the author and is made available under a Creative Commons Attribution Non-Commrcial No Derivative license. Researchers are free to copy, distribute or transmit the thesis on the condition that they attribute it, that they do not use it for commercial purposes and that they do not alter, transform or build upon it. For any reuse or redistribution, researchers must make clear to others the license terms of this work.

Table of Contents Page

Abstract 2

Preface 3

Figure Contents 6

Table Contents 10

Acronyms 12

Acknowledgements 14

Chapter 1. Introduction 15

1.1 Introduction and Motivation 15

1.2 Thesis Facts Known and Unknown 17

1.3 Thesis Overview 17

1.4 Original Contributions 18

Chapter 2. Literature Review 19

2.1 Basic Ferroelectric Properties 19

2.2 Bulk Acoustic Wave Resonator 32

2.2.1 State of Art of Ferroelectric Materials in BAW Resonators 35

2.2.3 Types of Bulk Acoustic Wave Resonators 42

2.2.4 BAW Device Performance Requirements 45

2.3 Dielectric Acoustic Wave Resonator 49

2.4 Fabrication Technologies 54

2.4.1 Magnetron Sputtering 54

2.4.2 Pulsed Laser Deposition 56

2.4.3 Silicon Substrate Patterning 58

2.4.4 Device Patterning 61

2.5 Characterisation Techniques 65

2.5.1 Optical Microscopy 65

2.5.2 Scanning Electron Microscopy 66

2.5.3 X-Ray Diffraction 68

2.5.4 Profilometry 70

2.5.5 Electrical Characterisation 72

2.6 Conclusion 84

Chapter 3. Deposition and Characterisation of Thin Film Multilayer Structure 85

3.1 Processing Overview 85

3.2 Deposition of 8 mol% Yttria Stablized Zirconia(YSZ) buffer layer by Pulsed Laser Deposition 87

3.3.1 Deposition of Strontium Ruthenate ($SrRuO_3$) Electrodes by Pulsed Laser Deposition 89

3.3.2 Electrical properties of the Strontium Ruthenate thin films 94

3.4.1 Deposition of Strontium Titanate ($SrTiO_3$) Active Layer by Pulsed Laser Deposition 94
3.4.2 Tunability vs. Frequency Measurement Results 98
3.5 Metal Layer Deposition 100
3.6 Conclusions 101

Chapter 4. Deep reactive ion etching of Silicon 102
4.1 Optimisation of the Si reactive ion etching process 102
4.2 Choice of the masking material for Si reactive ion etching 109
4.3 Conclusions 115

Chapter 5. Fabrication of a ferroelectric based tunable thin-film bulk acoustic wave resonator 116
5.1 Device Design 116
5.2 Device Mask Design 117
5.3 Resonator Patterning 119
5.3 Resonator device measurement results 123
5.4 Conclusions 127

Chapter 6. Theory and Device Operation 128
6.1 Theory and Device Operation of One Stacking Structure 128
6.1.1 Introduction 128
6.1.2 Theory of field dependent acoustic resonances 129
6.1.3 Theory of field dependent piezoelectric constitutive equations 132
6.1.4 Series and Parallel Resonance 133
6.2 Device Operation of Two Stacking Structure 135
6.3 Conclusion 136

Chapter 7. Conclusion and Future Works 137

References 138

Appendix I. 145
Modeling of the Resonator Device 145

Figure Contents

Figure 2.1.The crystallography structure of ABO3 type material an the unit cell response to external electric field.....20

Figure 2.2.The classification of the ferroelectric materials from the general class of dielectrics.....21

Figure 2.3.Temperature dependence of the relative dielectric constant of a ferroelectric material and different responses to electric field in ferroelectric and paraelectric states.....22

Figure 2.4.Temperature dependence of the loss tangent at zero biasing field for single crystal Strontium titanate at microwave frequencies.....23

Figure 2.5.Variation of dielectric constant and loss factor with frequency of an AC electric field.....26

Figure 2.6.The model of the interfacial dead layer within a ferroelectric device and the dependence of dielectric properties on the thickness of BST50/50 thin films.....28

Figure 2.7.The bias induced resonant dips observed in BST50-50 based capacitors from 0V-20V.....30

Figure 2.8.Electrical input impedance of a BAW resonator.....35

Figure 2.9 The DC bias dependence of a resonant frequency and reflected power corresponding to states (on and off) at T=52K and DC field of 1.2kV/cm.....40

Figure 2.10.The relationship between Curie temperature and Ba concentration for BST ceramic and single crystals and Temperature dependence of dielectric constant of BST ceramic for different Ba concentrations.....41

Figure 2.11.Thin film acoustic resonator setup and Solidly mounted resonator topology.....43

Figure 2.12.Thickness mode and Contour mode acoustic wave resonators.....45

Figure 2.13.Excitation of wavefronts inside a resonant cavity.....46

Figure 2.14.Potential applications of ferroelectric materials.....53

Figure 2.15.Commercial applications relating to SAW, BAW and Temperature Compensated SAW technologies.....53

Figure 2.16. Difference between the DC and RF magnetron sputtering system and the schematic of the magnetron sputtering system.....55

Figure 2.17.Electrical resistivity vs. Argon pressure for sputtered titanium films and Zone model showing the influence of argon pressure and substrate temperature on the microstructure of metal thin films.....56

Figure 2.18.The instrument setup of a pulsed laser deposition system.....57
Figure 2.19.Growth temperature Td, thickness t and lattice parameters a of the multilayer structure.....58
Figure 2.20. Difference between the wet etching and dry etching techniques.....58
Figure 2.21. The system schematic of reactive ion etcher and inductively coupled plasma etcher.....60
Figure 2.22. Results of deep silicon etching from different etching processing conditions.....61
Figure 2.23.Contact, proximity and projection alignment systems.....62
Figure 2.24. Ion beam milling system schematic.....63
Figure 2.25. The etching rate of different materials vs. the angle of incidence during ion beam milling.....64
Figure 2.26.Ion beam etching rate of different materials and Kaufman type ion beam etching system.....64
Figure 2.27. The schematic of transmission and reflection optical microscope.....65
Figure 2.28. Si transmission improves with wafer thinning and P-type doped Si transmission decreases with increasing carrier concentration.....66
Figure 2.29.Schematic diagram of a scanning electron microscope.....68
Figure 2.30. XRD diffraction pattern for STO and BST films grown at 400 °C and 500°C.....69
Figure 2.31. An X-ray beam scan process and relationship to Bragg's Law.....69
Figure 2.32. The schematic setup of a contact stylus profilometer.....71
Figure 2.33.Different types of ferroelectric capacitors.....73
Figure 2.34. Coplanar transmission line structures patterned on ferroelectric film.....74
Figure 2.35. Frequency range applicability for each measurement techniques and the associated instrumental error/limits.....75
Figure 2.36. Setup for current voltage measurement.....76
Figure 2.37. Four point probe method of measuring resistivity of a specimen and the electrical field and equipotential line distribution on the sample during four point probe technique.....77
Figure 2.38. Different measurement techniques used for different frequency ranges.....78

Figure 2.39.The different measurement configurations for different impedance samples.....79
Figure 2.40. Simplified diagram of the RF I-V technique setup.....80
Figure 2.41. The two types of capacitance measurement circuit modes-Parallel and Series Equivalent mode.....80
Figure 2.42. Setup for capacitance voltage measurement and the calibration standards for measurements.....81
Figure 2.43. Circuit model used to characterized the resonator performance.....81
Figure 2.44. The Open/Short/Load compensation for RF IV measurement.....82
Figure 2.45. One port measurement setup for resonator device characterisation....83
Figure 2.46. The calibration standard values for network analyzer in Vector impedance plane and Smith Chart.....84
Figure 3.1. The fabrication process of the bulk acoustic wave resonator.....85
Figure 3.2. Crystal structure of Yttria Stabilized Zirconia.....88
Figure 3.3. X-ray 2θ diffraction pattern of YSZ on Si substrate with native oxide and Si substrate with HF etching treatment.....89
Figure 3.4. The orthorhombic crystal structure of SrRuO3 with lattice parameters.....91
Figure 3.5. Schematic drawing of the rectangle on cube epitaxial relation of SRO on YSZ.....91
Figure 3.6. X-ray 2θ diffraction pattern of SRO on Si substrate.....93
Figure 3.7. X-ray 2θ diffraction pattern of SRO on YSZ buffered Si substrate.....93
Figure 3.8. The current voltage curve for the bottom electrode deposited directed on silicon substrate and deposited on YSZ buffered silicon substrate.....94
Figure 3.9. X-ray 2θ diffraction pattern of STO thin films grown on SRO electrodes on Si substrate at different substrate temperature and at a constant oxygen partial pressure.....96
Figure 3.10. X-ray 2θ diffraction pattern of STO thin films grown on SRO electrodes on Si substrate at different oxygen partial pressure and at a constant substrate temperature and an enlarged comparison XRD graph at STO (110) peak.....97
Figure 3.11. X-ray 2θ diffraction pattern of STO thin films grown on SRO electrodes on YSZ buffered Si substrate at 850°C and 150mTorr O2 partial pressure.....98
Figure 3.12. The capacitance-voltage behaviour of the resonator device at various frequencies with applied voltage from-2V to 2V.....99

Figure 3.13. Frequency vs. Tunability of the 300nm SRO/500nm STO /300nm SRO/10nm YSZ on Si multilayer structure 99
Figure 4.1. Etch rates of Silicon vs Pressure under CF_4 plasma.....103
Figure 4.2. Etch rates of Silicon vs Pressure under Argon plasma.....103
Figure 4.3. Etch rates of Silicon vs Pressure under CF_4(25%)+Ar(75%) plasma mixture.....104
Figure 4.4. Etch rates of Silicon vs Pressure under CF_4(50%)+Ar(50%) plasma mixture.....104
Figure 4.5. Etch rates of Silicon vs Pressure under CF_4(75%)+Ar(25%) plasma mixture.....105
Figure 4.6. Etch rates of Silicon vs Pressure under CF_4 at 100V RF bias.....106
Figure 4.7 Etch rates of Silicon vs Addition of Oxygen in CF_4(25%)+Ar(75%) plasma mixture at 60Pa 108
Figure 4.8 Etch rates of Silicon vs Addition of Oxygen in CF_4(75%)+Ar(25%) plasma mixture at 60Pa 108
Figure 4.9 Etch rates of Silicon vs Pressure in CF_4(40sccm)+Ar(10sccm)+O_2(5sccm) plasma mixture at 100V RF bias 109
Figure 4.10. The chemical and physical reactions occurring during the etching process.....110
Figure 4.11. The mask fabrication processing route.....110
Figure 4.12. The relationship between Electronegativity and the silicon etching rate.....112
Figure 4.13. The SEM images of Si etching profiles using different masking multilayer structures.....113
Figure 4.14. X-ray diffraction pattern of the multilayer structure before and after the backside etching process.....114
Figure 5.1. Bulk acoustic wave resonator configuration.....116
Figure 5.2. Microscopic image of the bottom electrode pattern.....117
Figure 5.3. Microscopic image of the ferroelectric layer pattern.....118
Figure 5.4. Microscopic image of the top electrode pattern.....118
Figure 5.5. Microscopic image of the substrate backside etching pattern.....119
Figure 5.6. Microscopic image of the bottom electrode layer patterning on the SRO+YSZ layer.....120

Figure 5.7. Microscopic image of the active layer patterning on the STO+SRO+YSZ layer.....120
Figure 5.8. Microscopic image of the top electrode layer patterning on the SRO+STO+SRO+YSZ layer 121
Figure 5.9. Microscopic image of the silicon substrate backside patterning on the silicon substrate.....122
Figure 5.10. Microscopic image of the three different active area dimensions and final device structure 50×50μm after photolithography patterning and ion beam milling steps.....123
Figure 5.11. The capacitance voltage and current voltage measurement at different frequencies for the entire resonator device after silicon substrate backside etching.....124
Figure 5.12. The capacitance frequency measurement from the one port reflection setup compared with modelling.....125
Figure 5.13. Results of phonon transport theory.....126
Figure 6.1. Layout of the one stacking structure for FBAR resonator.....129
Figure 6.2. Simplified cross section (a) and two terminal equivalent circuit of a tunable FBAR as a frequency selective switch.....130
Figure 6.3. The series resonant circuit diagram and the parallel resonant circuit diagram.....134
Figure 6.4. The series frequency response and the parallel frequency response.....134
Figure 6.5. Layout of the two stacking structure for the electronically switchable FBAR resonator.....136

Table Contents

Table 2.1.Comparison between the ferroelectric materials and piezoelectric materials in terms of mechanical and electrical properties.....32

Table 2.2.Summary of dielectric properties measurements reported for STO and BST thin films.....36

Table 2.3.Summary of various ferroelectric materials based tunable FBARs.....38

Table 2.4.Comparison of different technologies for microwave devices.....52

Table 2.5.Typical Specifications of a Stylus Profiler.....72

Table 3.1. Growth conditions for each layer within the multilayer structure for the bulk acoustic wave resonator.....86

Table 3.2. Physical properties of the materials used in the pulsed laser deposition...92

Table 3.3. The sputtering conditions for different metal mask materials.....100

Table 4.1. The etch rates of Si and different masking materials.....111

Table 4.2. The etching rates of different multilayer masking structures against the reactive plasma.....113

Table 5.1. The experimental parameters for etching the ferroelectric materials....122

Acronyms

AC	Alternating Current
BAW	Bulk Acoustic Wave
BSE	Backscattered Electrons
BST	Barium Strontium Titanate
BTO	Barium Titanate
DC	Direct Current
DUT	Device Under Test
EHF	Extremely High Frequency
FBAR	Film Bulk Acoustic Wave Resonator
GPS	Global Positioning System
GSG	Ground Signal Ground
HRS	High Resistive Silicon
IC	Integrated Circuit
ICP	Inductively Coupled Plasma
LAO	Lanthanum Aluminate
MEMS	Micro-electro-mechanical Systems
NA	Numerical Aperture
PLD	Pulsed Laser Deposition
RF	Radio Frequency
RIE	Reactive Ion Etching
SAW	Surface Acoustic Wave
SDA	Semiconductor Device Analyzer
SE	Secondary Electrons
SEM	Scanning Electron Microscope
SHF	Super High Frequency
SMR	Solidly Mounted Resonator
SRO	Strontium Ruthenate
STO	Strontium Titanate

TFBAR	Thin Film Bulk Acoustic Wave Resonator
UHF	Ultra High Frequency
UMTS	Universal Mobile Telecommunications System
UV	Ultraviolet
WLAN	Wireless Local Area Network
XRD	X-ray Diffraction
YSZ	Yittria Stabilized Zirconia

Acknowledgements

I would like to thank my supervisor Professor Neil Alford for allowing me to join his group to carry out this PhD project together with the endless support and guidance towards me throughout this project.

I would like to especially thank my supervisor Dr.Peter Petrov for the advice, encouragement and support regarding the experimental work of this research project.

I would like to thank Professor Andrey Kozyrev for providing the theorectical concept of this research. Without this, my PhD project would have never occurred.

I would like to thank Dr. Bin Zou for the invaluable discussions and tutoring relating to the fabrication and characterisation issues occurred during this project.

I would like to express my thanks to Dr. Peter Gammon, Dr.Sean McMitchell, Jing Pang, Evgeniy Donchev,Clementine Walker, Laurentiu Braic. This work would not have been possible without the help and support from all the students and staff in the Thin Film Technology Lab.

Finally I would like to sincerely thank my parents Jianxun Wang and Suzhen Wang for their constant support and guidance. I would like to thank my girlfriend Baoli He for her everlasting love and moral support through the best and worst times of my PhD research at Imperial College London.

Tianle Wang

London,UK

Januray 2014

Chapter 1. Introduction

This introductory chapter is to provide the overview of thesis and motivation for the work presented.

1.1 Introduction and Motivation

The evolution of wireless communication systems in recent years has been accelerating at an extraordinary pace. This is mainly due to the increasing public demand for greater functionality while demanding a reduction in size and cost. The modern smart phone of Apple Inc. known as the iPhone has been the revolutionary product of the 21st Century and the competition in this market has only intensified with time. This is where research in the reconfigurable technologies such as Multi-frequency band and multi-mode cellular networking, GPS and WLAN connectivity can expect to answer the questions posed by current and future demands. For example, most mobile phones nowadays operate on the third generation (3G) with higher data rate services for video calls, mobile internet access and mobile TV. These smart mobile phones with 3G capability are required to operate over the global UMTS frequency bands of 850/900/1700/1900/2100MHz and fulfil the GPS standards of 1.5GHz bands and WiFi in the 2.4/5.0GHz bands. With the newly developed successor- the fourth generation(4G) being gradually integrated into future wireless mobiles and computers, it is highly desirable to provide multi-frequency band and multi-mode wireless devices with increased data transfer speeds using a single hardware device. This also presents a difficult challenge to integrate this technology with elegant designs and cost effective materials for mass commercial production. Therefore by using a single electronically tunable device to replace several wireless transceivers will bring a massive cost savings.

The microwave resonator is based on the excitation of an electromagnetic wave and is a part of many devices such as filters, oscillators, amplifiers and frequency meters. The size of these devices is directly related to the wavelength of electromagnetic wave at a certain frequency, which is also related to the propagation velocity of the electromagnetic wave at the same time. The main goal of designing microwave devices are concentrated at achieving high performance with small size and integrated with different devices on one chipset. The resulting size of microwave resonators at RF/Microwave frequencies is a big limitation for integration of portable communication systems. The acoustic resonator is an elgant solution to these

limitations due to advantages like lower propagation velocity, smaller size and integrated circuits compatibility compared to the electromagnetic wave resonators.

The unique property of the ferroelectric materials such as electric field dependent permittivity and relatively low loss at microwave frequencies have made them promising candidates for electrically tunable RF and microwave devices in the wireless communication application. Ferroelectric materials are widely used in tunable microwave components such as tunable resonators, variable capacitors, phase shifters and filters.

This thesis proposes to use ferroelectric thin films for novel switchable and tunable bulk acoustic wave resonators at RF and microwave frequencies. The main focus of this thesis is to fabricate a novel type of thin film bulk acoustic wave resonator(TFBAR) on Si substrate using a MEMs setup and characterisation of ferroelectric thin films at microwave frequencies. The free standing TFBAR resonator will consist of single multilayer structure consisting of $SrRuO_3/SrTiO_3/SrRuO_3/YSZ$ deposited on the silicon substrate. The multilayer structure will be grown by PLD technique and an air cavity will be etched through the substrate using metal mask assisted dry etching method to create the free standing structure. The switchable and tunable characteristics of this resonator are based on the field dependent behaviour of the ferroelectric material in paraelectric state under DC bias. In current switchable and tunable microwave devices, external switches and varactors are required for frequency tuning, which results in increased loss in the path of RF signal, circuit design complexity and cost. Thus, by successfully fabricating prototypes of these intrinsically tunable resonators, we can contribute to the design and production of energy saving, cost effect and compact microwave systems. The principle of operation has been theoretically demonstrated recently by our colleagues from Professor Andrey Kozyrev's group from St.Petersburg State Electrotechnical University (LETI).[1]

The thesis presents the fabrication of the $SrRuO_3/SrTiO_3/SrRuO_3/YSZ$ multilayer structure on the silicon substrate, the development of a new alternative etching method for the silicon substrate and combining the deposition of the multilayer structure and the silicon etching technique to develop a novel TFBAR.

1.2 Thesis Facts Known and Unknown

Facts Known	Facts Unknown
Pulsed Laser Deposition Conditions for SRO/STO/SRO/YSZ stack on Si substrate	How to make tunable BAW resonator in terms of deposition of multilayer stack?
Deep Reactive Ion Etching Conditions for fabricating free standing TFBARs on Si substrate	How to etch silicon substrate fast enough without ICP(Inductively Coupled Plasma)?
Masking Material Selection for etching through Si substrate	Which materials could be used as a resist?
Ferroelectric Material Selection for Tunable Bulk Acoustic Wave Resonator	How to protect the device side while maintain the functionality?
Design of the electrode structure for Tunable Bulk Acoustic Wave Resonator	Electrostriction are negative in terms of microwave losses, nobody utilized these materials for tunable BAW applications

1.3 Thesis Overview

The organization of the thesis is as follows.

Chapter 2 presents the background to concept of ferroelectricity, introduces the ferroelectric material system used for tunable microwave applications and reviews the fabrication and characterisation techniques involved in this project.

Chapter 3 details the fabrication and electrical characterisation of the YSZ/SRO/STO/SRO multilayer sturcutre on Si substrate. The influence of the PLD deposition conditions on the growth of epitaxial STO thin films has been studied.

Chapter 4 describes an alternative Si deep etching method using metal masking materials developed to form a free standing MEMS structures. A Si etching rate of 11μm/min was achived using etching mixture of CF_4(40sccm)+Ar(10sccm) +O_2(5sccm) at 60Pa pressure and 100V RF bias voltage and metal masking layers of 100nm Au/100nm Ti/100nm Au/100nm Ti.

Chapter 5 presents the design, the fabrication and the electrical performance measurement of an electronically switchable bulk acoustic wave resonators based on the ferroelectric MEMS structures.

Chapter 6 presents the theory of the single layer device as presented in the thesis and the desired two layer device. The device operation are explained qualitatively and final device layout is presented.

Chapter 7 concludes the thesis and outlines the directions for future work.

1.4 Original Contributions

This thesis has presented original contributions to knowledge of tunable ferroelectrics thin films for microwave applications. The summary of these contributions is listed below:

1. The processing conditions were established for epitaxial growth of Strontium Titanate/Strontium Ruthenate multilayer thin films on high resistive Silicon substrate by pulsed laser deposition.
2. A novel alternative Silicon deep etching method using reactive ion milling was established. This method demonstrates the possible incorporation in the device fabrication of the MEMs system.
3. A novel free standing functional oxides multilayer structure for electronically switchable bulk acoustic wave resonator was proposed and fabricated on highly resistive Silicon substrate using pulsed laser deposition.

Chapter 2. Literature Review

This chapter gives an overview of the tunable microwave technologies and a general background introduction into the ferroelectric materials with detailed description of their dielectric, piezoelectric and acoustic properties. The current status and prospects are also reviewed. Various fabrication techniques are reviewed together with structural and electrical characterization to establish the relationship between processing parameters and material performance.

2.1 Basic Ferroelectric Properties

In 1921, Ferroelectricity was discovered by Joseph Valasek during an investigation of the dielectric properties of the Rochelle Salt ($NaKC_4H_4O_6 \bullet 4H_2O$) and demonstrated the polarisation hysteresis with electric field and the temperature dependence.[2] Since then the number of known ferroelectric materials has rapidly increased. Most of the useful ferroelectric materials belong to the perovskite family, which is characterised by the chemical formula ABO_3. Figure 2.1 shows the cubic cell structure of the ABO_3 type materials, with A^{2+} ions at the corner, B^{4+}ions at the centre of the octahedral and O^{2-}ions at the face centres of the cube. This perovskite ABO_3 structure allows variable compositions by substituting on the A or B sites with compatible ions. When an external electric field is applied, both B^{4+}cation and O^{2-}cation shift from their equilibrium positions and form electric dipoles shown in Figure 2.1. This shift leads to the polarisation of the material under electric field and the shape of the unit cell is elastically deformed, which known as the Electrostriction effect. In contrast to the common converse piezoelectric effect, electrostriction is present in all dielectric materials and the deformation strain has a quadratic dependence on the magnitude of the applied electric field. Although the value of piezoelectricity induced by electrostriction effect may be small compared to the piezoelectricity in crystalline materials, they may be quite large in ferroelectric materials.

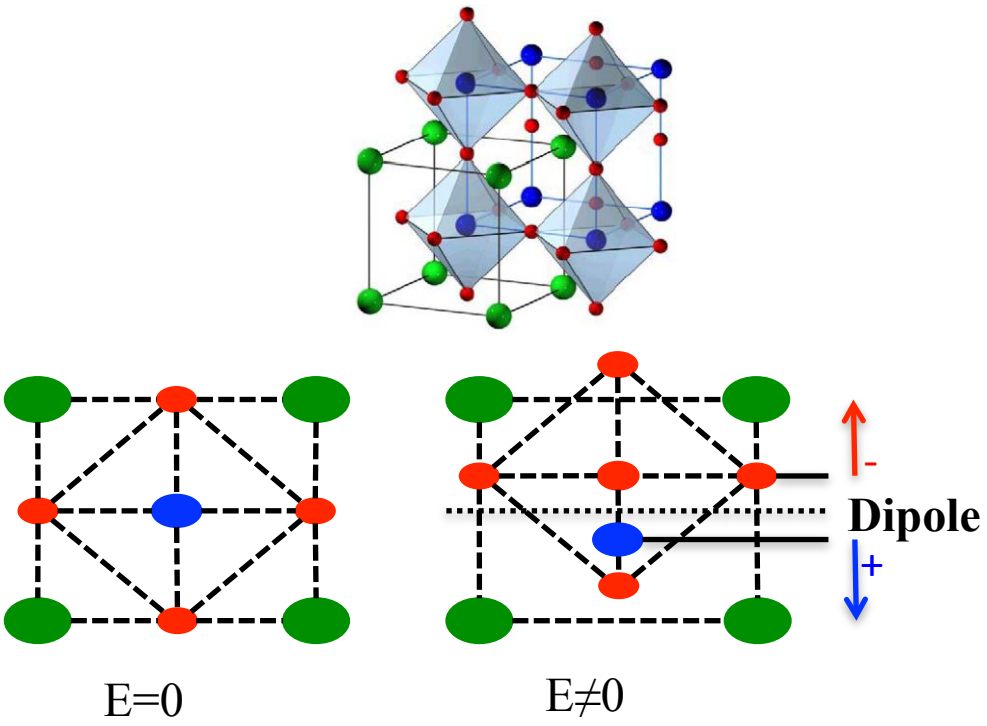


Figure 2.1. The crystallography structure of ABO_3 type material and the unit cell response to external electric field (Green-A, Blue-B, Red-O)

From the crystal symmetry, all of the crystal structures can be separated into 32 crystallographic point groups and only 11 of them are centrosymmetric. Centrosymmetric means the crystal contains a center of symmetry that inhibits any polar properties from the crystal.[3] The other 21 crystallographic point groups are all non-centrosymmetric and allow the crystal to contain one or more polar axes. All but one these non-centrosymmetric structure exhibit piezoelectricity described as a coupling between the electrical and mechanical energies. Piezoelectricity is linear with the applied electric field, so the piezoelectric response is reversed with the sign of the electric field is changed. 10 out of the 20 piezoelectric crystal point groups contains an unique polar axis and named as the polar crystals, because they posses a spontaneous polarization in absence of an external electric field. The spontaneous polarization is temperature dependent and its existence can be detected by observing the flow of charges to and from the surfaces on change of temperature. This known as the pyroelectric effect and the crystals with this effect are called pyroelectrics. A subgroup of the pyroelectrics is the ferroelectrics, which are polar materials that the direction of the spontaneous polarization can be switched by an external electric field. This classification is shown in Figure 2.2.

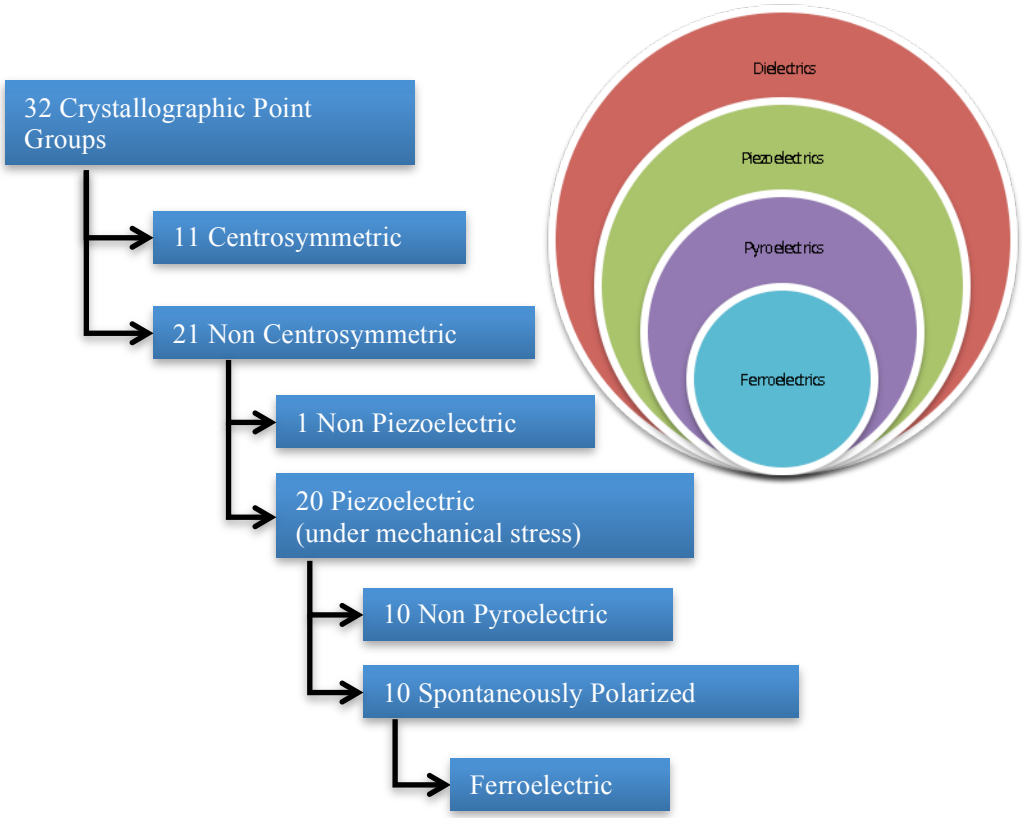


Figure 2.2. The classification of the ferroelectric materials from the general class of dielectrics

The piezoelectricity phenomenon was discovered in the 80s by the brothers Jacques and Pierre Curie[4]. The direct piezoelectric effect is the ability to induce an electrical polarization by the applied mechanical stress in crystals of certain categories. The converse piezoelectric effect is the production of a mechanical stress through the application of an electric field. The piezoelectricity phenomenon is reversible and expresses a linear interaction between mechanical and electrical domains in a single elastic body. The relationship is mathematically correlated as below, [5]

$$S=s^{E}T+d^{T}E \qquad (2.1)$$

$$D=dT+\varepsilon^{T}E \qquad (2.2)$$

where S is strain, s is compliance, T is stress, D is electric displacement, d is piezoelectric coefficient, ε is permittivity, E is electric field strength.

Ferroelectric materials are a subset of the dielectric materials, which exhibit a reversible spontaneous polarization within a certain temperature range. The spontaneous polarization is temperature dependent and deceases with increasing temperature to disappear above a phase transition temperature known as the Curie

point T_c. The ferroelectric material is in the paraelectric state when the temperature is above the Curie point T_c and exhibits a cubic structure. When the temperature is below T_c, the crystal structure experiences a slight deformation, the centre of positive charges and negative charges does not coincide, so the electric dipoles are formed and spontaneous polarisation occurs in the ferroelectric state. There is also a rapid decrease in the dielectric constant with further increasing the temperature after the Curie point T_c and it follows the Curie-Weiss relationship.[6]

$$\varepsilon_r = \frac{C}{T-T_0} \quad (T>T_c) \qquad (2.3)$$

where C is the Curie-Weiss constant, T_0 is the Curie-Weiss temperature (normally below T_c, only equal to T_c for a continuous transition). The temperature effect on the dielectric constant and polarization and dielectric constant responses to applied electric field for ferroelectric phase transition to paraelectric phase are shown in Figure 2.3. Tunable ferroelectric based devices should operate slightly above their Curie temperature point in the paraelectric phase, because it retains a less dispersive permittivity at microwave frequencies and low hysteresis effect. In Figure 2.4, the microwave losses in single crystal strontium titanate is shown to be controlled not only by the bias field, but also sensitive to the temperature changes in the surrounding environment.

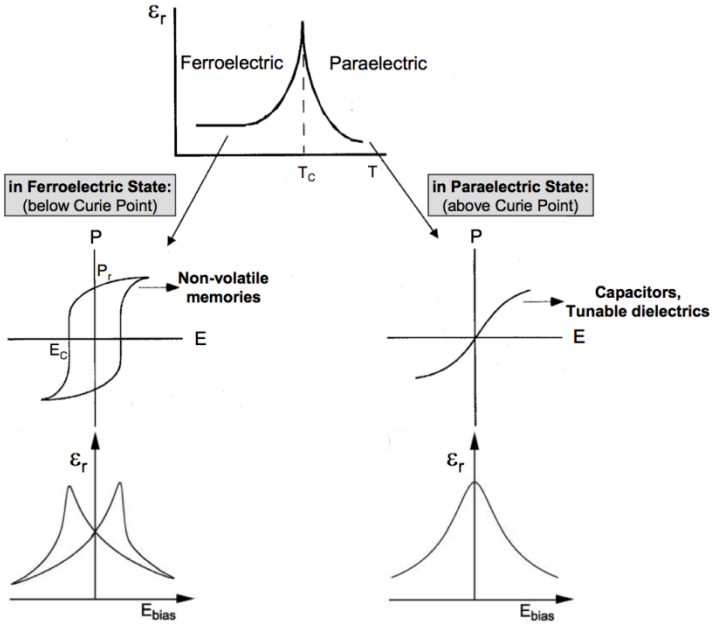


Figure 2.3.Temperature dependence of the relative dielectric constant of a ferroelectric material and different responses to electric field in ferroelectric and paraelectric states[7]

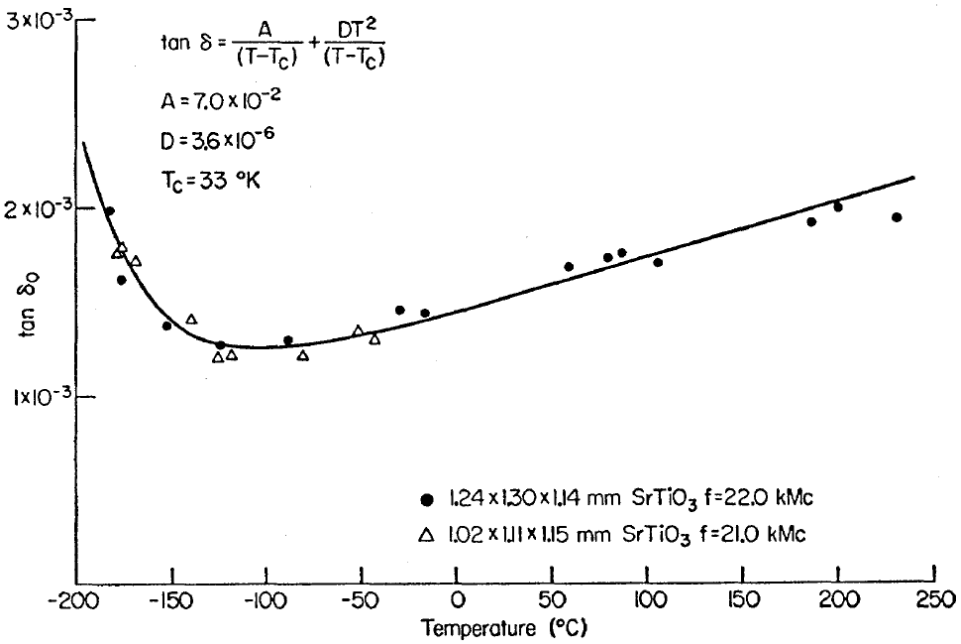


Figure 2.4. Temperature dependence of the loss tangent at zero biasing field for single crystal Strontium titanate at microwave frequeuncies [7]

Ferroelectrics can be divided into domains separated by domain walls, where domain is a group of unit cells within a single crystal and all of them has the same spontaneous polarization orientation. By applying alternating electric field, the spontaneous polarisation of domains will change repeatedly and this switching process results in a polarisation vs. electric field hysteresis loop. Generally, the existence of P-E loop is the evidence of classifying a ferroelectric material. In the paraelectric phase, the polarisation is strongly proportional to the external applied electric field and no hysteresis exists. In the ferroelectric phase, the polarisation does not go to zero when the external electric field is removed and exhibit a remanent polarisation P_r. This is due to the oriented domains being unable to return to their original random state without an additional energy input by an oppositely directed field, known as the coercive field E_c is needed to bring the polarisation to zero. Thus, the ferroelectrics operating at frequencies higher than 1MHz suffers from high dielectric losses. Further increasing the reverse electric field will lead to polarization saturation in the opposite direction.

The theory of ferroelectricity was first developed in 1949 by Devonshire and Landau[8, 9] to explain the ferroelectric phenomenon in $BaTiO_3$. He used an expansion of the Helmholtz free energy F of a ferroelectric crystal as function of the macroscopic polarisation vector P, assuming the free energy can be expressed as[10]

$$F = \frac{\alpha}{2}P^2 + \frac{\beta}{4}P^4 \quad (2.4)$$

where α and β are constants. The higher order terms are ignored in this expansion and the series do not contain terms of odd powers of polarisation vector due to the free energy of crystal will not change with polarisation reversal. The equation of state $\frac{\partial F}{\partial P}$ leads to a derivative with respect to P gives the following,

$$F = \alpha P + \beta P^3 \quad (2.5)$$

Using $\varepsilon = \frac{1}{\varepsilon_0}\frac{\partial P}{\partial E}$ and $\varepsilon(0) = (\alpha\varepsilon_0)^{-1}$,

$$\varepsilon = \frac{1}{\varepsilon_0(1+3\beta\varepsilon(0)\varepsilon_0 P^2)} \quad (2.6)$$

where ε_0 =8.864 × 10^{-12}Fm^{-1}. The dielectric constant in absence of electric field/polarisation is given by,

$$\varepsilon(0) = \frac{1}{\varepsilon_0 \alpha} \quad (2.7)$$

where α is assumed to be linear function of temperature and vanishes at the Curie-Weiss temperature T_c,

$$\alpha = \frac{1}{\varepsilon_0}\frac{T - T_c}{C} \quad (2.8)$$

where C is the Curie-Weiss constant. This assumption agrees with the incipient ferroelectric $SrTiO_3$ and $KTaO_3$ from 50-80K to the melting points of the materials shown by Rupprecht *et.al*[11] in 1964. However, later Muller *et.al*[12] found for temperatures below the Debye temperature, the assumption will not work and the lattice vibrations should be included as the temperature dependence of α slows down.

Dielectric materials are generally electrical insulators and susceptible to polarization in the presence of an externally applied electric field. The capacitance of a parallel plate capacitor will increase if a dielectric is inserted and the applied electric field will induce dipole moments within the material. One of the main characteristics of dielectric material is the dielectric constant ε_r (also known as relative permittivity). It is the ratio of the permittivity of a dielectric material (ε) to the permittivity of a vacuum (ε_0=8.85×10^{-12}F/m).

$$\varepsilon_r = \frac{\varepsilon}{\varepsilon_0} \quad (2.9)$$

For real dielectric materials, which possess both capacitive and resistive contributions, complex relative permittivity is used to describe the material,

$$\varepsilon_r^* = \varepsilon_r' - j\varepsilon_r'' \quad (2.10)$$

where ε_r' is the real relative permittivity or dielectric constant, ε_r'' is the relative resistive loss factor and j is a complex number.

The dielectric constant of the ferroelectric materials can be varied by applying an external electric field and this property is often described by the term "tunability", shown below:

$$\text{Tunability} = \frac{\varepsilon_{r0} - \varepsilon_{re}}{\varepsilon_{r0}} \times 100\% \quad (2.11)$$

where ε_{r0} is the dielectric constant of the ferroelectric material without external electric field, ε_{re} is the dielectric constant when the ferroelectric material is biased with an external electric field.

When an alternating electric field is applied to the dielectric, the absorption of electrical energy by the material is described as "dielectric loss", which is presented as the loss tangent tanδ.

$$\tan\delta = \frac{\varepsilon_r''}{\varepsilon_r'} = \frac{1}{Q_{FE}} \quad (2.12)$$

where Q_{FE} is the quality factor of the ferroelectric material. The dielectric loss can be contributed by intrinsic losses such as the interaction of the microwave field with the phonons or extrinsic losses such as the interaction between the microwave field and the defects.[13]

The tunability and loss tangent are closely related and require an optimal trade-off between them for a better microwave device performance. Experimentally[13] it was shown that a ferroelectric material with higher loss tangent usually has a larger tunability. To indicate the quality of ferroelectric material, the K factor[13] correlates the tunability and the loss tangent parameters,

$$K = \frac{(n-1)^2}{n \cdot tan\delta(U_{min}) \cdot tan\delta(U_{max})} \quad (2.13)$$

where n is the tunability ($n = \frac{\varepsilon(0)}{\varepsilon(U_{max})}$ and $n \geq 1$), U_{min} and U_{max} are the voltage states applied to the ferroelectric material. A ferroelectric material for microwave applications and devices is usually operated in its paraelectric state close to its Curie temperature to ensure high tunability and low loss tangent, but it does require a large electric field to obtain a relatively high tunability value in the thin film form. The quality factor (Q factor) can be used to characterize the losses in devices, which is defined as the ratio of stored energy to the energy dissipated.

Polarization of a dielectric material is defined as the total dipole moment per unit volume. It originates from the dipole alignments upon the application of an external electric field. A dipole is a system made up of positive and negative charges that are separated by a distance *a*. Assuming if the position vector is r_i, then the dipole moment *p* of the charge q_i is

$$\mathrm{p} = \mathrm{q} \cdot \mathrm{a} \tag{2.14}$$

$$\mathrm{p} = \sum_{\mathrm{i}} \mathrm{q_i r_i} \tag{2.15}$$

A dielectric material is polarized by the rearrangement of charges inside the dielectric when an electric field is applied. In macroscopic view, the dielectric has no net charges when no electric field is applied, because the dielectric has equal number of positive and negative charges within a macroscopic volume, so the net charge is essentially zero.

The total dielectric displacement D on the application of an electric field E is the sum of the displacement due to electric field E and due to the net polarization P from the material.

$$D = \varepsilon_0 E + P \tag{2.16}$$

The net polarization P is proportional to the electric field E by

$$\mathrm{P} = \varepsilon_0(\varepsilon_\mathrm{r} - 1) = \varepsilon_0 \chi \mathrm{E} \tag{2.17}$$

where the dielectric susceptibility χ is related to the relative dielectric constant by $\chi = \varepsilon_\mathrm{r} - 1$ and are both field-dependent.

There are four types of polarization mechanisms that can contribute towards the dielectric response. The frequency dependence of the dielectric constant ε_r' and loss factor ε_r'' for dielectric in an alternating electric field is presented in Figure 2.5.

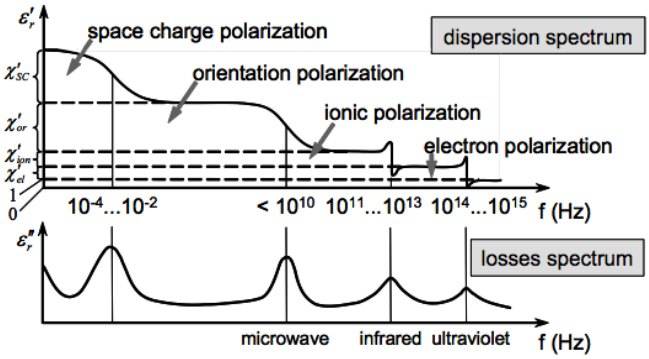


Figure 2.5. Variation of dielectric constant and loss factor with frequency of an AC electric field. [14]

When an alternating electric field is introduced, the polarizability of the dielectric material is selectively excited through different polarization mechanisms at various frequency ranges. There are four types of polarization mechanism that contributes to the dielectric response and total polarization:

- Electronic polarization-It occurs when an electric field displaces the nucleus of a neutral atom with respect to the surrounding electrons. This polarization is present in all materials and the electronic polarizability α_{el} is approximately proportional to the volume of an electron shell, so large atoms have bigger electronic polarization.
- Ionic polarization-It occurs when the materials are ionic and the cations and anions are shifted in opposite directions under an applied electric field, which induces a net dipole moment.
- Orientation polarization-It describes the alignment of permanent dipoles. The electric field can generate a preferred direction for the dipoles, while the thermal vibrations of the atoms can affect the alignment. Thus, orientation polarization decreases with increasing temperature.
- Space charge polarization-It occurs for dielectric materials that show spatial inhomogeneities of charge carrier densities and occurs when the mobile charge carriers are restricted by a physical barrier that inhabits charge migration, then the charges will build up at this barrier producing a localized polarization.

The total polarization of a dielectric material results from all the contribution discussed above.

$$P = P_{el} + P_{ion} + P_{or} + P_{sc} \qquad (2.18)$$

The contribution of a particular polarization mechanism at a particular frequency range is dependent upon the mass of the particles. When frequency reaches the radio frequency range, the molecular polarization will slowly cease to contribute to net polarization as the frequency continuously increases. As frequency increases, the number of polarization mechanisms will decrease and cease to function. Frequency regions where the dielectric constant is modified and dielectric loss peak occurs are the dispersion regions. The frequency dependent phenomena observed in these regions are due to dielectric relaxation, which is attributed to a delayed response of a certain polarization mechanism to the alternative electric field.

The dielectric constant depends on the film thickness and increases with thickness shown in Figure 2.6.[15, 16] The decrease in dielectric constant can be modeled by assuming the presence of the "dead-layer" at the electrode/ferroelectric interface. This dead layer is considered of a thin dielectric later with severely depressed dielectric constant and tunability. The dielectric constant deteriorates with thinner films as the effect of dead layer becomes more significant. The dead layer can be modeled using series capacitor model consisting of bulk and interfacial deal layer capacitors, where the capacitance is given below.

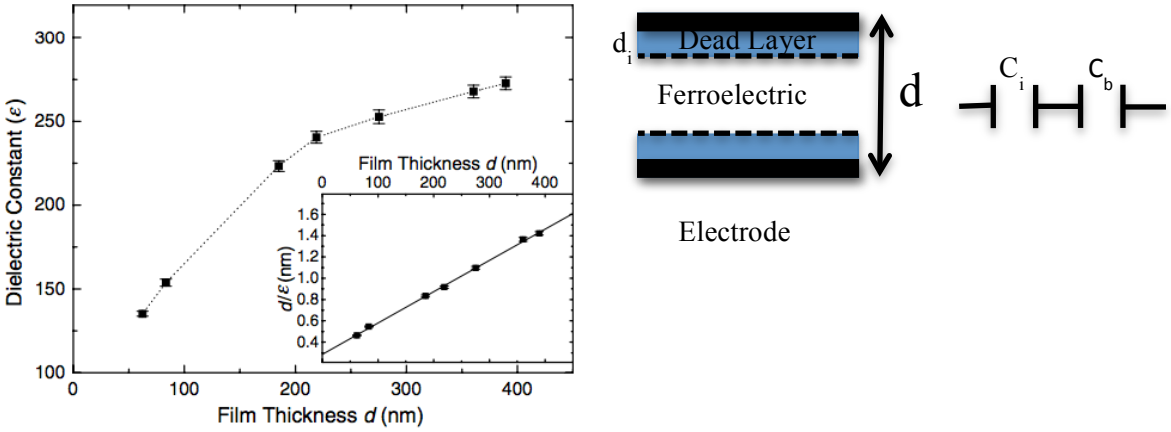


Figure 2.6. The model of the interfacial dead layer within a ferroelectric device and the dependence of dielectric properties on the thickness of $(Ba_{50}Sr_{50})TiO_3$ thin films.[15, 16]

$$\frac{1}{C} = \frac{1}{C_b} + \frac{1}{C_i} \qquad (2.19)$$

Here, C_i and C_b are the capacitance values of the interfacial (i) and bulk ferroelectric(b). If the dead layer thickness d_i is independent of the total thickness d, then

$$\frac{d}{\varepsilon} = \frac{d_i}{\varepsilon_i} + \frac{d-d_i}{\varepsilon_b} = \frac{d_i}{\varepsilon_i} + \frac{d}{\varepsilon_b} \qquad (2.20)$$

where ε is the dielectric constant,$d=d_b+d_i$, $\varepsilon_b >> \varepsilon_i$. The last term of equation 2.20 is valid due to the total film thickness is much larger than the interfacial dead layer thickness. The term $\frac{d}{\varepsilon}$ is a linear function of d with gradient of $\frac{1}{\varepsilon_b}$ and y axis intercept of $\frac{d_i}{\varepsilon_i}$.[15] This model is valid when the film is thicker than the assumed dead layer thickness. Thus, the effect of interfacial dead layer on the dielectric constant becomes smaller as the film thickness increases.

The theory of dielectric losses in the ferroelectrics was thoroughly investigated by Taganstev[17] and Vendik et.al[18], where the intrinsic phonon loss mechanism and the extrinsic defect loss mechanism are the two main components. The intrinsic loss is originated from the interaction of the alternating field with the phonons of the materials, which is the absorption of the energy quantum of the electromagnetic field in collision with the thermal phonons. Thus, the energy from the electric field will transfer into thermal energy causing an increase in the dielectric temperature. For frequencies lower than the damping frequency of the phonons Γ, (e.g $SrTiO_3$-150GHz) the dependence is

$$\mathrm{Tan}\delta_{\mathrm{phonons}} \propto \omega \mathrm{T}^2 \varepsilon_r^{\frac{3}{2}} \qquad (2.21)$$

where ω is the angular frequency, T is the temperature ε_r is the relative dielectric constant. In typical non-centrosymmetric crystals, the quasi-Debye mechanism contributes to the total intrinsic losses. For frequencies $\omega < \Gamma$, the contribution is

$$\mathrm{Tan}\delta_{\mathrm{Quasi-Debye}}(\mathrm{E}) = \mathrm{AI(E)}\omega \mathrm{n} \qquad (2.22)$$

where A is the fitting parameter, n is the tunability, the function I(E) approximately equal to 1 for small values of n. However, when the electric field is large, the $\mathrm{Tan}\delta_{\mathrm{Quasi-Debye}}$ vs. Electric field dependence deviates from the expression above and would be different for various materials.

The extrinsic losses of the paraelectric state ferroelectrics are due to the charged defects associated with the electrostriction effect. The electrostriction around the charged defect excites acoustic vibration within the material, which dissipates the energy of the microwave field. The losses due to charged defects are characterized by the relation[13],

$$\mathrm{Tan}\delta_{\mathrm{cd}} \propto \omega\varepsilon \qquad (2.23)$$

However, the loss tangent is experimentally more like the following behaviour[19],

$$\mathrm{Tan}\delta_{\mathrm{cd}} = \mathrm{A(E)}\omega^{\frac{1}{3}} \qquad (2.24)$$

When the ferroelectric materials based microwave devices operate at high frequencies, the reflection coefficient under electric field shows a resonant dip that is not observed for low frequencies, shown in Figure 2.7. The depth of these resonances varies with the electric voltage and frequencies at which the resonances occur depend on the layer structure of the device. This phenomenon is found to be caused by the electrostrictive property of the ferroelectric and induced field dependent piezoelectricity.

Electrostriction is a non-linear electromechanical coupling mechanism in the centrosymmetric crystal structure as opposed to piezoelectricity that governs the non-centrosymmetric crystal structure. Electrostricition is the coupling that exists between the strain and the electric field applied and it exists for al dielectrics.

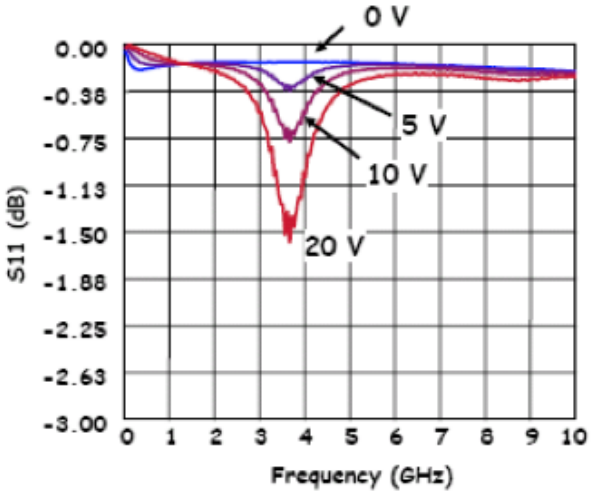


Figure 2.7. The bias induced resonant dips observed in BST50-50 based capacitors from 0V-20V.[20]

A general relation between induced strain S and the electrical polarization P due to the electrostriction effect can be deduced assuming there is zero applied stress[21],

$$S = QP^2 \tag{2.25}$$

where Q is the electrostriction coefficient. Using the polarization term due to applied electric field,

$$P = P_s + \chi E \tag{2.26}$$

where P_s is the spontaneous polarization, χE is the induced polarization due to applied electric field. Total strain can now be separated into three parts- spontaneous strain, linear piezoelectric strain and quadratic electrostrictive strain.

$$S = QP_s^2 + 2QP_s\chi E + Q\chi^2 E^2 \tag{2.27}$$

In the paraelectric state, there is no hysteresis and piezoelectric effect since the crystal structure is centrosymmetric, so only the electrostrictive term dominates the resultant strain. Due to the electrical field dependent polarization, the electrostrictive effect is dependent on the applied electric field, this allows us to control the mechanical/electrical coupling and generate acoustic waves through the converse piezoelectric effect. For ferroelectric materials, the generation and strength of acoustic waves are dependent mainly on the applied DC electric field. Therefore, tunable bulk

acoustic wave resonators can be fabricated using paraelectric state ferroelectric materials.

The bulk ferroelectrics are widely found in electronics such as ceramic capacitors, positive temperature coefficient resistors for thermistors and piezoelectric/pyroelectric ceramics for sensing applications. Bulk ferroelectric was not suitable for microwave tunable devices, because of the difficulties matching the reactance of the bulk ferroelectric to the impedance of the rest of circuit and requirement of high tuning voltages. Thin film ferroelectrics were seen as the solution and gathered interest in the late 1960, but it was limited to the fabrication technology and device electronics at that time. They only developed into reality with the advance of thin film deposition techniques and ability of integrate ferroelectrics with semiconductor in the mid 80s. The current and potential application for thin film ferroelectrics include memories, microelectromechanical systems(MEMs) and microwave tunable devices. The bias electric field dependence of the dielectric constant is an intrinsic property of ferroelectric that is crucial to produce voltage controlled tunable microwave devices and systems.

In the present FBAR resonator using piezoelectric materials usch as AlN and ZnO, the highest tunability achieved by heating, semiconductor and varactor loading is below 1% and large DC voltage are required for tunable filter applications. The ferroelectric films in their polar/piezoelectric phase such as PZT and BTO exhibits higher tunability of 2% and above, but their large hysteresis and low Q factor limits their application. Strontium titanate ($SrTiO_3$) and barium strontium titanate ($Ba_xSr_{1-x}TiO_3$) thin films are the most commonly used ferroelectric thin films for tunable film bulk acoustic wave resonator. Their paraelectric phase is ideal for this purpose due to the high dielectric constant, high tunability, absence of hysteresis and lower dielectric loss at microwave frequencies. $SrTiO_3$ is an incipient ferroelectric or quantum paraelectric material, which means it is a centrosymmetric cubic structure at room temperature and undergoes a structural phase transition with reducing temperature to a tetragonal phase at 105K.[13] The tunability of STO at room temperature is relatively low and they need to be cooled down to cryogenic temperature to reach reasonable tunability. By mixing $BaTiO_3$ and $SrTiO_3$, a solid solution of $Ba_xTi_{1-x}O_3$ is formed and the Curie temperature can be changed from around 40K to 385K by varying the Ba to Sr ratio in the mixture.[22] This is very useful since the important material properties such as permittivity strongly depend on the Curie temperature. The DC

voltage controlled switchable FABRs using paraelectric state ferroelectric materials have the advantages of exhibiting fixed resonance frequency and also additional functionalities such as switching and frequency tuning. The DC bias induced acoustic transformation from microwave power in the ferroelectric materials makes it desirable for a BAW resonator. Table 2.1 shows a comparison between the mechanical and electrical properties of ferroelectric and piezoelectric materials and its shows the ferroelectric-based materials are comparable in every aspect, thus making ferroelectric materials ideal candidates for use in bulk acoustic wave resonator applications.

Material	**Density (kg/m^3)**	**ε_r**	**V_{long}(m/s)**	**Lattice Constant(Å)**	**k^2(%)**	**Tan δ**	**e_{33}**
$SrTiO_3$	5120	300	7672	3.905	3	0.005 at 1GHz	-0.13 C/m^2
BST	5100-6000	360 - 900		3.9-4	7-20	0.0004-0.003 at 1GHz	
$BaTiO_3$	6035	1200	5600	4	6.2	0.1 at 1 GHZ	191 pC/N
AlN	3260	10.5	11340	a=3.11;c=4.98	6.1	0.003 at 1 to 10kHz	1.5C/m^2
ZnO	5680	10.2	6370	a=5.2;c=3.25	7.4	0.01..0.1 at 1 to 10kHz	1.32C/m^2

Table 2.1. Comparison between the ferroelectric materials and piezoelectric materials in terms of mechanical and electrical properties[3, 23] (ε_r is the dielectric constant, V_{long} is the longitudinal velocity, k^2 is the piezoelectric coupling coefficient, e_{33} is the piezoelectric stress coefficient)

2.2 Bulk Acoustic Wave Resonator

The concept of bulk acoustic wave resonators originated first in 1967 by Sliker and Roberts from a composite bulk quartz crystal resonator with thin film CdS transducers.[24] Later in 1968, Page et.al[25] showed that the quartz crystal can be replaced by a thinner 75μm substrate of single crystal silicon. Satoh et.al[26, 27] have improved the device and fabricated ZnO and AlN based micromachined film bulk acoustic wave resonators fully compatible with IC integration. The film bulk acoustic wave resonator (FBAR) technology can be potentially used in bandpass filters and chemical sensors. Aluminium Nitride and Zinc Oxide are the most investigated materials for TFBAR applications, because they exhibit high quality factor, high electromechanical coupling coefficient, high acoustic propagation velocity and

reliability, but require external frequency tuning passive components.[28, 29] Resonance frequency tunability of these piezoelectric materials with microelectromechanical systems (MEMs)structure setup as tuning layer has been reported to be around 0.4%-1.5%.[30] Electrostatic tuning of the bulk acoustic resonator itself is relatively weak and the tunability can only reach 1%.[31] The paraelectric phase ferroelectrics are generally not piezoelectric either, but the piezoelectric effect can be externally induced through DC electric field. Gevorgian et.al[32] have recently demonstrated that a tunable bulk acoustic wave resonator using ferroelectric materials in the paraelectric phase $Ba_{0.25}Sr_{0.75}TiO_3$ is based on the use of electrostriction phenomenon and field dependent piezoelectric effects to achieve tunable resonant frequencies. Tunable bulk acoustic wave resonators would enable development of a new class of components with enhanced functionalities such as tunable switches, tunable filters, voltage-controlled oscillators and tunable amplifiers.

The most common configuration of a thin film bulk acoustic wave resonator (TFBAR) is based upon the standing bulk acoustic wave across the thickness of the piezoelectric layer sandwiched between two metal electrodes. This structure setup must be enclosed by acoustically insulating boundaries such that energy loss is minimized through the substrate and this is typically done by introducing an air cavity or an acoustic reflector under the resonator.[33] Low cost substrates can be used instead of piezoelectric substrates and can be potentially compatiable with Integrated Circuits & Systems. The typical frequency range of a FBAR resonator is from 1GHz to 10GHz[31], such high frequency capabilities are becoming increasingly important in today's demanding communications sector.

Mechanical motion is initiated in the piezoelectric when an RF signal is applied across the device. Resonance occurs when the thickness of the film is equal to a multiple of half the wavelength of the input signal shown below[34],

$$F_{res}=1/\lambda_{res}=V_a/2d \qquad (2.28)$$

$$V_a=\sqrt{\frac{E}{\rho}} \qquad (2.29)$$

where F_{res} is the resonant frequency of the device, λ_{res} is the wavelength, d is the thickness of the film, E is the Young's Modulus, V_a is the speed of a travelling wave and ρ is the density.

The resonator is one of the key components of frequency generation and selection applications of oscillators and filters. By applying an AC electric field to a piezoelectric crystal, acoustic waves will be excited that result in a resonance at a frequency determined by the mechanical properties and physical dimensions of the crystal. Since the resonance frequency of the piezoelectric resonators based on bulk acoustic waves depend on the crystal dimensions, the maximum frequency is mainly related to the thickness of the piezoelectric crystal.[35]

It must be noted that the electrical performance of bulk acoustic wave (BAW) resonators depends on the piezoelectric layer and how the acoustic wave is confined in the structure. The acoustic waves are generated and reflected within the piezoelectric film due to the converse piezoelectric effect in bulk acoustic wave resonator as an AC electric field is applied. When half of the acoustic wavelength is equal to the thickness of the piezoelectric film, a mechanical standing wave is formed and resonance is observed. The thickness must be at odd number of half-wavelength for higher order resonances. The acoustic waves then polarize the material through the direct piezoelectric effect. The mechanically induced polarization at the standing wave frequency is 180° out of phase with the dielectric polarization due to the externally applied AC field. At this frequency, the current is minimized due to polarization charge cancelling out and gives a parallel type resonance at the electrical port. At a lower frequency, the two polarization charges are in phase and results are high current and a series resonance.

In an ideal scenario of bulk acoustic wave resonator with infinitely thin electrodes, the thickness mode resonant frequency in series (f_s) and parallel (f_p) is given as the following,[21]

$$\mathrm{f_p} = \frac{\mathrm{V_{ac}}}{2\mathrm{t}} = \frac{1}{2\mathrm{t}}\sqrt{\frac{\mathrm{c_{33}^D}}{\rho}} \tag{2.30}$$

$$\mathrm{f_s} = \mathrm{f_p}\sqrt{1 - \frac{8}{\pi^2}\mathrm{k_t^2}} \tag{2.31}$$

$$\mathrm{k_t} = \frac{\mathrm{e_{33}^2}}{\mathrm{c_{33}^D}\varepsilon_{33}^{\mathrm{S}}} \tag{2.32}$$

where V_{ac} is the acoustic wave velocity, t is the thickness of the ferroelectric film, k_t is the electromechanical coupling coefficient(k_{33}), ρ is the density of the ferroelectric film, C_{33}^D is the stiffness coefficient in orientation normal to the surface of the

piezoelectric film, $\varepsilon_{33}^{S}$is the permittivity coefficient and e_{33} is the piezoelectric stress coefficient.

The electrical impedance of a bulk acoustic wave resonator is characterized by the resonances at the resonance frequency f_r where the impedance value is at the minimum and the resonances at the antiresonance frequency f_a where the impedance value is at infinity. This is illustrated in Figure 2.8. The BAW resonator behaves as an inductor when the phase at 90° and exhibit a capacitive behaviour when the phase reaches -90°.

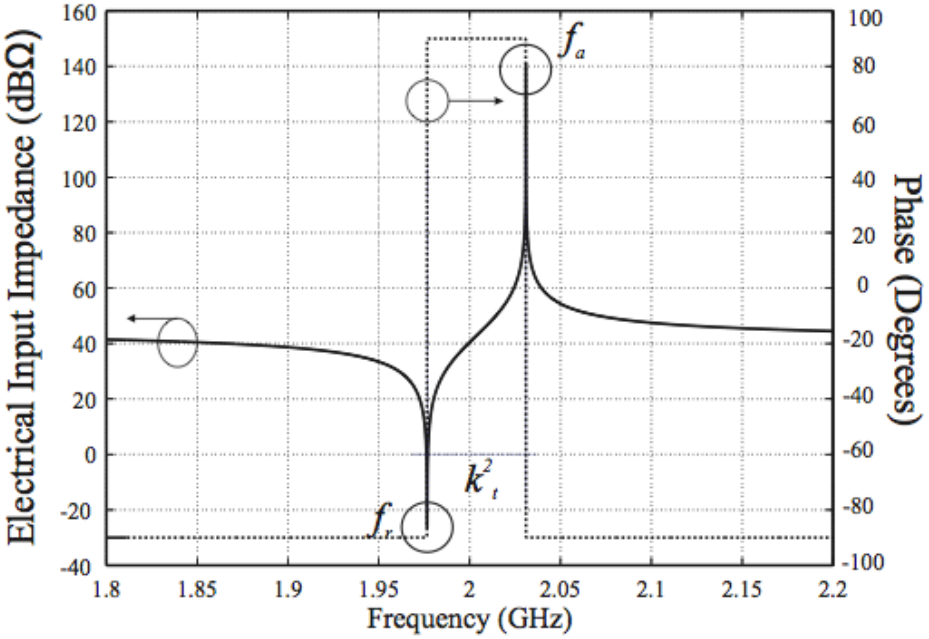


Figure 2.8. Electrical input impedance of a BAW resonator[36]

2.2.1 State of Art of Ferroelectric Materials in BAW Resonators

Ferroelectric materials such as Strontium Titanate (STO) and Barium Strontium Titanate ($Ba_xSr_{1-x}TiO_3$) are promising candidate for bulk acoustic wave resonator with tunability, i.e a possibility to change the resonance frequency. Therefore, it would enable development of new components such as tunable filters, switches and voltage controlled oscillators. Ferroelectric materials are strong candidates for commercial tunable microwave frequency devices and applications, because of their fast tuning speeds, low cost, high power handling, miniaturization and potential for Si integration.[37] The permittivity of ferroelectric materials can be changed proportionally with the applied DC electric field, but it is limited to the Curie temperature as the phase change from ferroelectric to paraelectric. The main disadvantage for using ferroelectric materials in tunable microwave devices is the

relatively large dielectric loss tangent and associated microwave dissipation. However, recent literature, including our collaborators in Russia has suggested this loss tangent is due to interaction of microwave field with the phonons causing the excitation of bulk acoustic waves within the ferroelectric film and this microwave power loss can be utilized to make a novel tunable bulk acoustic wave resonator.[1] This microwave loss can also be reduced through improving thin film fabrication techniques, but the device tunability will decrease as well as the insertion loss.

The microwave properties of these ferroelectric materials like STO and BST have been characterized by many research groups. A summary of the measured tunability and loss tangent is summarized in the table 2.2 and 2.3 below.

Device Characterisation	**Publications**	**Tunability**	**Loss Tangent**
STO on CeO_2 on Sapphire Substrate	Kozyrev et.al[38]	35%	0.04-0.05 at 3GHz
STO on YBCO on LAO Substrate	Galt et.al[39]	50%	0.01 at 6-20GHz
STO on LAO Substrate	Petrov et.al[40]	25%	0.005 at 20GHz
BST50/50 on MgO Substrate	Jackson et.al[41]	50%	0.055at 20GHz
BST 70/30 on Silicon Substrate	Tombak et.al[42]	42%	0.004 at 45MHz to 0.2GHz

Table 2.2. A summary of the dielectric properties measurements reported for STO and BST films

Kozyrev et.al[38] reported the microwave properties of STO planar varactors on CeO_2 buffered r-plane Al_2O_3 substrates using 200nm thick $YBa_2Cu_3O_{7-x}$ electrodes. The planar varactor was inserted into the gap at the midpoint of the resonator's microstrip line, thus loading the resonator with an additional capacitance. The varactors are made up of $1mm^2$ pads separated by 20μm gaps, which gave a capacitance of 0.4pF at zero bias and is tuned to 0.26pF with 260V corresponding to electric field of 130kV/cm at 3GHz. The tan δ ranged from 0.04 to 0.05 at zero bias and was reduced by a factor of 1.3 at higher bias voltages. This was one of the first reported STO device structures considered for electrically tunable microwave applications.

Galt[39] investigated the dielectric reporsponse of a microstrip resonator incorporated STO capacitor at its center on LAO susbtrate with 300nm thick YBCO electrodes.

The capacitor is 25μm^2 in area and it was tested at 10kHz to 20GHz to study the tunable frequency modes of the resonator. The results showed that the dielectric constant of the STO film is indepednent of frequency from 10kHz to 20GHz and the capacitance tuned by a factor 2 when the applied bias is varied from 0V to 60V(electric field-10V/μm). The loss tangent was in the 10^{-3} range at 4K and in the low 10^{-2} range at 76K.

Petrov et.al[40] reported the properties of single layer STO and multilayer STO structures on LAO substrates at microwave frequencies(40MHz-40GHz) as a function of appliced voltage and temperature. The STO films demonstrated relatively good tunability of 25% with an applied electric field of 19kV/cm and low film losses of tanδ<0.005 at 20GHz and 20K, which indicates their applicability for tunable microwave devices. Intermediate oxygen relaxation of STO film at high temperature of 900°C causes a reduction in its dielectric constant and the loss tangent, which reduces the number of structural defects present in the thin film.

Tombak et.al[42] reported low frequency measurements of $Ba_{0.7}Sr_{0.3}TiO_3$ parallel plate capacitors yielded 42% tunability at frequency range 45MHz to 0.2GHz using 7V DC bias and the dielectric loss tangent was around 0.004. The capacitors are in 50μm x50μm squares on top of silicon substrate. The frequency dependenet permittivity was relatively low due to Ti rich stoichiometry in the film and it imporved stability under large DC fields. The dielectric tunability decreases with increasing signal amplitude and the drop is proportional to the rms value of the RF signal amplitude. However, the possibility of integrating tunable microwave devices on silicon promotes great interest from the integration and compatibility.

Jackson et.al[41] reported the microwave properties of $Ba_{0.5}Sr_{0.5}TiO_3$ thin film coplanar phase shifters on MgO substrates in the frequency range of 45MHz-50GHz in 300nm thick coplanar waveguide transmission lines with a center line width of 50 μm and gap width 25 μm. Relatively high tunability of 50% was obtained between 0 and 3.2V/μm for films annealed ex situ and in situ annealed films recorded lower tunability values. The ex situ anneal films exhibit real dielectric permittivity of 2000 at 270K and tan δ value of 0.30. The optimization of the film deposition conditions was crucial in achieving the best microwave properties for device fabrication and characterisation. These works demonstrated the potential of achieveing low loss microwave tunable devices using ferroelectric materials such as STO and BST.

Material	F_{res}(GHz)	Q_f(GHz)	Tunable T_{fs}(%)	Tunable T_{fp}(%)	k^2(%)	Type
$SrTiO_3$[Saddik et.al][43]	7	700	1		3.3	Solidly Mounted
$SrTiO_3$[Volatier et.al][44]	2.2	110	1.62	0.59	3	Solidly Mounted
BST 25/75[Berge et.al][32]	5.5	715	3.8	1.2	7.1	Solidly Mounted
BST 50/50[Sis et.al][45]	1.28	900	NA	NA	7	Membrane
BST 70/30[Ivira et.al][46]	1.7	85	0	0.3	12-20	Membrane
$BaTiO_3$[Berge et.al][47]	3.8	30	1.3	4	6.2	Solidly Mounted

Table 2.3. Summary of Various Ferroelectric Materials Based Tunable FBARs

Saddik[43] reported a tunable STO(60nm) solidly mounted BAW resonator on an Bragg reflector (multilayers of Pt and SiO_2) on a sapphire substrate with a voltage dependent frequency tuning of 1% from 7.05GHz to 6.98GHz by an applied bias of 0-9V. The quality factor at the resonant frequency was approximately 100 and this is limited by the simplicitiy of the device design. The effective electromechanical coupling coefficient at 9V is 3.3% and the return loss at 9V is -9.5dB. The use of a thick metal electrodes and relatively thin STO thickness limits the Q factor of the resonator device.

Volatier[44] reported a tunable STO(430nm) electrostictive solidly mounted bulk acoustic wave resonator with a resonance frequency at 2.2 GHz and switch on voltage of 6V. The tunability of ±0.85% was achieved with a bias voltage between 6 to 30V. The quality factor is around 50 and no hysteresis was observed. The quality of STO film on top of the Bragg mirror still remains as the main problem. The lessening of porosity and crystal orientation should increase the dielectric constant, coupling coefficient and the quality factor of the resonator. This fabrication of an electrostrictive SMR BAW resonator using paraelectric state STO has realized the possibility of tunable or switch RF filters that are crucial to development of devices in the communication front end.

Berge[32] presented a switchable and tunable bulk acoustic wave resonator based on a paraelectric phase $Ba_{0.25}Sr_{0.75}TiO_3$(234nm) thin films on a Bragg reflector (HfO_2/SiO_2) on a silicon substrate. The measured resonance frequencies at series and

parallel are 5.5GHz and 5.7GHz at 25V bias. The tunability of the series resonance reaches 3.8% and the effective electromechanical coupling coefficient is 7.1% at a DC bias of 25V. The mechanical Q factor of the resonator is around 130 and is limited by the interface roughness. The reported tunability and coupling coefficient of the non hysteretic resonator is one of the highest recorded for tunable BAW resonators. The optimization of the resonator layers by improving deposition conditions of the BSTO film,control strain and minimize roughness will increase the Q factor greatly.

Sis et.al[45] presented an intrinsically switchable high Q BST(500nm) thin film bulk acoustic wave resonator in a membrane setup deposited on a silicon on insulator substrate. The resonance frequency was at 1.28 at 25V DC bias with Q factor exceeding 800. The active area of the measured device is 60x80μm. This significant improvement in the Q factor was obtained by the use of BST on silicon composite structure.

Ivira[46] reported the development of BAW resonator using electrostrictive BST 70/30 oxide thin films(1μm and 0.5μm) using Pt electrodes on silicon substrate for GHz applications in a membrane setup. The bragg reflector is often not compatible with the high temperatures required for BST deposition. The resonance frequency is at 1.7GHz and the electromechanical coupling coefficient ranged from 12 to 20 at the DC bias of 40 to 75V. The electromechanical coupling coefficient of the BST film based resonator is as good as the AlN based BAW resonator. The Q factor of the resonator was poor and it is the main drawback of the resonator. There was no piezoelectric effect at zero V_{DC} and it can be used in a switchable RF filter. The material quality of BST still require to be optimized to increase the quality factors and enhance the dielectric permittivity.

Berge et.al[47] reported the electricallt tunable solidly mounted thin film bulk acoustic resonators based on $BaTiO_3$ film(300nm) deposited on the silicon substrate and is acoustically isolated by a Bragg reflector stack. The acoustic resonance frequency occurs at 3.8GHz under 10V dc bias and the Q factor is approximately 30. The resonance frequency is tuned by 1.3% and the antiresonance frequency is tuned by 4%. The electromechanical coupling coefficient is 6.2% at 10V dc bias, which shows these microwave properties are much superior than the $Ba_{0.25}Sr_{0.75}TiO_3$ film reported. However, the hysteresis associated with the BTO at room temperature significantly limits the Q factor.

In the early stage of research, bulk and thick ferroelectric films in the paraelectric phase have been researched in tunable microwave devices. Later, single crystals and epitaxial films of $SrTiO_3$, $Ba_xSr_{1-x}TiO_3$ and $BaTiO_3$ have been considered due to lower losses.[13] The ferroelectric varactor is more superior than the semiconductor counterpart at the high frequency range(10-20GHz), where the *Q* factor of the ferroelectric varactors remain high and semiconductor decreases significantly.[48] The cost is an important issue for market commercialization and ceramics is generally a viable solution. The potential integration of ferroelectrics in non-volatile memory cells of the metal-insulator-semiconductor transistors can introduce a new type of microwave devices with enhanced functionalities at millimeter wave frequencies.

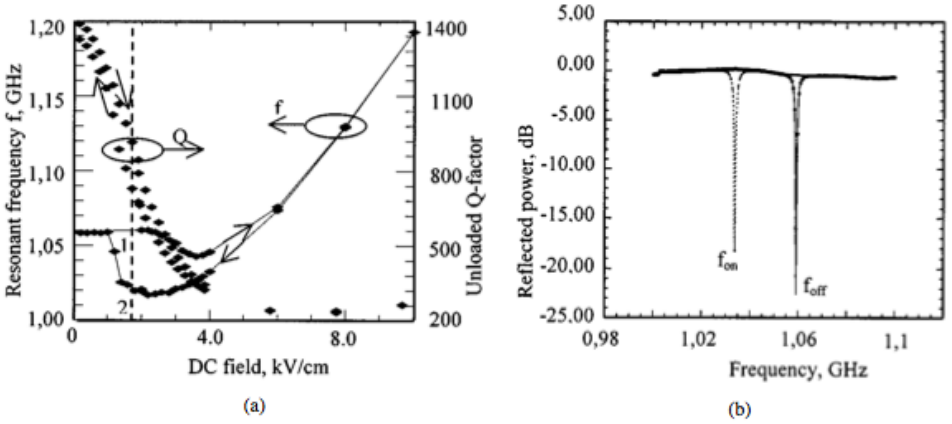


Figure 2.9. The dc bias dependence of a) resonant frequency and b) reflected power corresponding to two states (On and Off) at T=52K and dc field of 1.2kV/cm.[49]

The STO devices presented in the table 2.2 generally require high tuning voltages and temperatures below 90K for optimal operation. It is generally known that STO thin films show non-tunable characteristics at room temperature. An increased tunabilty in the microwave range at room temperature can be achieved by the chemical substitution of strontium atoms to barium or introduce a tensile strain by tailoring the suitable substrate for epitaxial thin film growth.[50]A disk parallel plate resonator using single crystal STO with superconducting electrodes shows dc bias dependent resonant frequency and digital switching at two distinct resonant frequencies for the same dc field presented in Figure 2.9. Gevorgian et.al[51] observed dc field acoustic resonances in $SrTiO_3$ and paraelectric state $Ba_{0.25}Sr_{0.75}TiO_3$ parallel plate capacitors deposited on silicon substrate with tunability of more than 5% operating at frequencies upto 10GHz. Their loss tangent is generally between 0.06 to 0.07 at 3GHz. The dc biased resonance of the STO capacitor is observed at 3GHz and

10GHz.[51]Thin film $SrTiO_3$ Metal-Insulator-Metal capacitors on silicon substrates with Pt electrodes were fabricated to characterize the piezoelectric resonance in the micrometer to millimeter waveband at room temperature. An electric field of 250kV/cm was applied and piezoelectric properties were induced based on second order phase transition, which implies that paraelectric and ferroelectric phases coexisted in the STO films. The measured resonant and antiresonant frequencies and their associated amplitudes were related to the thickness of the electrodes and STO thin film. [52] The $SrTiO_3/SrRuO_3/CeO_2/YSZ$ heterostructure on silicon substrate at frequency range of 1-50GHz have shown tunability of 10-20% with loss tangent of 0.08 at 50GHz(without losses in Si).[53] The dielectric properties of STO thin films fabricated on LAO substrate with $SrRuO_3$ electrodes by PLD[54] were investigated, it has shown the proportional relationship of tunabilty with the loss tangent from temperature of 4K to 190K. The loss tangent decreased by two orders of magnitude as the film thickness changes from 25nm to 2.5μm at temperatures above 100K. Switchable and tunable STO bulk acoustic wave resonator integrated with a Bragg mirror have been fabricated by Volatier et.al. It demonstrated resonance at 2.2GHz that can be switched on with 6V bias and tuned $\pm$0.85% with application of 6-30V without hysteresis.[44]

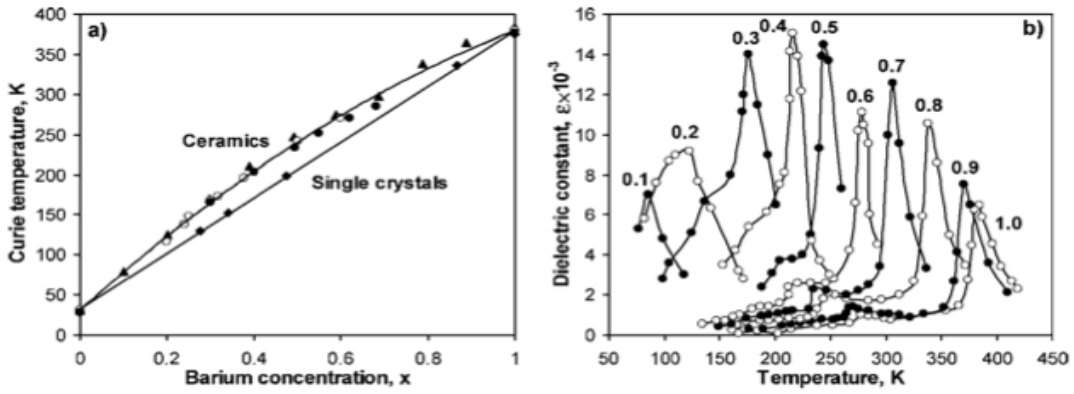


Figure 2.10. a)The relationship between Curie Temperature and Ba concentration for BST ceramic and single crystals, b)Temperature dependence of dielectric constant of BST ceramic for different Ba concentrations. [13]

$Ba_xSr_{1-x}TiO_3$ is a solid solution ferroelectric material used in many tunable RF and microwave devices. The paraelectric phase of the BST thin film at room temperature is preferred, because it exhibits high tunability and low dielectric loss at microwave frequencies.[13]The composition and temperature dependence of the permittivity of BST single crystals and ceramics are shown in Figure 2.10. The piezoelectric effect

can be induced through interfacial misfit stress caused by the substrate and defects such as oxygen vacancies and dislocations when external dc bias electric field is applied. [55] In case of ideal thin films with no misfit strain, the resonances in the ferroelectric varactor can be attributed to electrostriction only.[56]Berge *et.al* showed dc field dependences of resonant frequencies and electromechanical coupling coefficient for BST tunable bulk acoustic wave resonators. Their tunability of series and parallel resonances are 1.7% and 0.3% and the electromechanical coupling coefficient increased with dc bias upto 3.7% with 15V bias voltage. By improving the film quality, higher breakdown field can be achieved, hence the tunability is enhanced. The relative *Q*-factor is also expected to increase with improvement of film quality and optimization of electrodes and the Bragg reflector.[57] Zhu et.al have reported a dc voltage dependent switchable BST thin film bulk acoustic wave resonator on silicon substrate with a parallel resonance at 2.035GHz and series resonance at 1.975GHz with 25V dc bias applied. The electromechanical coupling coefficient was approximately 7.07% comparable to the Aluminum Nitride film bulk acoustic wave resonator.[58]Noeth et.al[59] also fabricated a tunable membrane type TFBAR based on $Ba_{0.3}Sr_{0.7}TiO_3$ thin film with resonance frequency tunability of 2.4% and antiresonance frequency tunability of 0.6% through application of dc bias field(615kV/cm). Although there is still room for improvement in the ferroelectrics performance, they require a careful optimization of the design to minimize the parasitic losses.

From these works on tunable and switchable BAW based on ferroelectric films, the quality of the ferroelectric film is key to research and improve the performance of the FBAR in agile RF front end architecture. The quality of the ferroelectric film is optimized through deposition conditions and achieving epitaxial growth. The all oxide epitaxy grown multilayer structure using STO as the active layer in a membrane setup on silicon substrate possess most of the advantages described from previous literature and is most suitable for the tunable bulk acoustic wave resonator. The possible compromise during this research are the low Q factor in performance, large number of intermediate steps and different equipment to achieve one multilayer structure.

2.2.3 Types of Bulk Acoustic Wave Resonators

Most of the thin film bulk acoustic wave devices are based on piezoelectric films (e.g AlN, ZnO) and the acoustic wave must be confined in the acoustic cavity created by

the piezoelectric layer in order to have a resonating mode within the structure. There are two basic designs of the thin film bulk acoustic wave resonator used to confine the acoustic waves-membrane mounted and solidly mounted. The membrane mounted TFBARs are fabricated by creating an air gap cavity below the bottom electrode through bulk micromachining of the substrate. The electrical behaviour of the air is a short-circuit forcing the acoustic wave to reflect between the top and bottom surfaces, thus generating a resonant mode. The surface mounted TFBARs use Bragg reflectors consisting of an alternating low and high acoustic impedance layers to acoustically isolate the resonator from the substrate. The setups are shown in Figure 2.11.

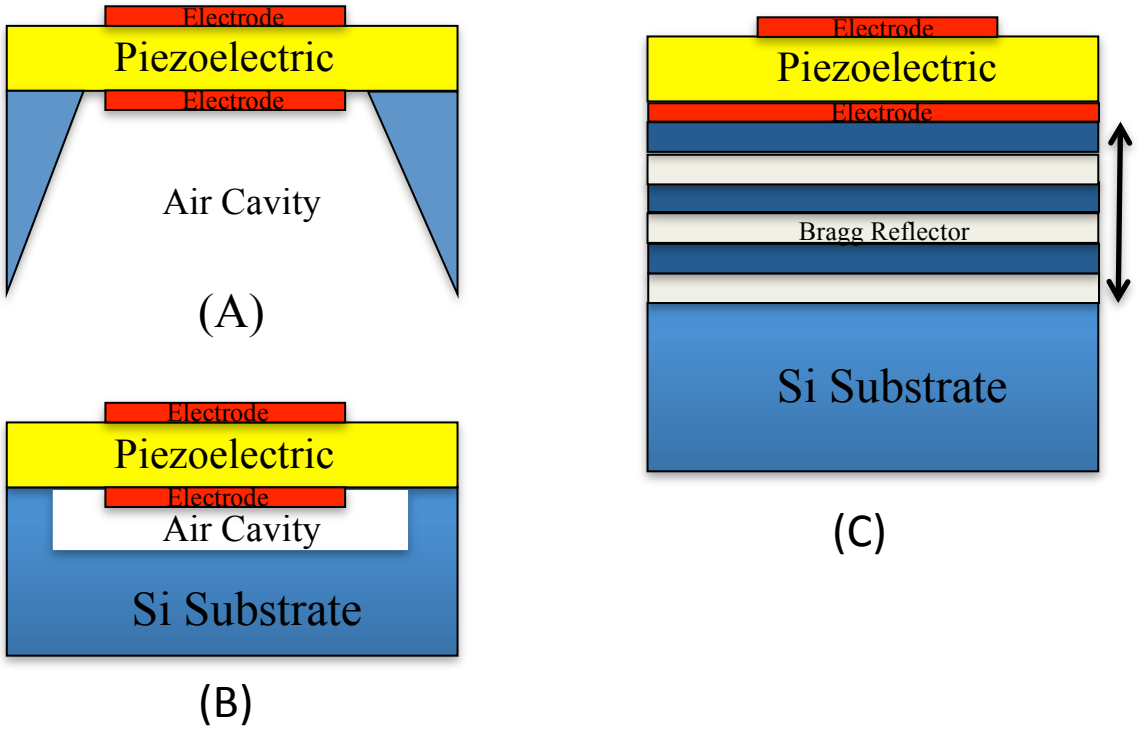


Figure 2.11. a) and b) are thin film bulk acoustic resonator setup and c) is the solidly mounted resonator topology

The structure setup of Figure 2.11a was the first type of bulk acoustic wave resonators presented in the 1980s by Lakin *et.al*[60], Grudkovskii *et.al*[61] and Nakamura *et.al*.[62] They made composite bulk micromachined resonators and acoustically coupled resonators with aluminium electrodes and used ZnO or AlN as the piezoelectric and Si as the substrate. Silicon anisotropic etching were used to release the piezoelectric layer using heavily boron-doped silicon as the etch stop. The *p*- doped silicon can act as a seed layer for the AlN growth and bottom electrode, because it is a good electrical conductor and possesses a low temperature coefficient of frequency.

The surface micromachined resonators were initially proposed by Satoh et al[63] in 1985 and the acoustical insulation was achieved by fabricating an air interface beneath the resonator using a sacrificial layer. Compared with the bulk micromachined structure, this surface micromachined resonator is not fragile and only single side mask alignment is required. The integrated circuits on the same substrate will also not be affected by the through wafer air cavities. This new air gap structure enables thin film resonators to be easily fabricated on top of a variety of substrates such as Si, GaAs, Sapphire, MgO and on top of a dielectric passivation film with Integrated Circuits. A surface micromachined FBAR made up of SiO_2/Al/ZnO operating at 2GHz has a Q factor of 300[64] and a k_t^2 (electromechanical coupling factor) of 5% and AlN based surface micromachined FBAR has a Q factor of 500 and a k_t^2 of 5.5%-6.5%.[65] The electromechanical coupling factor is a coefficient that measures the conversion efficiency between electrical and acoustic energy in piezoelectric materials. [66]

The solidly mounted resonator uses adjacent quarter wavelength layers with large effective transmission impedance to form a reflector between the resonator and the substrate, which resulted in the acoustical isolation of the resonator from the substrate leading to a high-Q resonator rather than a low-Q transducer. The concept was introduced by Lakin et al[67] in 1995 and filed for patent by Motorola. They used SiO_2/AlN, SiO_2/Si_3N_4,W/SiO_2 as the quarter wave length layers for acoustical isolation and patterned in complex filter structures to avoid capacitive coupling and other parasitic effects. SiO_2/AlN SMR based ladder filters working at 1.6GHz with 2.9dB insertion loss and 40dB rejection for use in the GPS systems was demonstrated based on the theoretical model by Lakin et.al.[68] The use of SiO_2 in reflectors is due to its positive temperature coefficient of frequency, which is the opposite to all the other reflector materials. By adding SiO_2 below or on top of the AlN or ZnO based solidly mounted resonator, the temperature coefficient of frequency can be reduced to zero without compensating for the reduction in the coupling coefficient. The solidly mounted resonator yields a lower effective coupling coefficient than the film bulk acoustic resonator, because a fraction of the acoustic energy is lost within the reflector. When operating at high frequencies, the requirement of a high degree of absolute film thickness control is essential. However, the SMR is less sensitive to film stress and requires less processing steps.

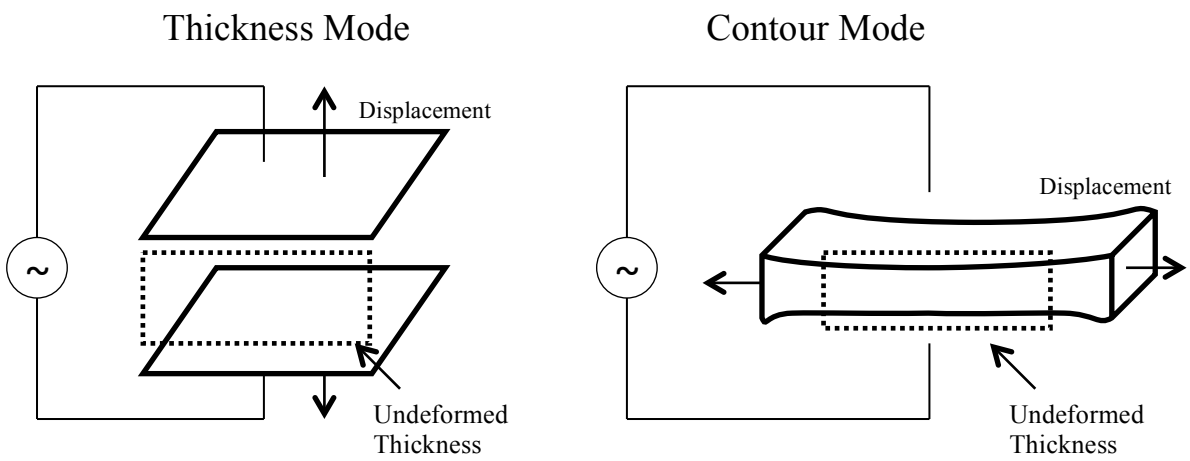


Figure 2.12. Thickness mode and Contour mode acoustic wave resonators

The FBAR resonators using ferroelectric thin films can be considered as thickness mode or contour mode. The thickness mode acoustic wave resonator is modelled similarly to the piezoelectric thin film FBARs, because their resonance frequency is inversely proportional to the thickness of the resonator. Figure 2.12 shows the two modes of acoustic wave resonators. A bulk acoustic wave resonator consisting of BST thin film sandwiched by two Pt electrodes is fabricated on a SiO_2/Si substrate. The resonance of this BST FBARs with and without Si substrate is simulated by Zhu et.al[69], which shown the generated acoustic waves is weak and damped by the silicon substrate. Thus it is necessary to remove the silicon substrate underneath completely. The contour mode acoustic wave resonator is designed to solve the difficulties regarding the thickness mode resonance, thus it is determined by the lateral dimensions of the resonator. The tolerance of the resonance frequency to lateral dimensions is greater than the thickness, which results in uniformity of resonance frequency distributed over the ferroelectric.

2.2.4 BAW Device Performance Requirements

The parameters regarding characterizing the performance of a bulk acoustic wave resonator are introduced here. The effective electromechanical coupling coefficient together with series and parallel resonance frequencies are defined and explained through the Mason's one-dimensional model for a piezoelectric resonator with two metal electrodes. The quality factor at resonance and antiresonance frequencies and unloaded Q factor are reviewed.

1. Effective Electromechanical Coupling Coefficient (K_{eff}^2)

The effective electromechanical coupling coefficient of the resonant (f_r) and antiresonant frequencies (f_a) of real thin film bulk acoustic wave resonators is defined in the equation below,

$$K_{eff}^2 = \frac{\pi^2}{4}\frac{f_a - f_r}{f_a} \tag{2.33}$$

Mason's one dimensional model[70] assumes an acoustic wave propagating in an vertical Z-axis direction within a piezoelectric slab connecting to an acoustic transmission line and bounded by two stress free boundary planes at the position Z_1=d/2 and Z_2=-d/2 with a thickness d=Z_1-Z_2. This graphically illustrated in Figure 2.13. They are one-dimensional since lateral dimensions are considered to be infinite, but lateral standing waves can occur due to the finite real dimension of the resonator structure. Thickness excitation mode occurs when the applied electric field is in the same direction as the wave propagation and lateral field excitation mode occurs when the electric field is perpendicular with the direction of wave propagation. At the boundary, the incident and reflected waves will be travelling in opposite directions and the constructive interference of these two waves creates the resonant behaviour of the resonator.

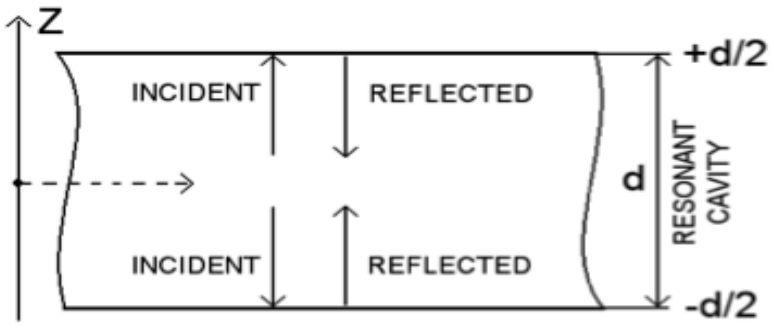


Figure 2.13. Excitation of wavefronts inside a resonant cavity[28]

The particle displacements at each boundary are[28]

$$u_1 = (ae^{-\frac{jkd}{2}} + be^{\frac{jkd}{2}})e^{j\omega t} \tag{2.34}$$

$$u_2 = (ae^{\frac{jkd}{2}} + be^{-\frac{jkd}{2}})e^{j\omega t} \tag{2.35}$$

where u is the particle displace, angular frequency $\omega=2\pi f$ and wave number k=angular frequency ω/acoustic wave velocity V_{wave}.

The stress and electrical displacements is key to determining the electrical impedance of the BAW resonator[28]

$$\mathrm{T_3} = \mathrm{C_{33}^E S_3} - \mathrm{e_{33} E_3} \tag{2.36}$$

$$\mathrm{D_3} = \varepsilon_{33}^{\mathrm{S}} \mathrm{E_3} + \mathrm{e_{33} S_3} \tag{2.37}$$

where T is the mechanical stress, D is the electrical displacement in the z-direction, S is the mechanical strain, E is the electrical field, $C_{33}^E$is the stiffness constant, $e_{33}$is the piezoelectric stress constant relating to the electric field and $\varepsilon_{33}^S$is the dielectric constant. When considering only the electro-acoustic waves at constant electric field, the electric displacement is zero as the elastic strain and the electric field polarization cancel out each other.[71] Thus the mechanical stress induced by the acoustic waves and the strain can be related,[28]

$$\mathrm{T_3} = \mathrm{C_{33}^D S_3} = \mathrm{C_{33}^E}\left[1 + \frac{(\mathrm{e_{33}})^2}{\mathrm{C_{33}^E \varepsilon_{33}^E}}\right]\mathrm{S_3} \tag{2.38}$$

$$K^2 = \frac{(\mathrm{e_{33}})^2}{\mathrm{C_{33}^E \varepsilon_{33}^E}} \tag{2.39}$$

where $C_{33}^D$is the stiffened elastic modulus and determines the acoustic wave velocity stiffened in the presence of piezoelectric medium. K^2 is the piezoelectric coupling coefficient.

The electrical impedance of the resonator is ratio of voltage over current. Here $k_t^2 = \frac{e_{33}^2 / \varepsilon_{33}^S}{C_{33}^D}$ is the intrinsic electromechanical coupling coefficient and measures how much electrical energy is transferred into mechanical energy through elastic deformation. Theoretically, this value is calculated from $\frac{V_0^2 - V_m^2}{V_m^2}$, where V_0 and V_m are the acoustic wave velocity of a non metalized and metalize surface.

$$Z_{im} = \frac{V}{I} = \frac{1}{j\omega C_0}\left[1 - k_t^2 \frac{\tan\left(\frac{kd}{2}\right)}{\frac{kd}{2}}\right] \tag{2.40}$$

The total electrical field has two components: an external part from the applied voltage and an internal part from the electric field induced by strain.

$$\mathrm{E_3} = \frac{\mathrm{D_3^{ext}}}{\mathrm{\varepsilon_{33}^S}} - \frac{\mathrm{e_{33}}}{\mathrm{\varepsilon_{33}^S}} \frac{\partial \mathrm{u}}{\partial \mathrm{z}} \tag{2.41}$$

then by substituting this expression into the voltage relation of $V = \int_{z_1}^{z_2} E_3 dz$, the current can be analytically expressed as

$$I = j\omega C_0 V - j\omega\left(\frac{e_{33}}{\varepsilon_{33}^S}\right) C_0 [u_1 - u_2] \quad (2.42)$$

where $C_0 = \frac{\varepsilon_{33}^S A}{d}$ is the static capacitance of the piezoelectric plate.

An approximate equation for the impedance can be derived using the following,

$$\frac{\tan\left(\frac{kd}{2}\right)}{kd/2} = \sum_{N=1}^{\infty} \frac{8}{(N\pi)^2 - (kd)^2} \quad (2.43)$$

where N=odd numbers represents the harmonic of the operation. The infinite impedance of this function occur at $\frac{kd}{2} = \frac{N\pi}{2}$. The frequency at which impedance equals zero and the admittance is infinite is the resonance frequency (series resonance). The frequency at which impedance is infinite and the admittance is equal to zero is the antiresonance frequency (parallel resonance). The antiresonance frequency is $f_a = \frac{N \cdot V_{wave}^S}{2d}$ and the resonance frequency for Nth poles is $f_r^N = \frac{V_{wave}^S}{2\pi d}\sqrt{(N\pi)^2 - 8k_t^2}$.The electromechanical coupling can also be defined in terms of relative separation between these two frequencies of the fundamental harmomic,

$$k_t^2 = \frac{\pi^2}{4}\frac{f_a - f_r}{f_a} \quad (2.44)$$

In reality, the impedance and admittance are never infinite, so the resonance occurs at the frequency where the impedance has a minimum and its phase crosses zero with a netative slope while the antiresonance occurs when the impedance has a maximum and the phase crosses zero with a positive slope.

Lateral standing waves can form undesired resonances in the performance for BAW resonator, which is closely related with the concept of energy trapping within the fundamental thickness mode and leaks to the lateral modes that results in degradation of the quality factor of the resonator.

2. Quality Factor

The quality factor is one of the most important quantities regarding the performance of a resonator. Generally it is expressed as the ratio between the stored energy and dissipated energy per wave cycle below,

$$Q = \omega \frac{\text{Energy Stored}}{\text{Dissipated Energy per one cycle}} \quad (2.45)$$

It can be of different origins such as electrical, acoustical or dielectrical, and it is a measure of relative loss of energy in the resonator. This quality factor is extracted

from the slope of the impedance phase curve $\Phi_Z$or the admittance phase curve Φ_Y at the resonance and antiresonance[72],

$$Q_{r,a} = \frac{f_{r,a}}{2}\left|\frac{d\Phi_z}{df}\right|_{f_{r,a}} \quad (2.46)$$

The quality factor is affected generally when connecting a resonator to an external circuit, thus the unloaded quality factor is important when comparing different resonator technologies.

The unloaded Q of any real resonator is measured using the S_{11} reflection coefficients based on a theorem derived by Bode et.al[73],

$$Q_{unloaded} = \omega \cdot \tau_{gd}\frac{|\Gamma|}{(1-|\Gamma|^2)} \quad (2.47)$$

where $\tau_{gd} = -\frac{d\varphi}{d\omega}$ is the delay, φ is the phase and $|\Gamma|$ is the magnitude of the reflection coefficient.

2.3 Dielectric Acoustic Wave Resonator

Microwave electromagnetic waves have frequency range from 0.3GHz to 300GHz[74] which correspond to a free space electric wavelength approximately from 1m to 1mm, respectively:

$$\lambda = \frac{c}{f} \quad (2.48)$$

where λ is the wavelength, c is the speed of light and f is the frequency.

There are three bands in the Microwave frequencies-the ultra high frequency (UHF) band from 0.3GHz to 3GHz, the super high frequency (SHF) band from 3GHz to 30GHz, and the extremely high frequency (EHF) band from 30GHz to 300GHz.[75] The UHF band is mainly used for the purpose of TV signals, mobile phones, and wireless local area network. The EHF band is called millimetre waves as its wavelength is on the order of millimetres.

In a microwave system, the components and circuits are separated into two main categories: passive and active. The passive devices are filters, phase shifter, matching networks and delay lines, which are connected with antennas and transceivers for microwave communication applications. Passive components cannot introduce net energy into the circuit and do not rely on any source of power. They can only change the phase and decreases the amplitude of a sine wave but not the shape. Active components require a source of power and can amplify and change the shape of a sine wave. In the modern tunable radio frequency (RF) and microwave telecommunication

devices, technologies for accomplish frequency agility are mechanical tuning, semiconductor diode, ferrites, micro-electro-mechanical systems (MEMs) and ferroelectric thin films. The performances of the tunable devices are closely related to the choice of technology.

Traditionally, mechanical tuning was the method used in microwave devices and the mechanically tunable devices possesses high power handling capability with a low insertion loss, but the low tuning speeds, large size and mass are their main disadvantages.[76] They are usually combined with a remotely controlled motor otherwise tuned manually.[77] The suitable applications are the long distance communication or radar system that require large power handling capability with low losses.

Ferrites are made out of a mixture of metal oxides and exhibit the general chemical composition of $MOFe_2O_3$ whereas M can be a divalent metal such Nickel, Magnesium, Iron or Zinc.[78] The magnetic dipole moments associated with unpaired electrons will induce anisotropic magnetic properties under a static magnetic field. Magnetically controlled ferrites incorporated systems have very limited uses due to their complexity, high costs, large size, high insertion loss and low tuning speeds.[78] One of the most common magnetically tunable filters is the yttrium-iron-garnet (YIG) filter consists of single crystal spheres and controlled by the change of ferromagnetic resonance frequency with an external applied DC magnetic field.[79] Although mechanically and magnetically tunable filters have distinct advantages, but both exhibit low tuning speeds that is far below the required 1GHz/μs in modern communication systems and both are incompatible with the monolithic microwave integrated circuits due to their bulky size and high power consumption.[80]

Semiconductor technology is a popular and common alternative for fabricating tunable integrated microwave devices. The varactor diode relies on the characteristic of variable capacitance as a function of applied bias voltage and the operation is based upon changing the depletion layer width of the p-n junction under a reverse bias voltage that is similar to varying the distance of between the two plates of a capacitor.[81] The width of the depletion layer increases proportionally with the square root of the reverse bias voltage applied across the diode, thus the capacitance is inversely proportional to the square root of the voltage. GaAs varactor diodes are one of the most favourable for microwave tuning applications in which its capacitance tuning ratio can be increased by controlling the doping concentration within the active

region. Semiconductor diodes have much faster tuning speeds but experience poor power handling, high insertion loss and their Q factor drops exponentially as the frequency reaches around 1GHz, thus confining their applicability only in the low microwave frequencies.[82] The junction noise resulting from the electron/hole collisions in the semiconductor varactor diode and high tuning voltages as a result of the small capacitor area. No semiconductor varactors with high enough Q-factors and tunablitiy have been fabricated for the 10-20 GHz frequency range. (e.g At 50GHz,Q is of the order of 10 or less)[83]

Polysilicon vibrating micromechanical resonators have attracted attention due to their small size, self-switching properties, high Q-factors and compatible integration with the established Si microfabrication processes. The principle of operation is based on the mechanical vibration of the resonator excited and actuated by an external force through electrostatic capacitive transduction. Contour mode spherical resonators have found to be operating at 1.5GHz with a Q-factor of 12000.[84]However, these polysilicon resonators tend to be very stiff and induce large motional resistance at the resonance frequency thus presents an impractical insertion loss of 2.79dB for 0.087% bandwidth 9MHz filter.[85]

At the beginning of the nineties, radio frequency micro-electro-mechanical systems (RF MEMs) were discovered and used for tunable circuits, where the tunability is obtained by the physical movement of a component through electrostatic, electrostrictive or piezoelectric forces that sequentially changes the capacitance of the device.[86-89] They are mechanical structures fabricated on the low cost substrates using semiconductor processing and surface micromachining techniques, which enable batch fabrication to reduce cost and achieves system integration. RF MEMs can be separated into two major types: switches and varactors. Their typical structure consists of two metal contacting plates separated vertically by an air gap and the capacitance is tuned by varying the distance between the two plates through electrostatic manipulation. Due to the mechanical stiffness, the change of the bridge gap is only approximate to one third of its original length, thus the MEMs varactors suffer from low tunabilities of 15% with a typical tuning voltage of 50-100V.[21] While MEMs varactors are superior in Q factor, size, low microwave losses and high linearity compared to semiconductor varactor diode, they also encounters challenges in reliability, expensive hermetic packaging and moderate tuning speeds.

The important parameters and technologies regarding tunable devices are shown in Table 2.4. None of the technologies are absolutely prefect and are dependent on the desired characteristic requirements with the trade off with performance.

Tunable Microwave Technology	**Mechanical**	**YIG Ferrites**	**Semiconductor GaAs Varactor**	**RF MEMS**	**BST Thin Film Varactor**
Tunability	10 to 20%	Multi-Octave	3:1(33%)	2:1(50%)	2:1(50%) to 3:1(33%)
Unloaded Quality Factor	>1000	>500	10 to 40 at 10 GHz	Very High	20 to 100
Insertion Loss(dB)	0.5 to 2.5	3 to 8	2 to 10	2 to 8	3 to 10
Tuning Voltage(V)	-	-	<15	20 to 100	5 to 20
Tuning Speed(GHz/ms)	Very Low	0.5 to 2	1000	100	1000000
Power Handling	Very High	2W	mW	1 to 2W	mW
Power Consumption	High	High	Medium	Low	Low
Size/Weight	Big	Big	Small	Small	Small
IC Integration	Hard	Hard	Good	Good	Good

Table 2.4. Comparisons of different technologies for microwave devices[21, 90-92]

The current semiconductor industry does not have reliable high frequency varactors and it can be replaced by ferroelectric varactors with substantially higher Q-factor at microwave frequency range of 10-20 GHz. Thin film ferroelectric varactors possess high tuning speeds, low power consumption and high dielectric constant ideal for device miniaturization. Extra tunability and enhanced functionalities can be achieved by combining with ferrites, semiconductors to provide electric and magnetic tuning. Present microwave applications of ferroelectric materials are shown in Figure 2.14.

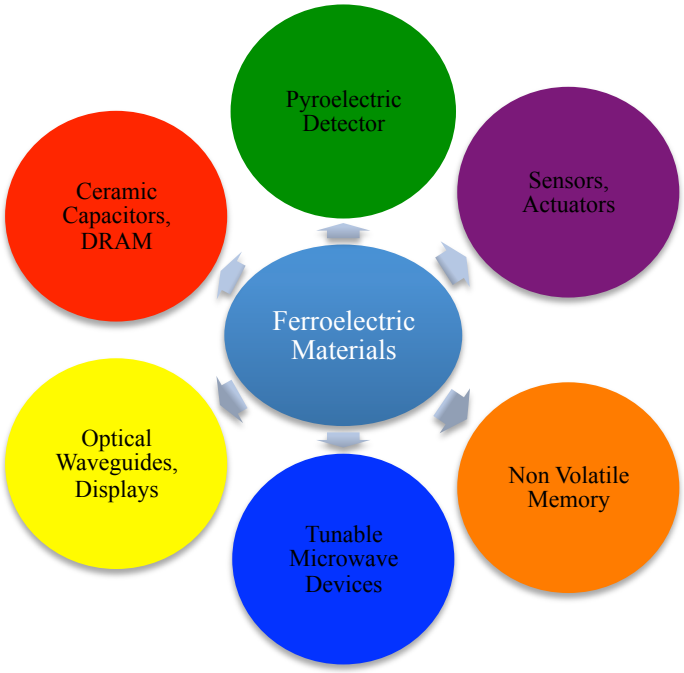


Figure 2.14.Potential Applications of ferroelectric materials

Agile microwave technologies today have the potential to revolutionize the reconfigurable microwave systems industry and develop novel components, devices and systems. Although none of these present technologies is the ultimate solution to the frequency agile problems of all microwave systems, each of these technologies are suitable for their own niche of applications. Nevertheless, the ferroelectrics have a superior number of advantages making them preferable for most of the applications. Figure 2.15 shows the high performance of the bulk acoustic wave resonator in the GHz frequency range and potential future product development in the communications sector compared to the rest of the resonator technologies.

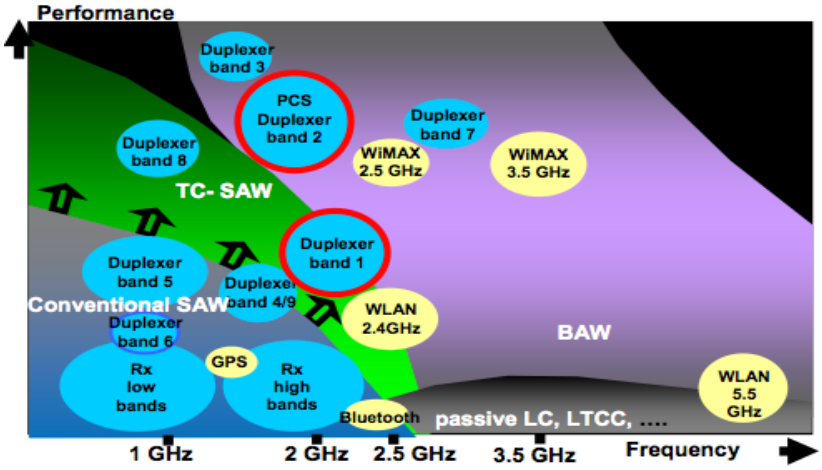


Figure 2.15. Commercial applications relating to SAW, BAW and Temperature Compensated SAW technologies[93]

The quality and dielectric property of these ferroelectric thin films are complex functions of the many parameters such as temperature, frequency, electric field, composition and film thickness. Most importantly, they are also dependent on the processing such as deposition method, substrate, growth conditions, defect density and electrode. The relationships must be clearly demonstrated before any potential commercialization for the microwave applications. This thesis is mainly focused on the study and fabrication of the tunable ferroelectric bulk acoustic wave resonator on silicon substrate. For this purpose, the TFBAR structures are designed and fabricated using pulsed laser deposition and various microfabrication techniques.

2.4 Fabrication Technologies

There are many different methods to fabricate ferroelectric thin films and all of them have their own unique advantages and drawbacks. The method is chosen based on the application, cost and system requirements.

2.4.1 Magnetron Sputtering

Magnetron sputtering is one of the most widely used physical deposition method for growing metallic and ferroelectric thin films. It is highly versatile as it can deposit conductive and insulating thin films onto metal or ceramic substrates. The materials are deposited by physically bombardment of the target material with energetic argon ions. When the target material is conductive, DC power is preferred. RF power can be used for both conductive and insulating materials, which the power supply can generate output power of >100W in the 13.56MHz frequency band and requires a matching network to match the 50Ω output impedance to the input impedance. Once the RF plasma is established, the matching network is automatically adjusted to minimise the reflected power. A plasma discharge is sparked by DC or RF power applied to the target material (cathode), accelerating Ar^+ ions towards the target. The plasma consists of electrons and positive argon ions at a high energy state, where the ions are accelerated towards to the negatively charged target and force the neutral target atoms to be ejected, which are deposited on the substrate placed in front of the target. For growth of oxide materials, reactive sputtering technique is used and oxygen gas is additionally applied with argon to the system. The quality and properties of the oxide thin film deposited by reactive sputtering depends on the substrate temperature, pressure, power, target composition and ratio of partial pressures of Ar and O_2.

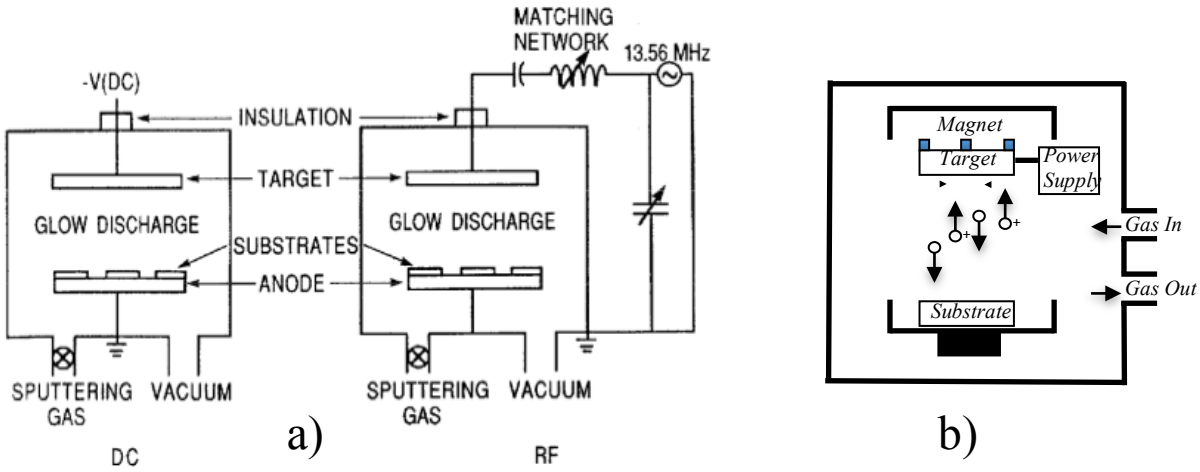


Figure 2.16. a)Difference between the DC and RF Sputtering System, b) the simple schematic of the magnetron sputtering system[94]

Metal thin films are important component of the microelectronics industry due to their high conductivity and stability. They are mainly used for ohmic contacts and good physical adhesion between the substrate and the metal layers to prevent undesired peeling effects. Titanium is widely used as diffusion barriers, buffer layers and interlayers, even though pure titanium is highly reactive metal, it is normally protect by the stable TiO_2. Thin Ti films were deposited on pure Si(100), oxide/Si(100), nitride/Si(100), TiO_xN_y/Si(100), polyimide and glass using R.F magnetron sputtering by Song et.al.[94]Ti films were strongly grown in the (100) direction on pure Si(100),oxide/Si(100) and nitride/Si(100) substrates with an RF power of 200W and Ar flow rate of 100sccm. [94] Ti thin films growth behaviour were influenced by the surface energy and the crystallinity of the substrate. The distance between the target and the substrate can also affect the growth direction. The orientation(100) peak of the Ti films on silicon(100) substrate is more pronounced when the distance is decreased and the direction is highly oriented towards (002) with increasing distance. When the substrate surface energy is low, the (002) orientation is preferred and the (100) orientation is preferred for high surface energy substrates such as silicon or nitride.

Thin gold films deposited on the native oxide of Si(001) substrates by direct current magnetron sputtering were investigated by Ayoub et.al to control the roughness of gold films.[95]The parameters such as deposition rate, target/substrate distance and gas flow mostly affected the morphology of Au. By increasing these parameters, smaller Au particles were produced. Deposition of Au on silicon substrate follows the typical

Volmer-Weber growth mode. The morphology of Au films are characterized as hemispherical grains dispersed uniformly on the surface.

The resistivity of metal thin films such as aluminium, titanium, nickel and molybdenum, zirconium, niobium and tungsten deposited by magnetron sputtering process are strongly dependent on the argon pressure was investigated by Thorton and Hoffman et.al.[96] Figure 2.17 shows the resistivity of titantium films as function of argon gas pressure. Thorton developed a "Zone Model" which relates the argon pressure and substrate temperature to the microstructure of the metal thin films. [96] The resistivity of the metal film is closely related to its microstructure, where the porous structure are likely to increase the resistivity.

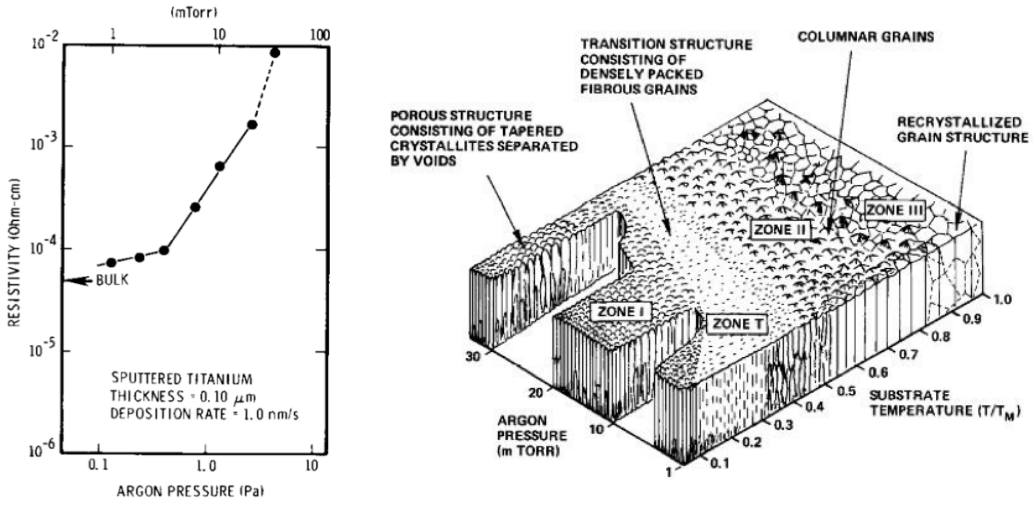


Figure 2.17. a)Electricial resisitivity vs Argon pressure for sputtered titanium films[97] and b)Zone Model showing the influence of argon pressure and substrate temperature on the microstructure of metal thin films[97]

2.4.2 Pulsed Laser Deposition

Pulsed laser deposition has been widely used technique to grow epitaxial thin films of various ferroelectric materials. It is an easy and quick way of fabricating high quality samples for research purposes. The PLD target can be easily fabricated through standard sintering solid state reaction method and the target composition can be mixed using different materials in the powder form, which leads to low cost and fast processing time for making complex thin films.

Pulsed laser deposition is a process where the composition of the target is transferred to the film using a high power pulsed laser inside a vacuum chamber, which forms a plasma plume and the target material will condenses on the substrate surface.[98] The

main advantage of the laser ablation technique is the good stoichiometry transfer from the target material to the film and is highly repeatable, because the vapour plume is identical to that target material regardless of the vapour pressures of the constituent atoms. The technique can be used to deposit in-situ pure elements and multilayer compounds with relatively high deposition rate. The deposition flux can be instantaneously varied independently of the average growth rate and the kinetic energy of the ablated species. There also exist drawbacks such as large particulate/droplets formation on the film surface due to laser pulse interaction with the target, thickness inhomogeneity due to the focused pulsed laser beam and substrate size.

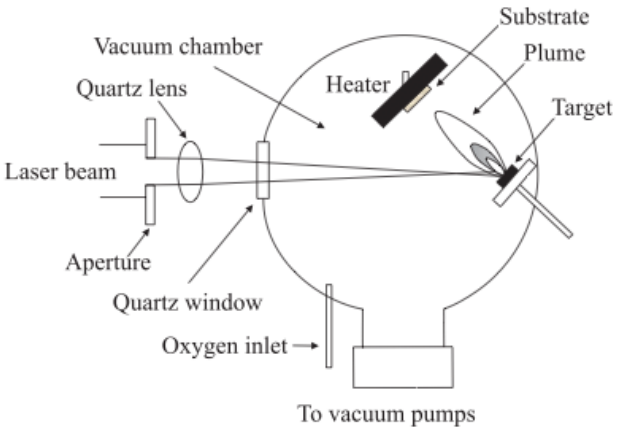


Figure 2.18. The instrument setup of a pulsed laser deposition system[99]

Many ferroelectric devices containing $SrTiO_3$ and $Ba_xSr_{1-x}TiO_3$ have been fabricated on different substrates using pulsed laser deposition. The microstructure and physical properties of BST and STO films can be easily tailored by the growth parameters such as temperature, oxygen partial pressure, and laser energy during PLD. The typical growth conditions for BST thin films are at temperature of 750℃, laser fluence at target of $1.5Jcm^{-2}$ and oxygen partial pressure of 0.1mbar.[99]To study the dielectric properties of STO thin films, it was grown on single crystal $LaAlO_3$ substrate with $SrRuO_3$ electrodes using pulsed laser deposition. The typical deposition conditions were excimer laser density of $1\text{-}1.5Jcm^{-2}$, substrate temperature of 720-780℃, oxygen pressure during deposition of 100mTorr and cooling rate of deposited film in 500Torr oxygen to room temperature. [54]

A $SrTiO_3/SrRuO_3/CeO_2/YSZ$ multilayer structure have been grown in-situ on silicon substrate by PLD technique using a KrF excimer laser with laser fluency of $1.5Jcm^{-2}$.[53]No oxygen was introduced to the vacuum chamber during the deposition of the

YSZ buffer layer to avoid further growth of the native SiO_2 on the Si substrate. The oxygen pressure during the deposition of CeO_2, $SrRuO_3$ and $SrTiO_3$ was at 0.4mbar. The growth temperatures, thickness of layers and bulk lattice parameters of the multilayer structure were summarized in Figure 2.19. The samples were cool down to room temperature at oxygen pressure of 400mbar.

Layer	YSZ	CeO_2	$SrRuO_3$	$SrTiO_3$
T_d, °C	770	720	780	700
t, nm	50	10	50	100
a, nm	0.514	0.541	0.393	0.3905

Figure 2.19. Growth temperatures T_d, thickness t and lattice parameters a of the multilayer structure[53]

2.4.3 Silicon Substrate Patterning

Substrate micromachining is one of the key processes required for fabrication of advanced MEMs systems. It is achieved through etching using either dry or wet methods, although wet etching of silicon using alkaline solutions is not capable of transferring complex geometries with accurate dimensional control (not reproducible) and rate is dependent on the crystal plane orientation. Dry etching is well established in the semiconductor industry to etch depths of only a few microns without any orientation restrictions, but it is lacking in mask selectivity and etching rate. The differences between these two methods are shown in Figure 2.20.

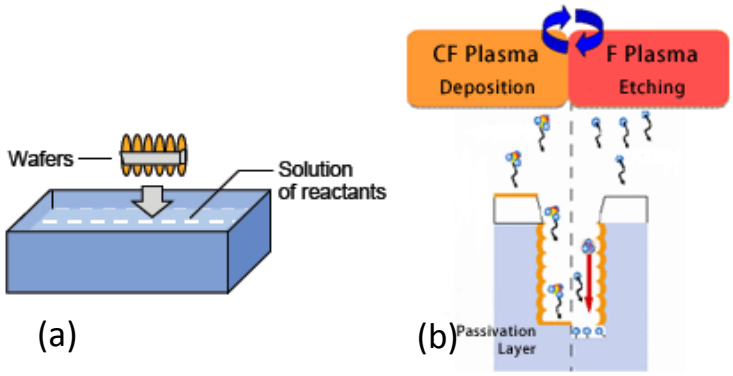


Figure 2.20. Difference between the a) Wet Etching[100] *and b) Dry Etching techniques*[101]

The most used isotropic wet etching for silicon is the HNA mixture of hydrofluoric acid (HF), nitric acid (HNO_3) and acetic acid (CH_3COOH) and its etch rate is from 1 to 3µm/min.[100] The nitric acid drives the oxidation reaction of silicon, while the fluoride ions of the HF acid form soluble silicon compound H_2SiF_6. The acetic acid

prevents the dissociation of the nitric acid into NO_3^- or NO_2^- and the oxidation of silicon is slowed down without acetic acid. However, the same mixture without the acetic acid can only be effectively used for shorter etches until the NO_2 is depleted. The overall chemical reaction is[102]

$$18HF + 4HNO_3 + 3Si \rightarrow 3H_2SiF_6 + 4NO_{(g)} + 8H_2O \quad (2.49)$$

There are also wet etchants that can achieve anisotropic etching profile such as Potassium hydroxide, KOH and Tetramethyl ammonium hydroxide, TMAH. The overall chemical reaction[103] of silicon with alkali hydroxide etchants is

$$Si + 2OH^- + 2H_2O \rightarrow SiO_2(OH)_2^{2-} + 2H_2 \quad (2.50)$$

The wet etch rates is dependent upon the crystal plane orientation of silicon and can differ by a factor of 200 in KOH etching, where fast etching is experienced in (100) crystal planes and (111) planes show slow etching. The etch rate for a KOH etchant of 50wt% concentration at 80°C is around 1.4μm/min for (100) crystal plane.[102] Potassium hydroxide etching solution is usually used at concentrations above 20% due to the high surface roughness and formation of potential insoluble precipitates. For heavily doped silicon regions, the etch rate is also slowed down, because the width of the space-charge region layer at silicon surface is decreased due to doping, which leads to rapid recombination of electrons generated by the oxidation reaction. This decrease in electron availability limits the reduction of water molecules to form OH^- ions which is crucial to the etching reaction. The TMAH etchant can be used as an alternative to alkali hydroxide, because it contains no alkali ions which can be detrimental to CMOS integrated circuits.[103] However, the surface morphology is rougher and the selectivity is lower than for the alkali hydroxides at the Si etch rate of 0.5-1.5μm/min. Different masking layers such as silicon nitride and silicon dioxide are compatible with both alkali hydroxide and ammonium hydroxide etchants. An oxide thickness of 2μm is required for through wafer etching in KOH and 200nm is sufficient for TMAH etchants. The wet etching rate is a function of temperature, loss of reactive species, loss of liquids to evaporation, mixing, applied potential, contamination and so on.[103] Thus, the etch rate of wet etching is poorly controlled and not well reproducible.

Dry etching using chlorine based plasma creates silicon microstructures with high accuracy, but the etch rate is typically below 1μm/min and the selectivity is in the range of 20-30:1 for silicon dioxide masks.[101] Thus the fluorine radicals have

replaced the chlorine, because the fluorine radicals can readily etch silicon without any need for ion assistance, but the etch is no longer directional as a consequence. Silicon etch rates of 2.0-3.6μm/min was obtained in an CF_4 only plasma at high pressures (0.5-1.5Torr) and the etch rate was increased even further by addition of 20% Oxygen into the CF_4 plasma, which can be useful for deep trench etching applications.[104] But at a higher O_2 content, a passivating inorganic $Si_xO_yF_z$ film is formed on the Si surface and the etch rate is controlled by the thickness of this layer rather than the F-atom density, so the etch rate decreases. Si etch rate of 0.36μm/min by using a microwave discharge of $Ar/CF_4/O_2$ at low power of 80W, where the etch rate was increased by a factor of 8 with the addition of oxygen and by a factor 23 with the addition of argon.[105] Small amount of inert Ar^+ ions from the Argon+CF_4 plasma are accelerated towards the silicon at the cathode due to built-in electric field and enhance the chemical reaction in reactive ion etching.

The reaction involved in the chemical part of reactive ion etching is illustrated,

$$e^- + CF_4 \rightarrow CF_3^+ + F^* + 2e^- \qquad (2.51)$$

$$Si + 4F^* \rightarrow SiF_4 \qquad (2.52)$$

The most commonly considered processing variables of dry etching are pressure, power, gas flow and masking material, while doping of silicon, temperature, reactor cleanness and loading effect of the material surface are often missed. The etch rate of *n*-type Si is higher than intrinsic Si which etches faster than *p*-type Si, because the Coulomb attraction between the uncompensated donors in the N type and the reactive halogens will enhance the etch rate, whereas the Coulomb repulsion in the *p*-type will lower the etch rate.[106] There are two types of dry etching equipments and they are illustrated in Figure 2.21. The Inductively Coupled Plasma etcher uses much higher power than the Reactive Ion Etcher, thus its etch rate is also much higher.

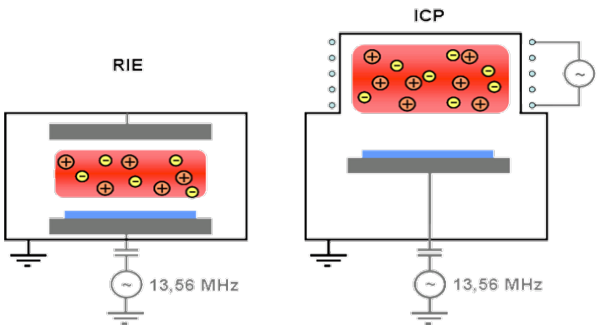


Figure 2.21. The system schematic of Reactive Ion Etcher and Inductively Coupled Plasma Etcher. [101] [107]

Bosch deep silicon etching was developed to achieve high etching rates and anisotropic structures.[101] The Bosch deep silicon etching process uses SF_6/C_4F_8 as the etchant and passivation step gases and they are alternated to avoid recombination of active species in the gas phase. Kiihamaki *et.al*[107] reported the deep silicon etching process using inductively coupled plasma reactor with SF_6/C_4F_8 pulsed processes and achieved the maximum etch rate of 7 µm/min for low aspect ratio structures. The etched rate per pulse is from 0.2-2µm with pulse lengths of 5-13s. Silicon dioxide and photoresist were used as masking materials. Figure 2.22 shows the typical processing conditions and results from different etch processes. An average Si etch rate of 5 µm/min is produced for 400 µm deep features by ICP reactor using the Bosch setup.[107]

Process	Low	Medium	High
Pressure (mtorr)	15	45	40
SF_6/C_4F_8 pulse ratio	1 : 1	1 : 1	1.85 : 1
max ER (128 um feature)	1.6	3.5	7
ave ER ($AR = 10 : 1$)	1.35	3.2	4.85
Si : ox selectivity	150 : 1	700 : 1	250 : 1
Photoresist selectivity	80	NM	NM
Undercut (micron)	0.25	1	2
Sidewall profile (angle)	positive	vertical	retrograde/barrel

Figure 2.22. Results of deep silicon etching from different etching processing conditions. [107]

2.4.4 Device Patterning

The microelectromechanical systems devices are usually patterned using a reproducible process called Photolithography. It transfers a pattern from a photomask to the surface of a film or a substrate using light exposure.[108] This process was initially used for reproducing engravings and photographs, and later become the ideal process for mass production of integrated circuits. The whole device patterning process is carried out within a clean room where the amount of atmospheric dust and contamination is strictly controlled. The mask alignment and exposure system can be divided into contact, proximity and project types depending on the optics used to transfer the pattern to the sample. There are three types of mask alignment systems used for device patterning shown in Figure 2.23 and the basic steps of device patterning also included.

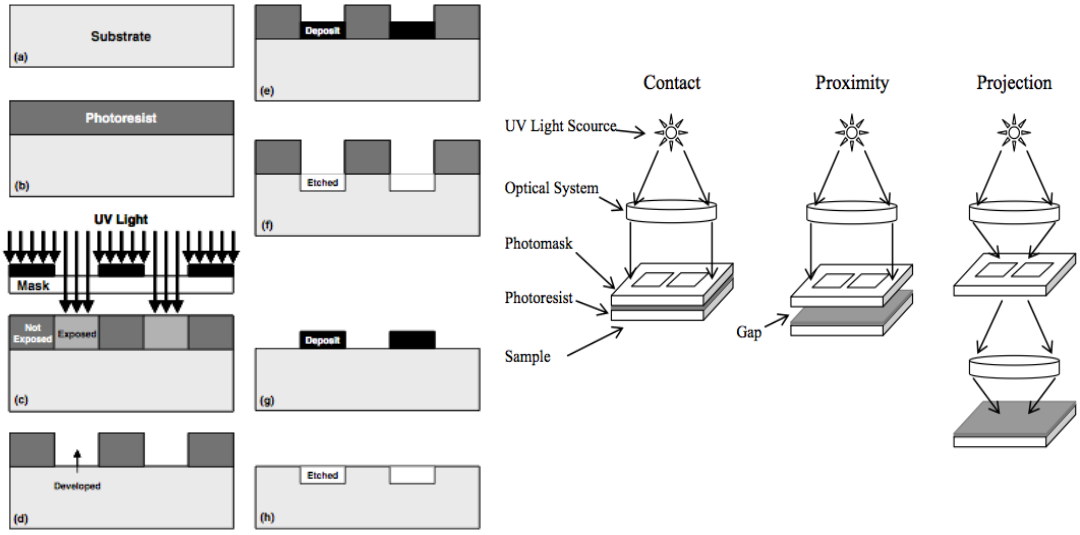


Figure 2.23.Contact, Proximity and Projection Alignment Systems[109]

For typical silicon etching processes, contact printing and stepper are frequently used for pattern lithography to enable ICs and MEMS to be produced reliably with microscopic dimensions and in high volume.[107, 109] Contact lithography involves a mask being in contact or near proximity with a substrate to be patterned. In this lithography technique, the resolution and the quality of pattern transfer is limited by the diffraction of light, wafer flatness and debris between the substrate and the mask.[110] Silicon etched in the reactive ion etching reactor were patterned with 1.5 µm thick photoresist using the contact mask aligner with UV source and developed using AZ400K developer.[111] The resolution of contact photolithography can be extended to 100nm lines or below using a conformable embedded amplitude mask of a trilayer resist stack and deep UV radiation source with the wavelength of 220nm. The exposure latitude was measured to be around ±20% for ±10% linewidth control.[112] Miyajima *et.al*[113] has reported high aspect ratio photolithography using positive photoresist and conventional contact mask aligner with standard UV light source. Minimum linewidth and spacing of 3.5 µm and µm respectively, and a maximum aspect ratio of 7.7 was achieved using 23 µm thick multilayer photoresist.[113] Intimate contact between the mask and substrate is found to be most critical for high resolution photolithography, thus the edge bead removal process was applied.

The ion beam milling process is the next step in device patterning after photolithography. It is a process that uses accelerated submicron inert ion particles to remove the atoms of material while the sample is mounted to a rotating holder inside

a vacuum chamber. An atom at the surface is ejected when the energy transferred to the atom in the collision process exceeds the chemical binding energy, which is characterized by value of incident ion energy required for the removal of an atom, typically in the range of 5-40eV. Prior to ion beam milling, photoresist material has been deposited onto the sample, because the ion beam will physically etch away everything to which it is exposed. The etching rate of the photoresist material is much lower than that to the material which is desired to be etched, for example, metal's etching rate is between 3 to 10 times faster than the etch rate of photoresist in the ion milling process. The detailed schematic drawing of an Ion beam milling system is shown in Figure 2.24.

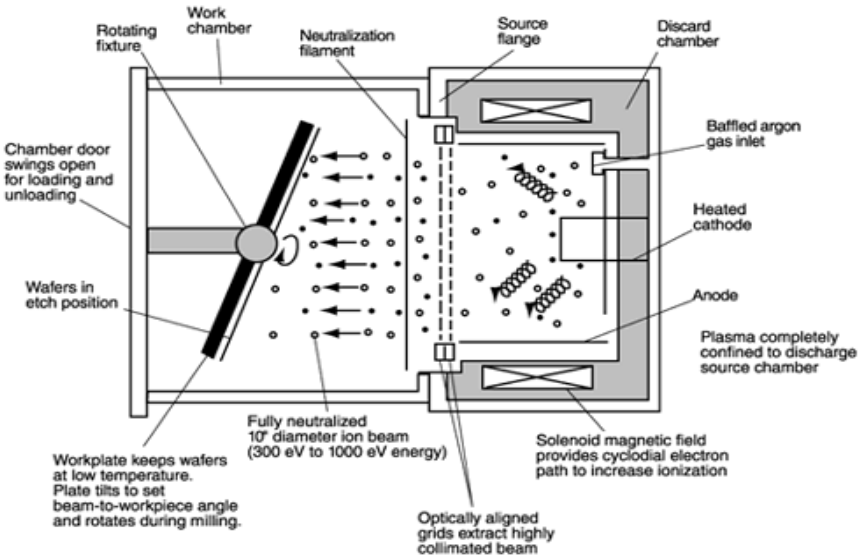


Figure 2.24.Ion Beam Milling System Schematic[114]

Ion beam milling is a process that can offer solution to materials that are difficult to etch and patterned down to submicron dimensions with highly accurate control. This process exhibit high etch resolution with no mask undercut and the ability to etch any material or multilayer combinations and the ability to control the profiles of etched sidewalls. [115] The most important property in ion etching is the sputter yield, which is defined as the number of sputtered target atoms per incident ion. This property depends on the material being etched, bombardment energy and angle of incidence. Somekh demonstrated the ion beam etching rates of several materials and resists vs. the angle of incidence relationship while the accelerating voltage was 500V and 0.6mA/cm^2 beam current density, which is shown in Figure 2.25. [116]

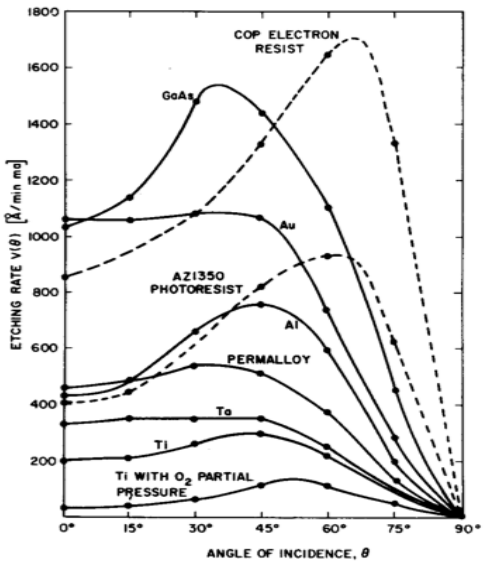
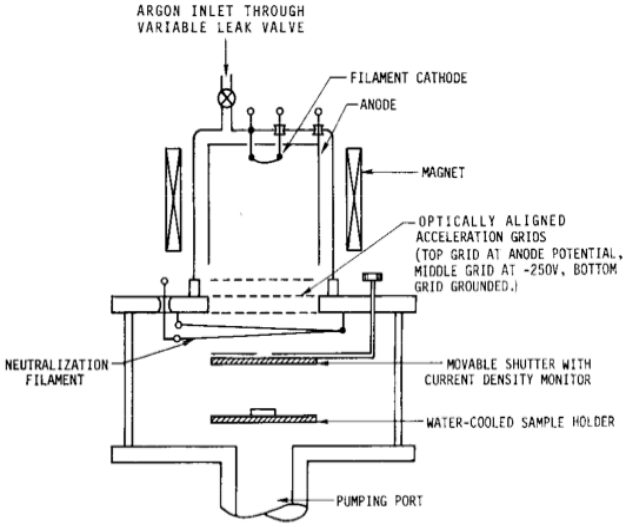


Figure 2.25. The etching rate of different materials vs. the angle of incidence during ion beam milling.[116]

Gloersen demonstrated the ion beam etching rates of several different materials using argon ions in Kaufman type ion source. The materials were etched at normal incidence, 1mA/cm^2 beam current density and accelerating voltage of 500V.[117] The ion milling rate of different materials are compared in Figure 2.26a and the setup of the Kaufman type ion beam etch system is shown in Figure 2.26b.

Material	Etching rate [Å/min]
SiO_2 crystal {001}	330
Gd–Ga garnet	280
GaAs{100}	650
Si{100}	215
Al_2O_3{1$\bar{1}$02}	83
Soda–lime glass	200
SiO_2 (evaporated film)	280
W (bulk)	180
Al (bulk)	300
Stainless steel 304 (bulk)	250
Ta (bulk)	150
Mo (bulk)	230
Cu (bulk)	450
Permalloy (film)	330
Shipley AZ1350 photoresist	200
Riston 14 photoresist	250



(a) (b)

Figure 2.26. A)Ion beam etching rate of different materials and b)Kaufman type ion beam etching system[117]

2.5 Characterisation Techniques

Quality control and inspection is one of the most important parts of the research. Several different characterisation techniques are used to examine the microstructure and material properties of ferroelectric thin film deposition, metal thin film deposition and silicon substrate micromachining. A brief overview will include the given capabilities and limitations of the techniques used in this PhD thesis.

2.5.1 Optical Microscopy

A compound light microscope is a microscope that uses multiple lenses to collect light from the sample and separate exchangeable objective lenses to focus the light into the eye or camera. They are superior than the single lens microscope in terms of improved numerical aperture, reduced chromatic aberration and adjustable magnification. The setup of a transmission and reflected light microscope is shown in Figure 2.27.

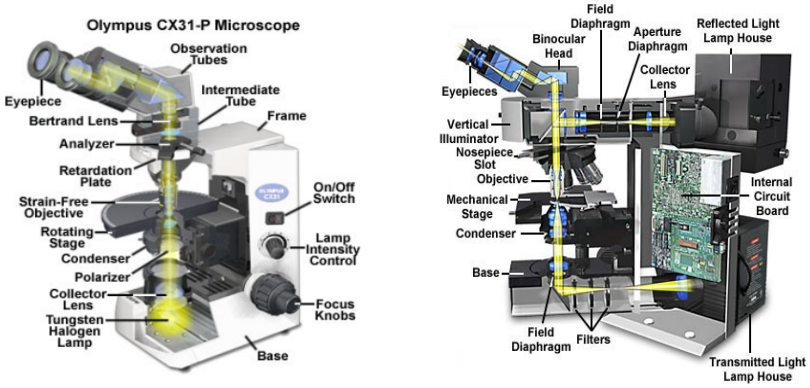
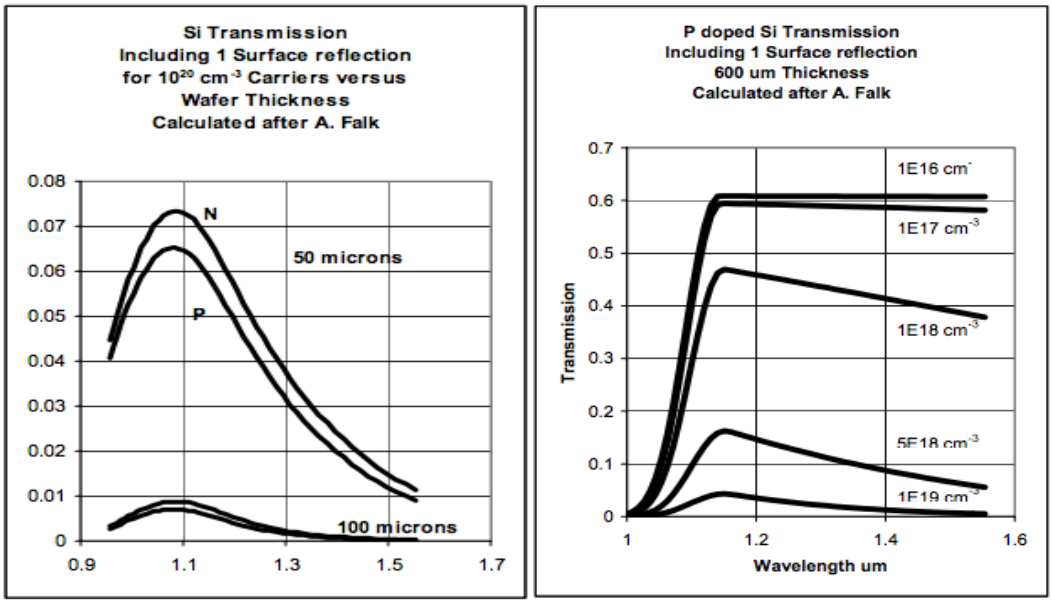


Figure 2.27. The schematic of transmission and reflection optical microscope[118, 119]

Light microscopy is a quick and accurate method for characterising surface of the Si MEMS structure and thin film samples.[118, 119]Aw et.al[120] investigated the absorption measurements on the heavily doped silicon and the undoped silicon, where the heavily doped silicon is much less transparent due to the free carrier absorption and scattering of light. Falk et.al developed an empirical method for calculating absorption for doped silicon. Typical reactive ion etching techniques produce a silicon surface with a very low reflectivity known as black silicon, thus introduce difficulty towards the characterisation of etched silicon structure.[121]



(a) (b)

Figure 2.28 a)Si transmission improves with wafer thinning ,b)P-type doped Si transmission decreases with increasing carrier concentration. Calculated both by A.Falk.[122]

Light microscopy has a resolution limit defined by $0.61\frac{\lambda}{\mathrm{NA}}$, where NA(Numerical Aperture) is a property of the objective lens determined from its magnification, diameter and refractive index. Visible light has an average wavelength of approximately $0.5\,\mu\mathrm{m}$, which makes the resolution to $0.2\ \mu\mathrm{m}$. The relationship between the resolution limit and the wavelength of illumination is applicable for any form of radiation. Electron particles travel near the speed of light as a wave and their wavelength is inversely proportional to the electron's velocity, thus the resolution can be increased by examining a specimen with high velocity electrons.

2.5.2 Scanning Electron Microscopy

Scanning electron microscopy(SEM) is a powerful analysis tool for examining the microstructure and composition of materials in high resolution and is widely used all research areas. It was made in the 1930s to overcome the limitations of optical microscopy and to increase the magnification and resolution to a much higher standard. [123] The principle of a SEM is based on the interaction between an incident electron beam and the sample specimen. Different signals are produced due to the interaction between the electrons and the sample such as backscattered electrons, secondary electrons, Auger electrons and characteristic X-rays.[123]

Scanning electron microscopy is commonly used for characterizing silicon MEMs structures, thin film morphology and nanostructures, because it has minimum resolution of 5nm that is applicable for almost every microfabricated structures.[124]Due to the low reflectivity of the black silicon etched by reactive ion etching techniques, SEM is used to characterize the etch profiles.[121]The surface morphology of the thin films grown on various substrate can be analysed using SEM, which shows any surface features in amorphous or crystalline films. [125] Most of the electrons are scattered at large angles from 0° to 180° when they interact with the positively charged nucleus. The two most common signals used to generate SEM images are the secondary electrons (SE) and backscattered electrons (BSE). The backscattered electrons are produced when an incident electron collides with the nucleus of the surface atom and are elastically scattered. The production of BSE electrons varies directly with the atomic number, thus the backscattered electron images can be used for identifying sample atomic number. Some electrons are scattered inelastically due to the loss in kinetic energy upon the interaction with orbital shell electrons and remove loosely bound conduction electrons from the sample. They are known as the secondary electrons and are widely used for SEM topographical images. Both SE and BSE signals are collected when a positive voltage is applied to the collector screen in front of the detector. When a negative voltage is applied, the only BSE signal is obtained as low energy SEs are repelled. Then, the electrons captured by the detector are amplified and used to from an image in the SEM.

As a result of secondary electron generation, a vacancy is left in an ionised atom's electron shell. An electron from a higher energy outer shell from the same atom can fill this vacancy and the excess energy produced by reshuffling electrons to fill the shell vacancies can emit Auger electrons.[126] Auger can be used to give compositional information of the sample but the kinetic energy is relatively low and only emitted from shallow sample depths (<3nm). X-rays are also produced by the interactions of the incident electron beam with the sample surface. This X-ray has a characteristic energy unique to the element from which it is originated from and thus can be used to provide compositional information about the sample.

An SEM is made of three main parts: electron column, detection system and view system. The setup is shown in Figure 2.29. The electron beam produced by the electron gun is converged into fine beam via the electromagnetic lenses (condenser

and objective lenses). Then a scan signal is applied to the deflection coils and the electron beam is scanned along the sample surface. The specimen chamber can be equipped with a specimen stage and several detection equipment such as specimen goniometer, secondary electron detector for detecting signals from the sample, backscattered electron detector and X-ray detector. All components of the SEM system must be kept at high vacuum pressure to reduce the possibility of contamination from air molecules.

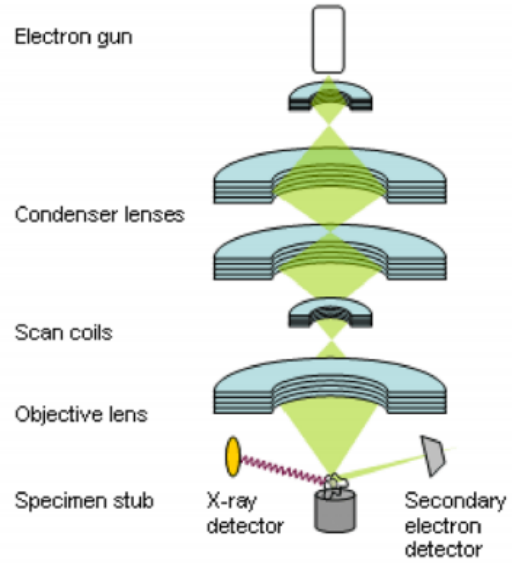


Figure 2.29. The schematic diagram of a scanning electron microscope[123]

2.5.3 X-Ray Diffraction

X-ray diffraction(XRD) is one of primary techniques for characterisation the crystal structure of materials. The wavelength of an X-ray source is on the order of Angstroms (10^{-10}m), which is similar to the interatomic spacing in solid materials.[127] When X-rays interact with a material with regular and repeating arrangement of atoms, a diffraction pattern is generated from this interaction. This diffraction pattern is directly related to the crystal structure of the material under observation. Each crystalline material has a unique atomic architecture and consequently has a unique X-ray pattern, so it can be used to identify materials.

XRD provides structural information such as crystal orientation, texture and grain size for samples from hundreds of micrometres thick to tens of nanometres thin.[128]In XRD characterisation, the θ-2θ scan is carried out to provide these structural information as the incident angle θ is varied and the detector angle for the diffracted beam is simultaneously moving at 2θ. Figure 2.30 shows a typical θ-2θ scan of PLD

deposited BST and STO thin film on a Si(100) substrate with Pt electrodes. The STO and BST thin films were grown in the (110) preferential orientation to the substrate.

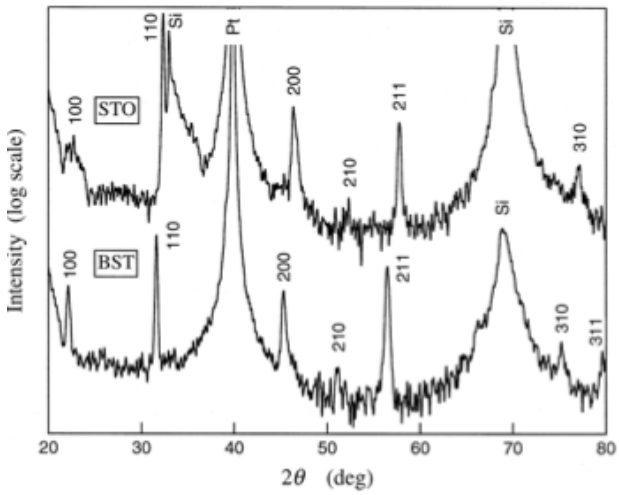


Figure 2.30. XRD diffraction pattern for STO and BST films grown at 400℃ and 500℃.[129]

The setup of the X-ray diffraction is shown in Figure 2.31. When a parallel beam of X-rays of wavelength λ is incident on the sample at an angle θ to the surface and interact with atoms in two lattice planes, the constructive interference occurs when the path difference between the diffracted beams are equal to a whole multiple of wavelengths.[130]This diffraction condition is known as the Bragg's Law, which can be expressed as

$$n\lambda = 2d\sin\theta \qquad (2.53)$$

where n=an integer, λ=the wavelength of the X-rays, d= the spacing between 2 atomic layers, θ= the angle between incoming X-rays and the atomic layer.

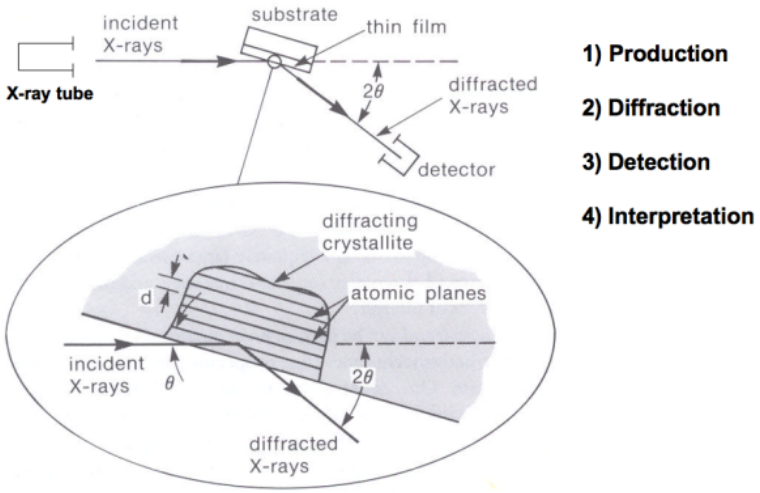


Figure 2.31. An X-ray beam scan process and relationship to Bragg's Law[130]

Therefore, given the wavelength λ of the X-ray source, and the measured angular position θ of a diffraction peak, the interplanar spacing d of a set of crystallographic planes in a crystalline material can be calculated.

Conventional $\theta - 2\theta$ scans of the ferroelectric thin films were performed in a PANalytical X'Pert Pro diffractometer equipped with a Cu $K_{\alpha 1}$ hybrid monochromator, incident beam optics and a receiving slit/analyzer crystal in the diffracted beam optics. The sample stage can accommodate samples from three inch sized wafers to 150mm diameter and provides x-y mapping capability. This equipment is mainly used for determination of the crystallographic orientation and quality of crystalline thin films.

2.5.4 Profilometry

The profilometry technique was chosen to characterize the etch depths of the silicon MEMs structure and thin film thickness, because it is a quick and accurate method to measure thickness from thin and thick film step heights ranging from below 1nm upto 90mm. It is based on the physical contact measurement of the sample using a stylus and the vertical displacement of the stylus is converted into a height value in Z equivalent to the step height in the feature studied. The sample is placed in a *X*, *Y*, θ stage controlled by manual knobs. The setup of the stylus profiler is shown in Figure 2.32. Ray *et.al* characterized the step height and the etch rate of single crystalline silicon substrates that have been etched using CF_4,SF_6 and CHF_3 to investigate the processing parameters on the etch rate of Si.[104] Sengupta *et.al* measured ferroelectric BSTO thin films fabricated using pulsed laser deposition using a Dektak 200 profilometer. [131] Ito et.al also used profilometer to characterize the SRO thin films prepared by laser ablation on the quartz substrate. [132]

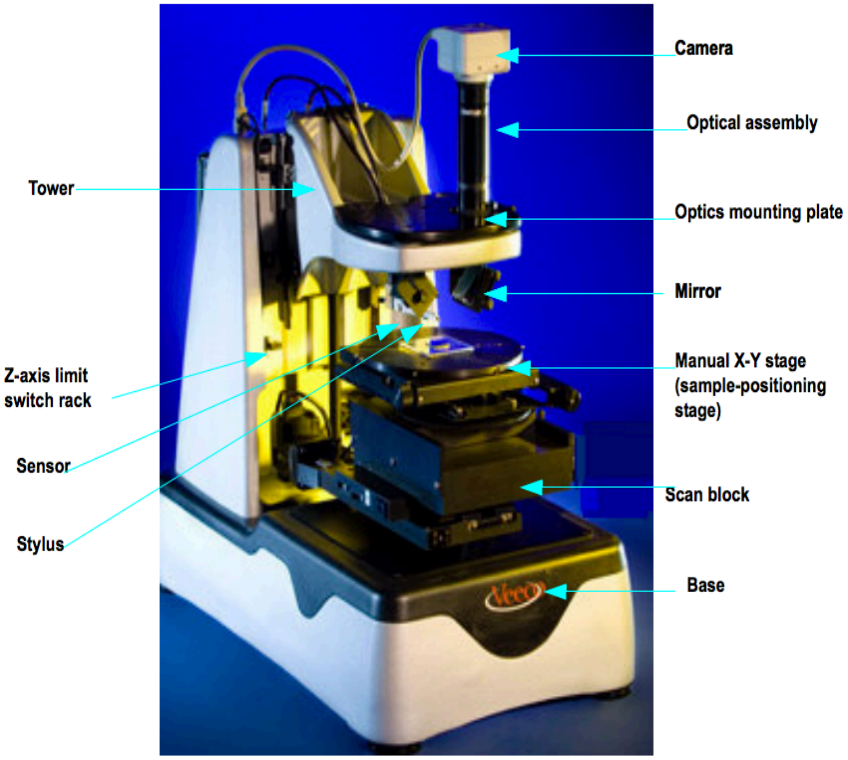


Figure 2.32.The schematic setup of a contact stylus profilometer[133]

To setup a surface scan, the scan parameters such as length, speed, sampling rate and the force applied to the sample surface must be selected carefully prior to measurement. Apart from these scan parameters, the environmental noise can also affect the accuracy of the contact profile measurement. Due to factors such as surface roughness, equipment vibration and possible stylus penetration, a minimum 1% error in the step height measurement can be expected between successive scans. The specification of a stylus profiler (e.g Dektak 150) is shown in Table 2.5.

Stylus Profiler System Specifications	
Stylus Force	1 to 15mg with LIS 3 sensor
Stylus Radius	2.5 μm
Scan Length Range	55mm standard
Sample Stage	Manual X/Y/θ operation,100×100mm X-Y translation, 360° rotation, manual levelling, 1 μm repeatability, 0.5 μm resolution
Maximum Sample Thickness	Upto 90mm
Maximum Wafer Size	150mm
Vertical Range	524 μm
Step Height Repeatability	≤ 6Å
Vertical Resolution	1Å max. (at 6.5 μm range)

Table 2.5. Typical Specifications of a Stylus Profiler[133]

2.5.5 Electrical Characterisation

The electrical characteristics of a ferroelectric thin film device can be extracted in forms of complex dielectric constant and tunability using different types of techniques, such as the direct methods, waveguide methods and resonance methods. The choice of measurement techniques and corresponding system setups are dependent on the frequency range and the form of interest of the ferroelectric material. For measurement at frequencies below the radio frequency, any form of ferroelectric tunable capacitor can be modelled as lumped elements since its dimensions are much less than the wavelength of the electromagnetic signal. The capacitance and loss tangent of this capacitor can be measured directly by a standard impedance analyzer. However, when the measurement is performed at microwave frequencies, the devices can no longer be modelled as lumped elements due to comparable capacitor dimensions with electromagnetic signal length and parasitic effects. Thus, the waveguide and resonance methods are favoured in this scenario.

The parallel plate or planar capacitors are the most commonly used structures to characterise the dielectric properties of ferroelectric materials with frequency and electric field. The various types of ferroelectric capacitor structures are shown in Figure 2.33.

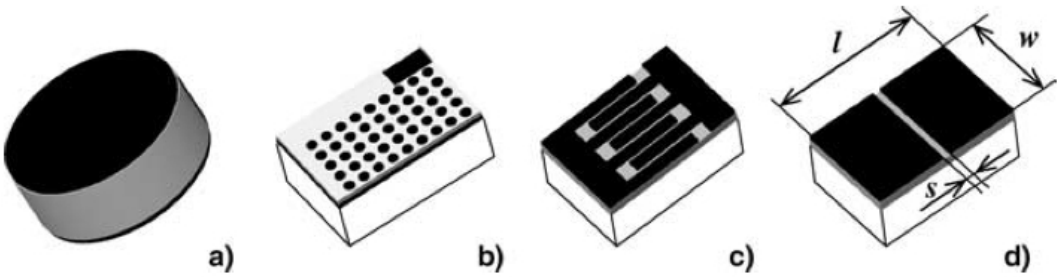


Figure 2.33. Different types of ferroelectric capacitors-a) parallel plate capacitor, b)array of thin/thick film parallel plate capacitors, c)interdigital capacitor, d) air gapped planar capacitor[13]

At low frequencies, the parallel plate capacitor structures in Figure 2.33 a) and b) can be represented by a equivalent electrical circuit of a capacitance C_p and a frequency dependent resistance R_p connected in parallel and a series resistance R_s relating to the losses in the electrodes. The impedance analyzer can measure the capacitance and loss tangent at frequencies below a few MHz, but a network analyzer is used instead at higher frequencies to measure the complex reflection coefficient.

The loss tangent and capacitance of the ferroelectric capacitor are calculated from the equation 2.54, [13]

$$\tan\delta \cdot \omega C + j\omega C = \frac{1}{Z_0}\left(\frac{1-S_{11}}{1+S_{11}}\right) \qquad (2.54)$$

where ω is the angular frequency of the A.C field, C and tan δ are the capacitance and loss tangent, Z_0=50Ω.

The electrodes loss (R_s) can be calculated by subtracting the conducting loss using the equation 2.55,

$$\tan\delta_e = \tan\delta_{Measure} - \omega R_s C_p \qquad (2.55)$$

where $tan\delta_e$ and $tan\delta_{Measure}$ are the loss tangent of the ferroelectric material and the measured capacitor. [13]

To study the dielectric properties of the ferroelectric material in a parallel plate capacitor, the capacitance and the loss tangent tanδ is measured using an LCR meter. The expression relations are:

$$C = \varepsilon_0 \varepsilon_r \frac{A}{d} \qquad (2.56)$$

$$\tan\delta = \frac{\varepsilon'' + \frac{\sigma}{\omega}}{\varepsilon'} \qquad (2.57)$$

$$\varepsilon(\omega) = \varepsilon'(\omega) - i\varepsilon''(\omega) \qquad (2.58)$$

where ε_0 is the dielectric constant at free space, $\varepsilon_r$is the relative dielectric constant, A is the electrode area, d is the thickness of the ferroelectric film,σ is the conductance, $\varepsilon'(\omega) = \varepsilon_0\varepsilon_r$ and $\varepsilon''(\omega)$ are the real and imaginary parts of the dielectric constant.

The planar capacitor structures in Figure 2.33 c) and d) is slightly more complicated and the electric field distribution between the ferroelectric, substrate and air must be included in the model. The capacitance can be calculated from the following expression, [13]

$$C = \varepsilon_0 w \left[\frac{2}{\pi}\ln\left(\frac{4l}{s}\right) + \frac{\varepsilon_3 - 1}{\pi}\ln\left(16\frac{h_3+h_2}{\pi s}\right) + \frac{\varepsilon_2-\varepsilon_3}{\frac{s}{h_2}+\frac{4}{\pi}\ln 2}\right] \quad (2.59)$$

where ε_2 and ε_3 are the relative dielectric constants of the ferroelectric and the substrate, h_2 and h_3 are the thickness of the ferroelectric and the substrate, l is the capacitor length, s is the electrode gap and w is the capacitor width. [13] This equation 2.59 was derived for ferroelectric capacitors and it provide some 1-2% accuracy on condition that $h_2 < s \leq 10h_2$, $s \leq 0.25l$, $s \leq 0.5h_3$, $\frac{\varepsilon_2}{\varepsilon_3} > 100$ reported by Vendik *et.al.*[134]

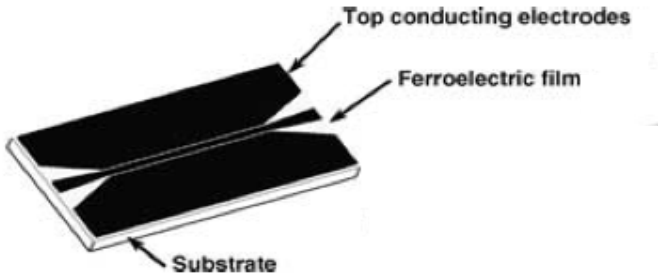


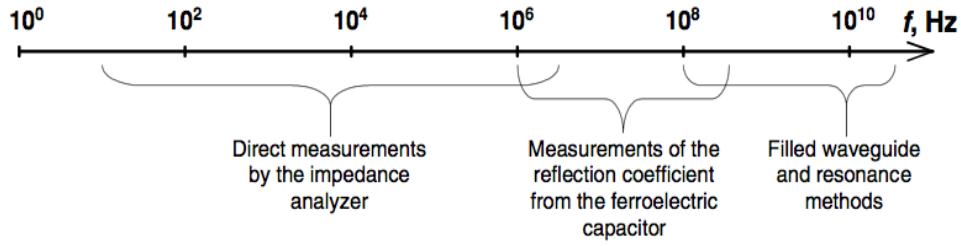
Figure 2.34. Coplanar transmission line structures patterned on ferroelectric film[13]

The transmission line structures such as coplanar waveguide can be used for characterization of both thick and thin ferroelectric materials, where the scattering matrix of a transmission line is patterned onto the ferroelectric film. This measurement technique is drawn in Figure 2.34. The impedance of the transmission line need to be closed to 50Ω to reduce the signal reflection and can be modelled by full wave analysis. The permittivity parameter is extracted from the measured scattering matrix using conformal mapping.

The electrical measurement techniques presented in this section each have its limitations and applicability over a large range of frequencies. They are chosen based on many parameters such as the frequency, linear sample dimensions and instrumental errors. Figure 2.35 a) shows the various methods used for different

frequency ranges and b) shows the instrumental errors and limits of each characterization methods.

a)



b)

Methods	Instrumental errors	Limits
Direct capacitor measurements		
Capacitance	0.05–0.1%	$10^{-17} < C\,[F] < 10$
Loss tangent	0.0005–0.001%	$10^{-6} < \tan\delta < 10$
		$f\,[Hz] < 10^6$–10^8
Characterization of the capacitor through the measurements of the reflection coefficient		
Capacitance	2–5% (HP8722)	$0.005 < \omega C < 0.05$
Loss tangent	5–6%	$0.0005 < \omega C \tan\delta < 0.02$
Waveguide and transmission line methods		
Absolute error for the phase	<5 degrees	$f\,[GHz] > 0.5$
Absolute error for the transmission coefficient	<0.02	length of the line: $l\,[m] > \frac{2}{f\,[GHz]\sqrt{\varepsilon}}$
Resonance methods		
Capacitance or dielectric permittivity	<1%	10^{-4}–$10^{-2} < \tan\delta < 0.1$
Loss tangent	~ 5%	$0.05 < C\,[pF] < 1$

Figure 2.35. Frequency range applicability for each measurement techniques and the associated instrumental errors/ limits[13]

To study the electrical properties of the thin films and the fabricated devices, the following methods are used,

- Current-Voltage Measurement
- Capacitance-Voltage Measurement
- Resonance Measurement

2.5.5.1 Current Voltage Measurement

The DC current voltage measurement was performed using a setup of a probe station and an Agilent semiconductor device analyzer B1500A (SDA) with integrated PC. The setup uses four probes to minimize any parasitic resistance contributions from the wires and contacts. The setup is shown in Figure 2.36.

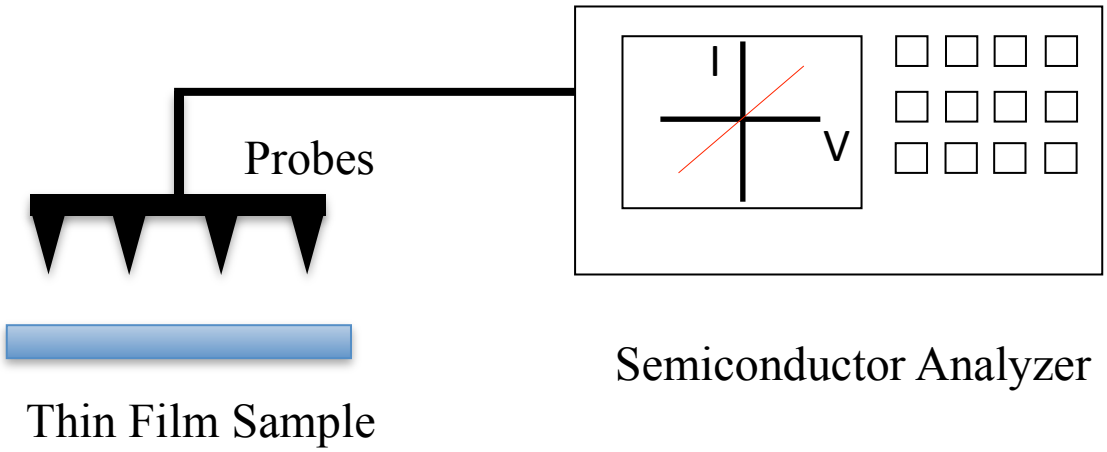


Figure 2.36. Setup for Current Voltage Measurement

To characterize the electrical properties of bulk and thin film semiconductor materials, the direct current electrical resistance measurement is commonly done using two point or four point probe contact method. [135]The two point probe method is usually used for testing bulk form and the resistivity can be obtained. When the two probes are in contact with the specimen, a voltage sources applied a voltage V across the sample, causing a current I to travel across the sample. Or, a current source could force current through the sample, while a voltmeter in parallel with the current source can measure the voltage induced across the sample. The amount of current I that flows through the sample is measured by the ammeter, which is connected in series with the sample and the voltage source. The resistance R of the sample is given by equation 2.60,

$$R = \frac{V}{I} \tag{2.60}$$

Then, the resistivity ρ of the sample can be calculated by equation 2.62,

$$\rho = \frac{RA}{l} \tag{2.62}$$

where V is the voltage, I is the current, R is the resistance, ρ is the resistivity, A is the cross-sectional area of the sample and l is the length of the sample.

The probe tips are usually mounted on the end of a controlling arm and each arm pivots on a probe station with a magnetic system that virtually eliminates the lateral motion of the probe tips as it contacts the sample surface. The probe tips are lowered onto the samples as gently as possible, because the pressure on the tip is quite high due to the small contact area. The probe tip material is relatively hard and consequently can leave "probe marks" sometimes on the specimen.

However, using the two point probe technique to measure resistivity is often not accurate, because it usually includes the parasitic resistance of the contact probes and the materials or in the measurement kit itself. These parasitic resistances can increase the actual value of the resistivity of the material. The modulation of the sample resistivity due to the applied current is also a potential issue. The four point probe measurement technique will eliminate many of these problems.

The four point probe setup consists of four equally spaced probe tips with finite radius. A high impedance current source is used to supply current to the outer two probes and a voltmeter measures the voltage across the inner two probes to determine the resistivity of the sample.[136] Figure 2.37 shows the setup of the four point probe method and the difference between the outer and inner probes.

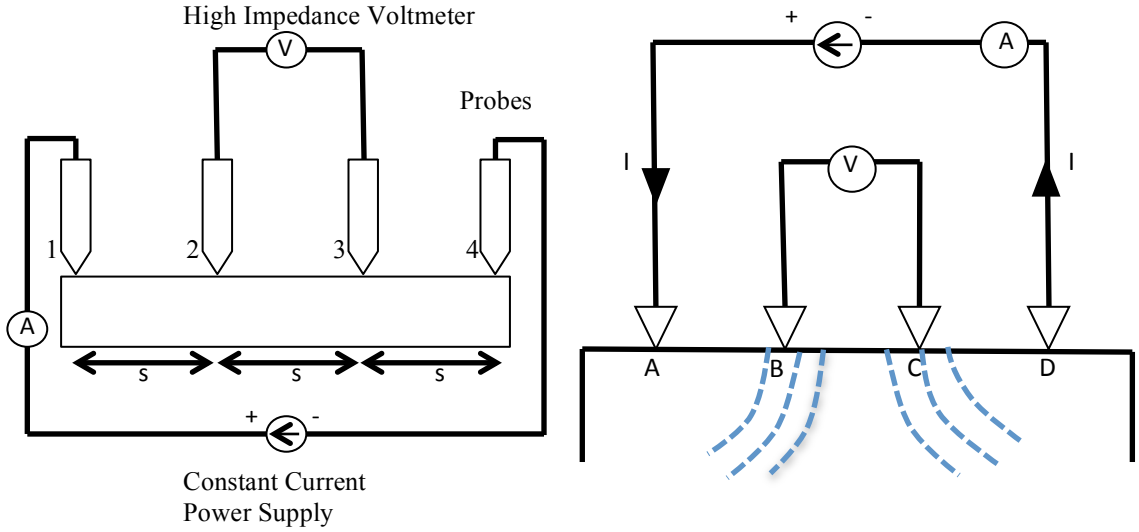


Figure 2.37. Left, Four point probe method of measuring resistivity of a specimen; Right, The electrical field and equipotential line distribution on the sample during the four point probe technique

The electric current travelling through the two outer probes create an electric field in the samples and they are shown by the solid blue lines in Figure 2.37. The two inner probes measures the potential difference between point B and C. The inner probes do not draw current due to the high impedance voltmeter, so the undesired voltage drop at point B and C is caused by contact resistance between the probe is eliminated from the measurement. Since the contact resistances can be sensitive to pressure and the sample surface condition, the errors relating to the two point probe technique can be quite large.

From these findings regarding the current voltage measurement technique, four point probe method is always used throughout the resonator characterization, because it proves to minimizes any possible errors from the characterization equipment. Thus, if the electrical results were undesired, then the errors can be easily deducted and solved from the fabrication route.

2.5.5.2 Capacitance Voltage Measurement

The capacitance voltage measurement at various frequencies is performed using an Agilent RF LCR meter 4287A with external DC bias supply and the semiconductor device analyzer mentioned before. Different measurement techniques are used for different frequency bands, this is shown in Figure 2.38.

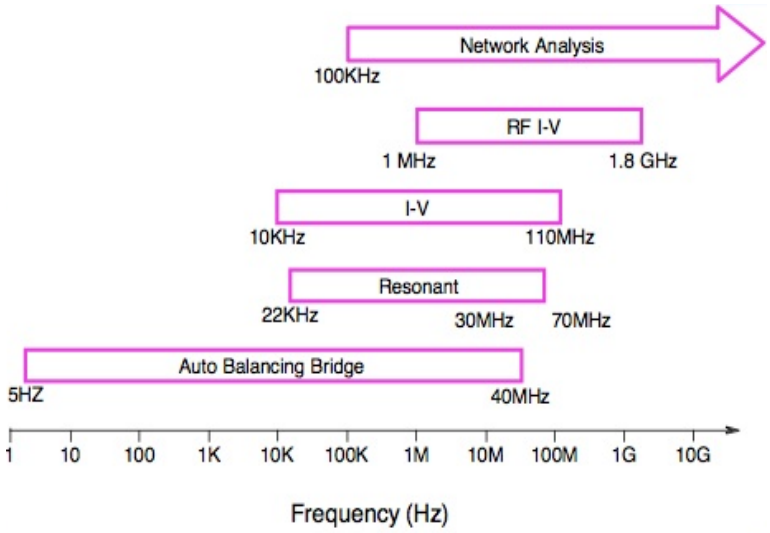


Figure 2.38. Different measurement techniques used for different frequency ranges[137]

For this bulk acoustic resonator structure, the high frequency RF I-V technique is used. The RF I-V method is based upon the same principle as the I-V method where the current is calculated using the voltage measurement across an accurately known low value resistor R. However, the RF I-V method employs an impedance matched measurement circuit(50Ω) and a precision coaxial test port for high frequency operation. There are two types of configuration for different impedance measurements and it is shown in Figure 2.39. The impedance of the device under test(DUT) is calculated from the equations illustrated in Figure 2.39. In practice, a low loss transformer is used in place of the low value resistor R and it can limit the low end of the applicable frequency range.

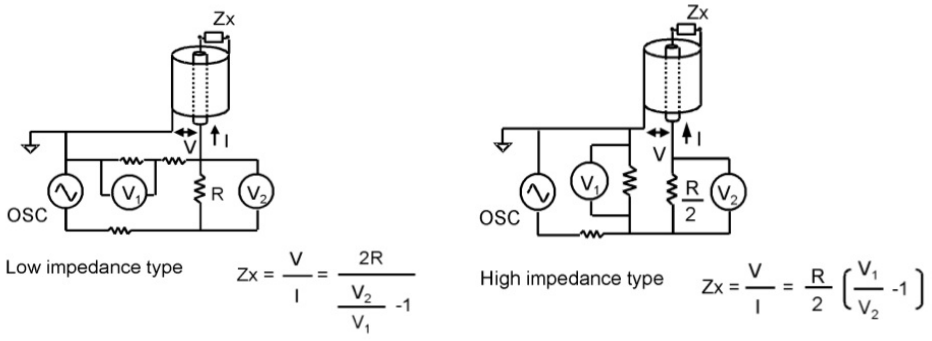


Figure 2.39. The different measurement configurations for different impedance samples[138]

In the RF I-V method, the signal source section generates a RF test signal applied to the test device and has a variable frequency range from 1MHz to 3GHz. A frequency generator is applied to meet the frequency accuracy, resolution and sweeping function requirements. The amplitude of the signal source output is adjusted for desired level through output attenuator. The test head section is equipped with a current detection transformer, V/I multiplexer and test port. The measurement circuit is matched to the 50Ω impedance to ensure the accuracy at high frequency operations. Since, the test current flows through the transformer in series with the DUT connected to the test port, it can be measured from the voltage across the transformer. The V channel signal E_{DUT} is the voltage across the DUT and I channel signal E_{TR} is the current flowing through the DUT. All measurements are made in reference to 50Ω without ranging operation due to the fixed impedance. The V/I input multiplexer selects the E_{DUT} and E_{TR} signals, so the two vector voltages are measured with identical vector ratio detector to avoid tracking errors. The measuring ratio of the two voltages originates from the impedance of the test device as the following relation,

$$Z_x = 50 \times \frac{E_{DUT}}{E_{TR}} \qquad (2.63)$$

The mixer circuit down converts the frequency of the E_{DUT} and E_{TR} signals to an frequency suitable for the AD converter's operating speed. In practice, double or triple conversion is used to obtain spurious free signals. Each vector voltage is converted into digital form by the AD converter and is digitally separated in to O° and 90° vector components. Figure 2.40 is a simplified diagram of the RF I-V equipment.

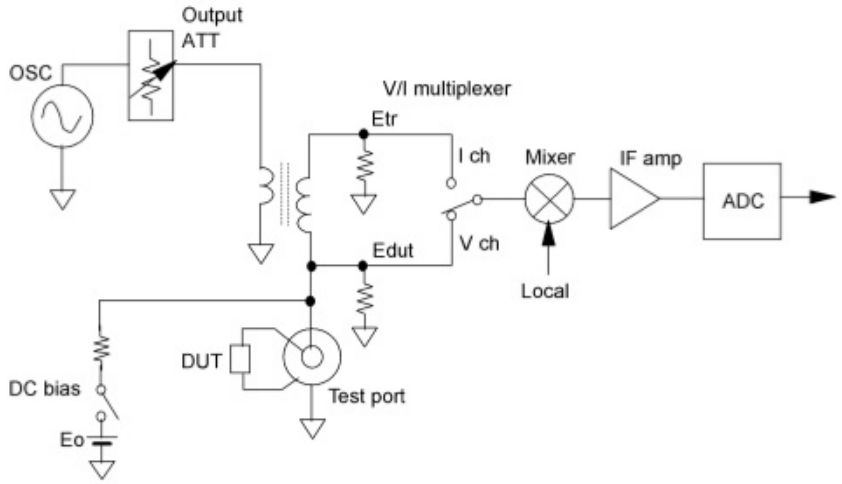


Figure 2.40. Simplified diagram of the RF I-V technique setup[138]

The capacitance measurement circuit generally consists of two types of circuit mode-parallel equivalent circuit and serial equivalent circuit mode. In case of small capacitance, it exhibits large reactance and high impedance, which can increases the effect of the parallel resistance R_p on the measurement much greatly than that of the serial resistance R_s, so the serial resistance can be neglected and the parallel circuit mode is used. For large capacitance, it has a small reactance and low impedance, which increases the effect of series resistance on the measurement much more than that of the parallel capacitance, thus R_p can be ignored and the serial circuit is applied. This is shown in Figure 2.41.

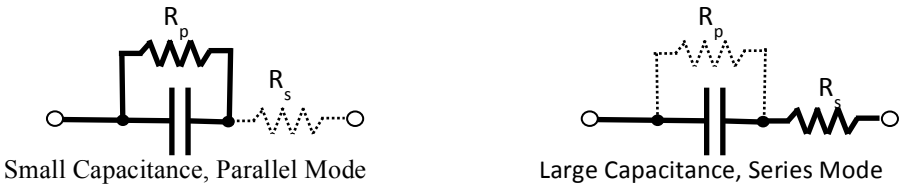


Figure 2.41. The two types of capacitance measurement circuit modes-Parallel and Series Equivalent Mode

Short-Open-Load calibration (50Ω) was done using the CS-5 calibration substrate. The resonator structures were contacted using ground-signal-ground microprobes for these measurements. The calibration and compensation steps were carried out, these steps are required to reduce the effects of error sources existing between the DUT and calibration plane of the instrument. The short open load compensation requires the measurement data of a standard device with a known impedance value and open/short measurement data. It will eliminate any complicated residuals, phase shift error and

maximize the correlation between the instruments. The setup is shown in Figure 2.42 and the circuit model is shown in Figure 2.43.

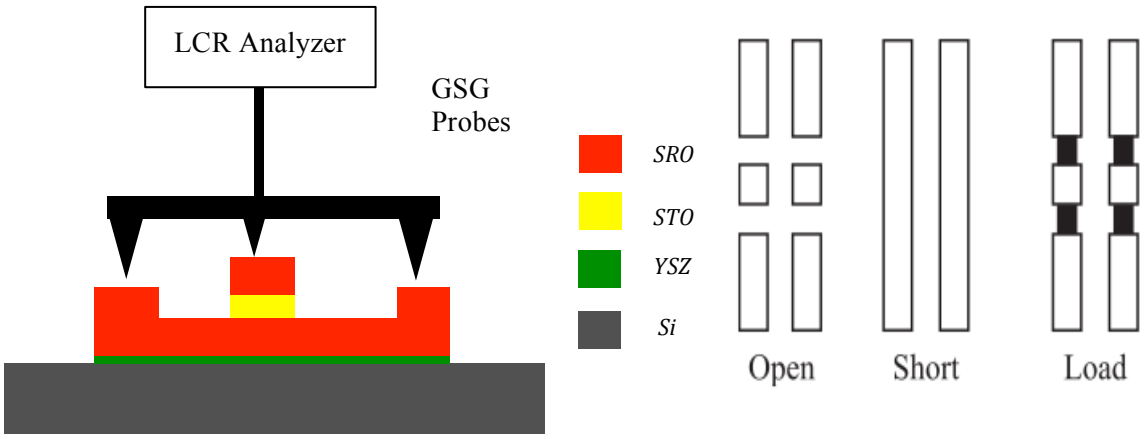


Figure 2.42. Setup for Capacitance Voltage Measurement and the calibration standards for measurements

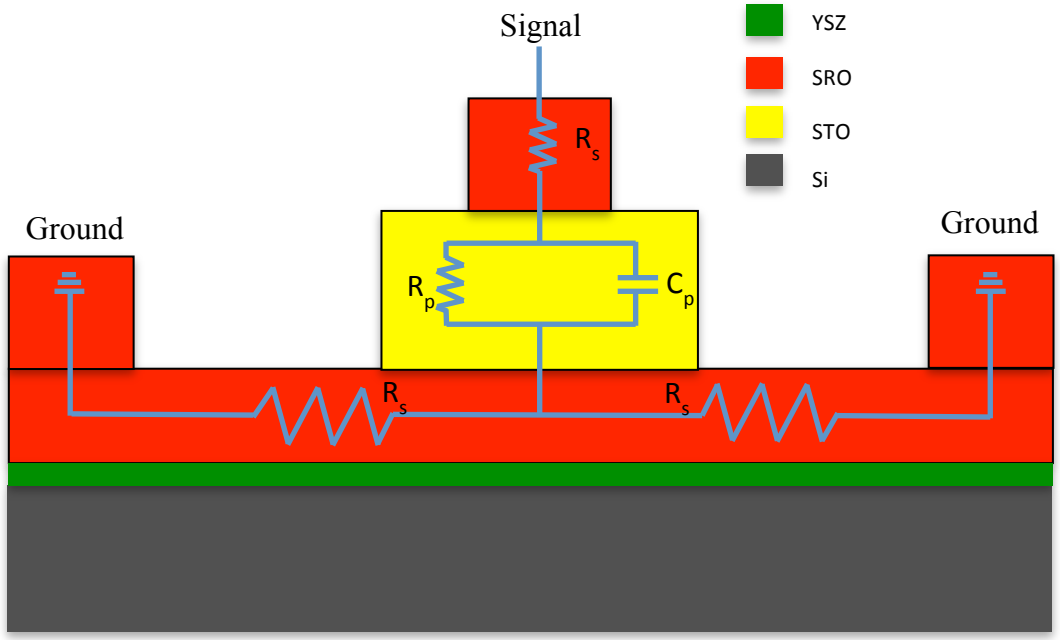


Figure 2.43. Circuit Model used to characterized the resonator performance

The residuals of a test device are defined as a four terminal network with A,B,C,D parameters, assuming that the impedance measurement value of a DUT with a true value Z_1 becomes Z_2 at the test terminals, the following equations can be derived.

$$Z_1 = \frac{(A \times V_2 + B \times I_2)}{(C \times V_2 + D \times I_2)} = \frac{(A \times Z_2 + B)}{(C \times Z_2 + D)} \qquad (2.64)$$

where $Z_1 = \frac{V_1}{I_1}$ and $Z_2 = \frac{V_2}{I_2}$.The open/short/load compensation is illustrated in Figure 2.44.

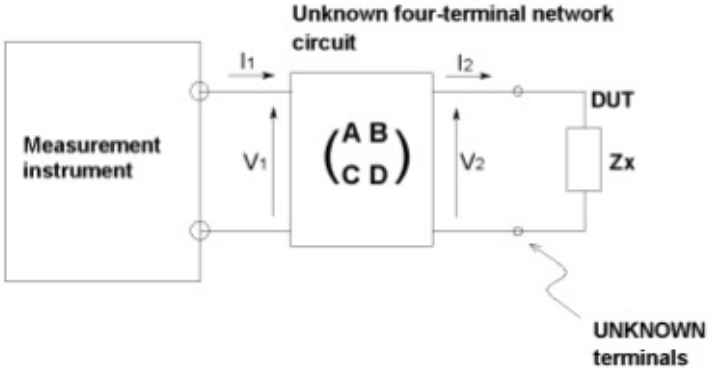


Figure 2.44. The Open/Short/Load Compensation for RF I-V measurement[138]

The dielectric constant, quality factor, loss tangent and tunability all can be extracted from the measurements using the relations,

$$\varepsilon_r = \frac{C \cdot d}{A \cdot \varepsilon_0} \tag{2.65}$$

$$Q = \frac{1}{tan\delta} \tag{2.66}$$

$$\text{Tunability(n)} = \frac{C(0) - C(V)}{C_0} \cdot 100\% \tag{2.67}$$

By using the capacitance voltage characterization technique, the resonator characteristics such as tunability, capacitance, quality factor, impedance and reactance can be measured at different frequencies and voltages. These characteristics must be characterized in order to determine the success of the resonator fabrication.

2.5.5.3 Resonance Measurement

Reflection measurements are the technique to determine the electrical response of the bulk acoustic wave resonator operating in the higher frequency range (GHz). One port S-parameter network analyzer 8722ES from Agilent with external DC bias supply was used to measure the microwave performance of the fabricated resonator. The probes used here was ground-signal-ground (GSG) GGB industries 150 μm microwave Picoprobes. The reflection coefficient is obtained by measuring the ratio of an incident signal to the reflected signal. A network analyzer is used to supply and measure the signals, while a directional coupler or bridge is used to detect the reflected signal.

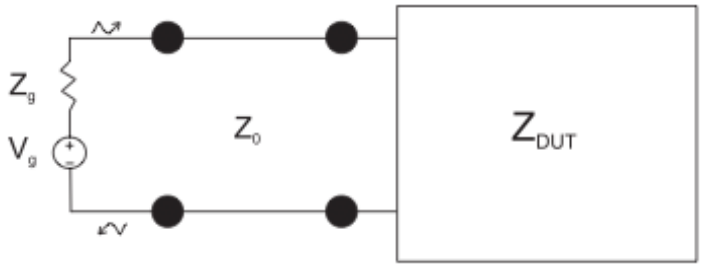


Figure 2.45. One port measurement setup for resonator device characterisation

The measured one port reflection measurement S_{11} is defined as

$$S_{11} = \Gamma = \frac{Z_{DUT} - Z_0}{Z_{DUT} + Z_0} \tag{2.68}$$

where the impedance Z_0=50Ω was used to calculate the input impedance Z of the resonator. In accordance with this equation, measured reflection coefficient ranges from -1 to 1 depending on the impedance, Z_{DUT}. The capacitance C and loss tangent tanδ were calculated from

$$Z = R + jX \tag{2.69}$$

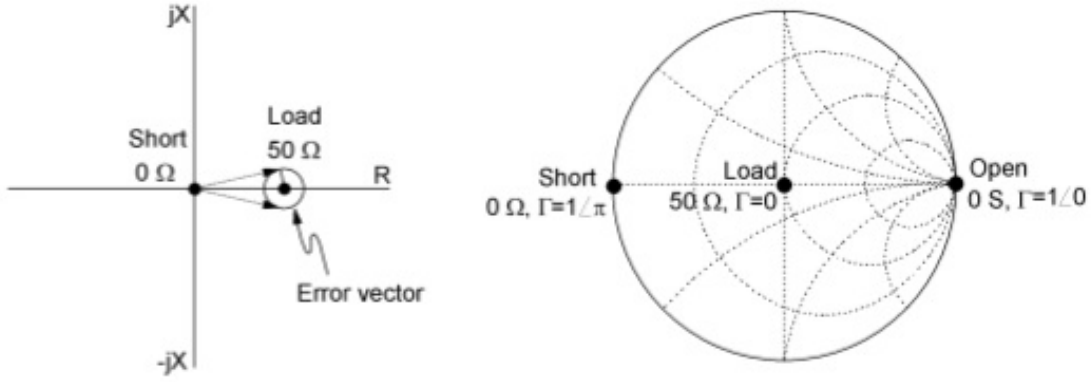
where R is the DC resistance,

$$\omega C = \frac{1}{\omega L - X} \tag{2.70}$$

where X is the reactance, ω is the angular frequency, L is the inductance and

$$\tan\delta = \frac{X}{R} \tag{2.71}$$

The multiplexed vector ratio measurement from the network analyzer avoid phase tracking error and calibration with a low loss capacitor will ensure a stable accurate measurement of the low dissipation factor, thus high Q factor. The open, short and load calibration minimizes instrument inaccuracies, so they must be connected to the test port and each of the terminations before actual measurement. The impedance values of these reference terminations are indicated on vector impedance plane and smith chart in Figure 2.46.



Note: Open impedance is infinite,
so it is not shown in the graph.

Figure 2.46. The calibration standard values for network analyzer in (left) Vector impedance plane and (right) Smith chart[138]

The network analyzer is an excellent solution for testing the fabricated resonator performance at high frequency ranges while maintaining fast speed and accuracy. Thus, the resonator device is tested both on the RF I-V method and network analyzer method to ensure the results are in coherence with each other.

2.6 Conclusion

The key concepts of ferroelectric thin films as well as the fabrication and characterisation techniques were reviewed in this chapter. The concept of using the paraelectric state ferroelectric thin films for TFBAR applications was introduced. The reviwed fabrication technmiques will be used to fabricate a ferroelectric based MEMS structure and the review characterisation will be used to measure the multiayer structure. In the next chapter, the experimental details and characterisation results of the SRO/STO/SRO/YSZ multilayer structure on Si substrate will be presented.

Chapter 3. Deposition and Characterisation of Thin Film Multilayer Structure

This chapter investigates the fabrication steps required to develop a successful tunable bulk acoustic wave resonator using PLD, magnetron sputtering, device patterning and substrate micromachining. PLD was used to deposit $SrTiO_3$, $SrRuO_3$ and YSZ thin films on high resistivity silicon substrate. Metal layers were deposited by magnetron sputtering for masks used in Si etching. The deposition parameters were studied and optimized to achieve epitaxial multilayer structures for the design of tunable bulk acoustic wave resonator.

3.1 Processing Overview

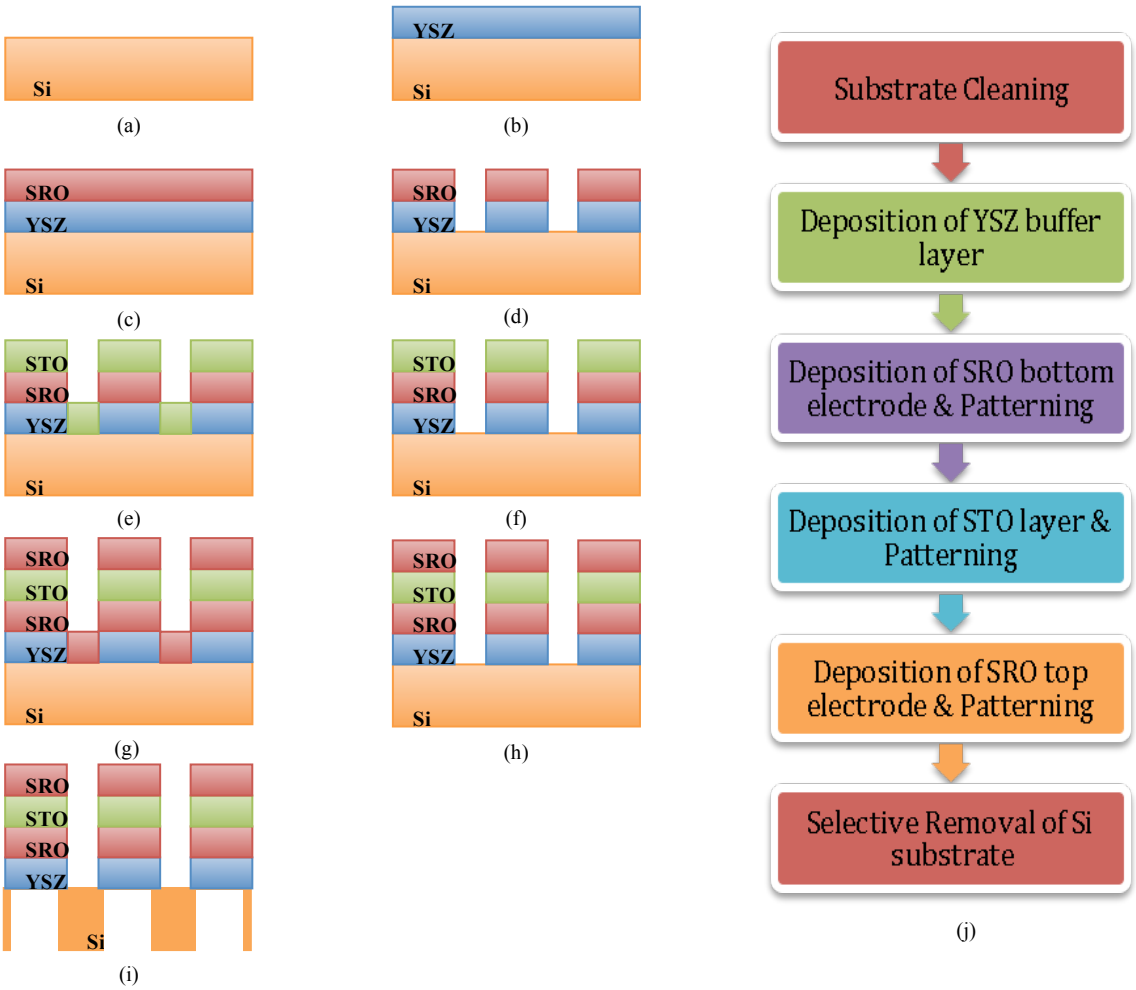


Figure 3.1. The fabrication process of the bulk acoustic wave resonator: (a) substrate pre-treatment, (b) YSZ buffer layer deposition by PLD, (c)SRO bottom electrode deposition by PLD, (d)Patterning of SRO bottom electrode using photolithography and ion beam milling, (e) STO ferroelectric layer deposition by PLD, (f) Patterning of

the STO ferroelectric layer by photolithography and ion beam milling, (g) SRO top electrode deposition by PLD, (h)Patterning of SRO top electrode by photolithography and ion beam milling and (i) Deep etching of the Si substrate from the backside of wafer by reactive ion etching resonator and (j) flow chart of the processing route

The multilayer thin film structure was fabricated *in-situ* on high resistive silicon substrate using PLD and employs a free standing MEMS systems design. The fabrication steps are drawn in the diagram and flowchart shown in Figure 3.1.

The pulsed laser deposition system configuration used for growing this resonator structure is summarized below:

- KrF Excimer Laser(Lambda Physik): Wavelength-248nm
- Laser Fluence: 1.2 J/cm^2
- Repetition Rate: 8Hz
- Substrate to Target Distance: 55mm
- Substrate Temperature: 700-850℃
- Oxygen Partial Pressure: 75-200mTorr

To ensure low microwave losses, the substrate was 300μm thick high resistive silicon (HRS) (ρ>10 kΩcm) with (100) orientation (sourced from PI-Kem). The multilayer structure were grown epitaxially on the single crystal Si substrate using PLD, which will improve the electrical characteristics of the thin films compard to the films with preferred orientations. The growth conditions for the multilayer structure are summarized in Table 3.1.

Materials	**Substrate Temperature/°C**	**Oxygen Partial Pressure/ mTorr**
YSZ	800	10^{-2}
$SrRuO_3$	700	75
$SrTiO_3$	850	150

Table 3.1 Growth Conditions for each layer within the multilayer structure for the bulk acoustic wave resonator

The fabrication of the resonator structure on the silicon substrate begins with the deposition of the YSZ buffer layer on top of the wafer, then the SRO bottom electrode was deposited in-situ on top of YSZ. The bottom electrode and the buffer layer were both patterned using photolithography followed by ion beam milling. Next, a ferroelectric layer of STO was also deposited on top of the bottom electrode using

PLD. Then the active layer pattern was aligned to the pattern of the bottom electrode by photolithography and partially removed using ion beam milling. Then the SRO top electrode was deposited on top of the active layer using PLD and it was patterned according to techniques already described. In the last step, the Si substrate was etched through using an alternative etching process involving reactive ion etching using a combination of CF_4+Ar+O_2 gases and metal masking. The resonator device was freestanding on the substrate at this point.

3.2 Deposition of 8 mol% Yttria Stablized Zirconia(YSZ) buffer layer by Pulsed Laser Deposition

8mol% Yttria Stabilized Zirconia (YSZ) was chosen as buffer layer material for the epitaxial growth of Strontium Ruthenate(SRO) film on the silicon substrate, because it makes up a barrier between the Si substrate and the SRO film to minimize the chemical interaction by the RuO_2 and Silicon. The strong chemical interaction between the $SrRuO_3$ thin film on the silicon substrate can result in formation of randomly oriented polycrystalline $SrRuO_3$ film, which is preferentially formed due to the unstable contact of $SrRuO_3$ with Si from the Ru-Si-O ternary system as it has no stable tie line between the RuO_2 and Si.[139] To ensure the oxide electrode was epitaxially grown on the silicon substrate, the buffer layer must first become epitaxially grown on the substrate.

Yttria-stabilized zirconia exhibits high chemical stability, high heat resistance, ionic conductivity at high temperature and inertness with silicon, which it is advantageous when compared with other buffer materials. Pure zirconia(ZrO_2) exists in the monoclinic form at room temperature and the addition of cubic stabilizers such as Y_2O_3 allows the transformation to stable cubic fluoride structure. YSZ has a dielectric constant of 27 at 10GHz and a 5eV bandgap. The lattice parameter of YSZ is 5.16Å and the lattice parameter of silicon is 5.43Å, warranting a very small(5%) lattice parameter mismatch.

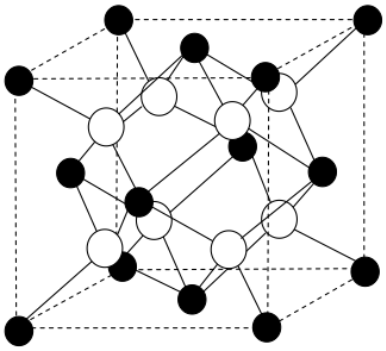


Figure 3.2. Crystal structure of Yttria Stabilized Zirconia

In this work, a YSZ buffer layer was deposited as the first layer on the silicon substrate to facilitate the further epitaxial growth of $SrRuO_3$ thin film. YSZ can be deposited on the silicon substrate by many methods, but the pulsed laser deposition process is considered the most suitable technique due to its versatility and direct stoichiometric transfer from the target composition to the thin film.[140] Moreover, multilayer films can be deposited using a multi-target PLD system in a single process. The quality of YSZ thin film depends on the deposition conditions such as substrate temperature and oxygen partial pressure. They must be optimized to fabricate high quality epitaxial multilayer films.

Several studies[141-143] have suggested that a thin SiO_2 layer on top of the silicon surface favours the high quality growth of epitaxial YSZ films. Therefore the first task of this part of the study was to evaluate the effect of the Si native oxide layer on the YSZ film growth.

To investigate whether the native oxide of the silicon substrate affects on the epitaxial growth of YSZ buffer layer on the silicon substrate, two different samples were compared. One sample was untreated and it had native oxide grown on top of the silicon substrate. The native oxide of the other sample was etched using buffered HF mixture consisting of 40% Ammonium Fluoride(NH_3F), 49% Hydrofluoric acid(HF) and DI water.

The removal of the silicon dioxide by buffered oxide etch solution was based on the overall reaction,

$$SiO_{2\,(s)} + 4HF_{(l)} \rightarrow SiF_{4\,(aq)} + 2H_2O_{(l)} \qquad (3.1)$$

Both silicon substrates with and without native oxide layer were further processes using a PLD.

The KrF excimer laser($\lambda = 248\text{nm}$)operating at a repetition rate of 8Hz with an energy density of 1.2J/cm^2 was used to deposit the YSZ buffer layer. The base pressure in the chamber was 1×10^{-6} Torr before increasing the substrate temperature. Epitaxial YSZ thin film was grown on both types of substrate at a substrate temperature of 800℃ and no addition of oxygen gas into the chamber. The thickness of the YSZ buffer layer was 10nm.

The crystallographic orientation of the films were characterized and compared by XRD with Cu K_α radiation shown in Figure 3.3.

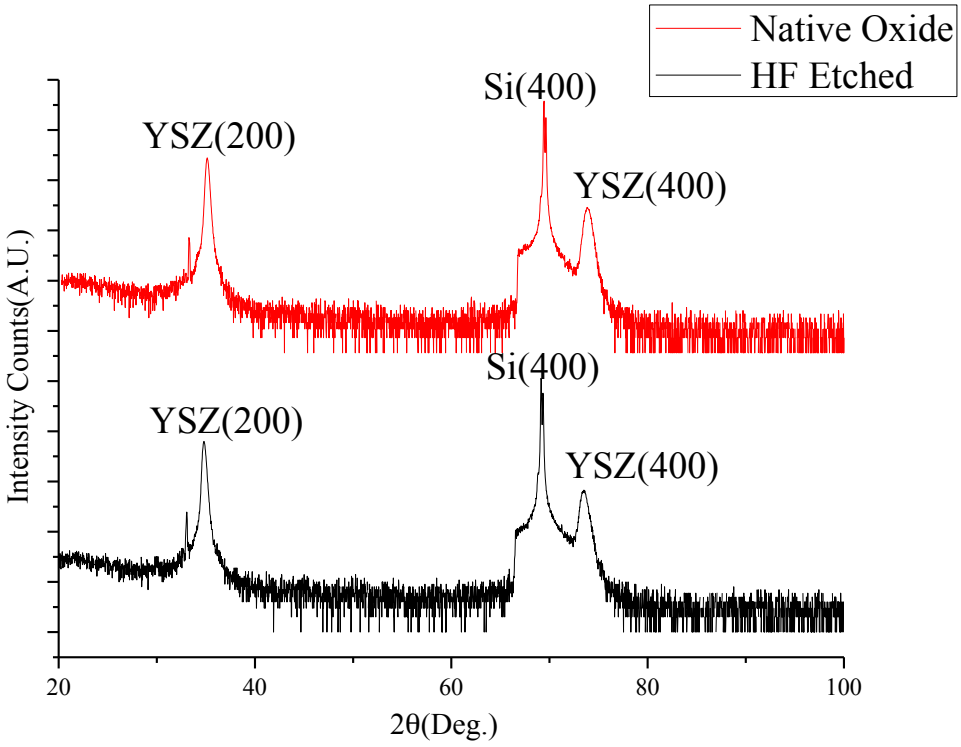


Figure 3.3. X-ray $\theta - 2\theta$ diffraction pattern of YSZ on Si substrate with native oxide and Si substrate with HF etching treatment

The X-ray diffraction results showed that YSZ buffer layer can be epitaxially grown on top of both HF treated and untreated silicon substrate. The native oxide layer of the silicon substrate have shown no effect on the epitaxial growth of YSZ buffer layer, thus untreated silicon substrate was used throughout the fabrication of the acoustic wave resonator device.

3.3.1 Deposition of Strontium Ruthenate ($SrRuO_3$) Electrodes by Pulsed Laser Deposition

The choice of electrodes sandwiching the active ferroelectric oxide layer was important in order to obtain good quality deposited films for desired resonator

characteristics and mechanical properties The oxide electrodes had smaller lattice mismatch with the active layer compared with the metal electrodes, thus it was easier for the oxide electrodes to achieve high quality epitaxial grown ferroelectric films. The thickness of the electrodes would affect the Q-factor of the resonator[144],the effective resonator coupling coefficient and the tunability. Thick electrodes would increase the mechanical losses in the acoustic path of the active layer and the proportion of non-tunable electrode material within the resonator volume. In order to maximize the Q-factor and tunability of active ferroelectric layer, a low resistivity and structurally compatible material was preferred. The conductive oxide electrodes such as $SrRuO_3$ were commonly used for fabricating multilayer ferroelectric oxide resonator structures. Metal electrodes such as Pt were also reported to be the widely accepted candidates for growth of high quality ferroelectric oxide thin films, because they are inert under high temperature oxidizing conditions and exhibit low leakage currents. Usually, Ti is deposited as an intermediate layer to improve adhesion between Pt and the SiO_2 layer. However, the formation of hillocks in the Pt electrodes due to stress relief will cause electrical shorting. The fiber textured morphology of Pt electrodes will also not be suitable for growing epitaxial films of perovskite films, where the perovskite films deposited on such $Pt/Ti/SiO_2/Si$ substrates were usually polycrystalline or textured.

Strontium Ruthenate was electrically conductive and structurally matched with most perovskite oxides. $SrRuO_3$ crystallizes in an orthorhombic perovskite structure and can be regarded as pseudo cubic structure owing to the distortion of the RuO_6 octahedra at room temperature. This crystal structure was shown in Figure 3.4. Thus, it was used mainly as electrodes of many ferroelectric oxide devices. Many groups have reported the epitaxial rectangle on cube relation between the SRO[110] ‖ YSZ[100] ‖ Si[100], where the (110) SRO plane is based on the pseudocubic structure of the SRO lattice. The schematic drawing of the epitaxial relation of SRO on YSZ was shown in Figure 3.5.

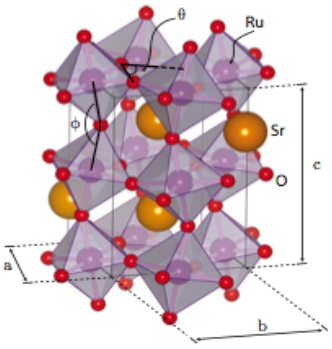


Figure 3.4. The orthorhombic crystal structure of $SrRuO_3$ with the lattice parameters of a=5.57,b=5.54 and c=7.85Å.[145]

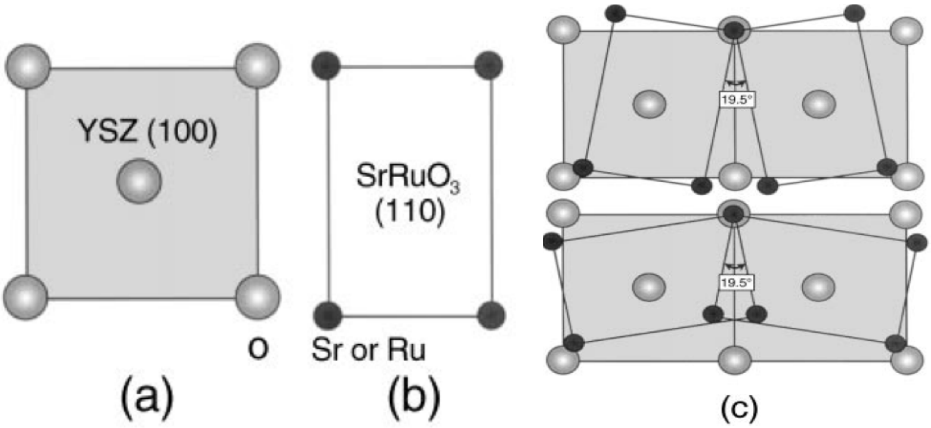


Figure 3.5. Schematic drawing of the rectangle on cube epitaxial relation of $SrRuO_3$ on YSZ: a) YSZ(100) plane, b)$SrRuO_3$(110) plane and c)Possible variants of the epitaxial relationship [146]

In the pulsed laser deposition technique, the substrate temperature and oxygen pressure were the main parameters controlling the growth of the electrodes. The interfaces between the substrate/electrode/dielectric can all cause problems towards non-stoichiometric growth and single crystal properties. Values of physical parameters of the used substrates and thin films such as metal oxide electrodes and ferroelectric materials are presented in table 3.2.

Material	**Structure**	**Lattice Parameters(Å)**	**Linear Thermal Expansion Coefficient ($10^{-6}/K$)**
Si	Cubic	a=5.43	4.4
$SrRuO_3$	Orthorhombic/ Pseudo-cubic	a=5.57 b=5.54 c=7.85 a=3.92(pseudo-cubic)	1.5(<160K) 4.5(>160K)
YSZ	Cubic	a=5.16	10
$SrTiO_3$	Cubic	a=3.91	10.08

Table 3.2. Physical properties of the materials used in the pulsed laser deposition

In this study, Strontium Ruthenate (100nm) was first deposited on SiO_2/Si substrate at a substrate temperature of 700℃ and oxygen partial pressure of 75mTorr. After the deposition of the $SrRuO_3$ films, it was post-annealed in oxygen environment (O_2:500 Torr) at 700℃ for 20 minutes to achieve high crystallinity single phase thin films. The SRO film is polycrystalline with random orientation (see Figure 3.6). This was due to the chemical interaction of silicon and the RuO_2 mention in the earlier chapter. By applying a 10nm YSZ buffer layer on the SiO_2/Si substrate prior to SRO deposition, it has allowed the epitaxial growth of SRO in an orientation of (110). Figure 3.7 shows a SRO[110]∥YSZ[100]∥Si[100] relation on the XRD graph.

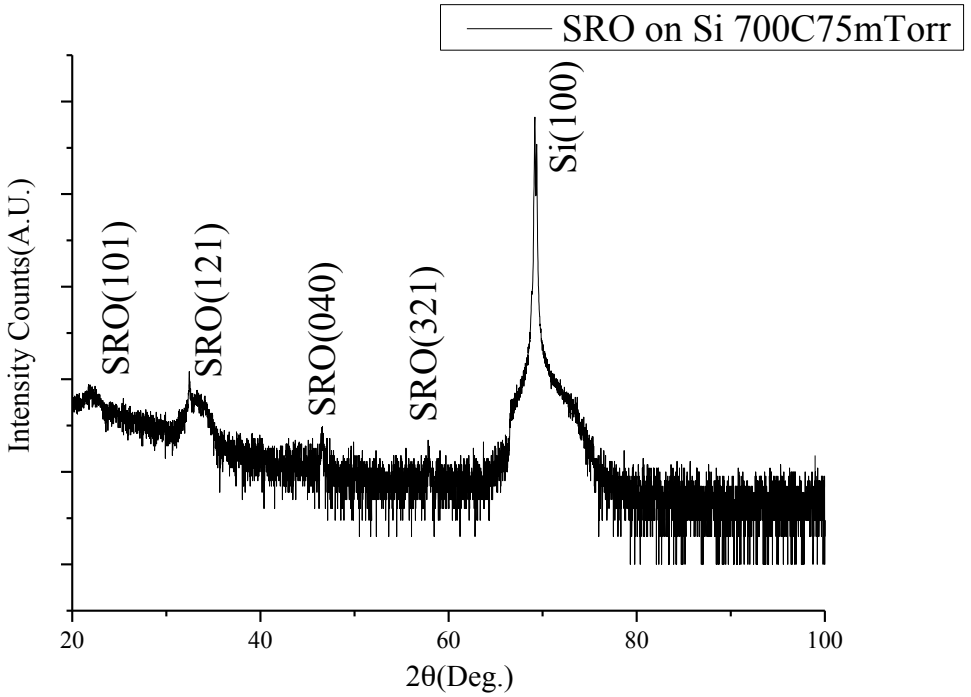


Figure 3.6. X-ray $\theta - 2\theta$ diffraction pattern of SRO on Si substrate

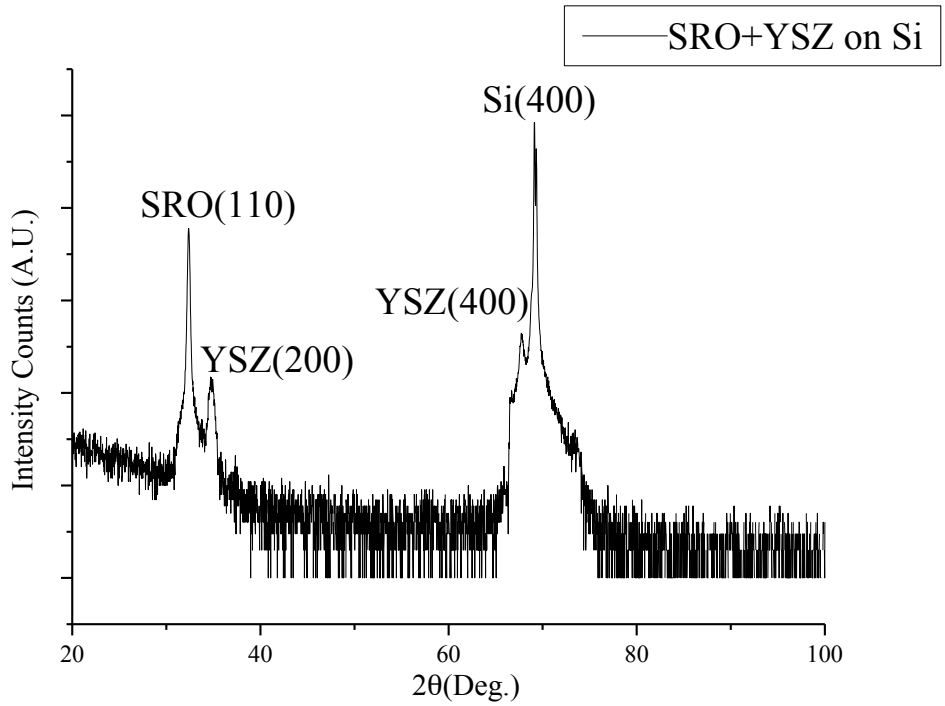


Figure 3.7. *X-ray $\theta - 2\theta$ diffraction pattern of SRO on YSZ buffered Si substrate*

From these X-ray diffraction results, we note the importance of depositing a YSZ buffer layer prior to the growth of the SRO electrode on the silicon substrate. The

epitaxial growth of SRO electrode and further multilayer depositions on the silicon substrate was only possible with the presence of the YSZ buffer layer in between. Thus, the growth of the multilayer resonator structure can be controlled and tailored using different temperatures, oxygen partial pressures and buffer layers.

3.3.2 Electrical properties of the Strontium Ruthenate thin films

The four-probe current voltage measurement technique was used to compare the conductivity of the bottom $SrRuO_3$ electrodes deposited directly on the silicon substrates and on the YSZ buffered silicon substrates. The result is shown in Figure 3.8.

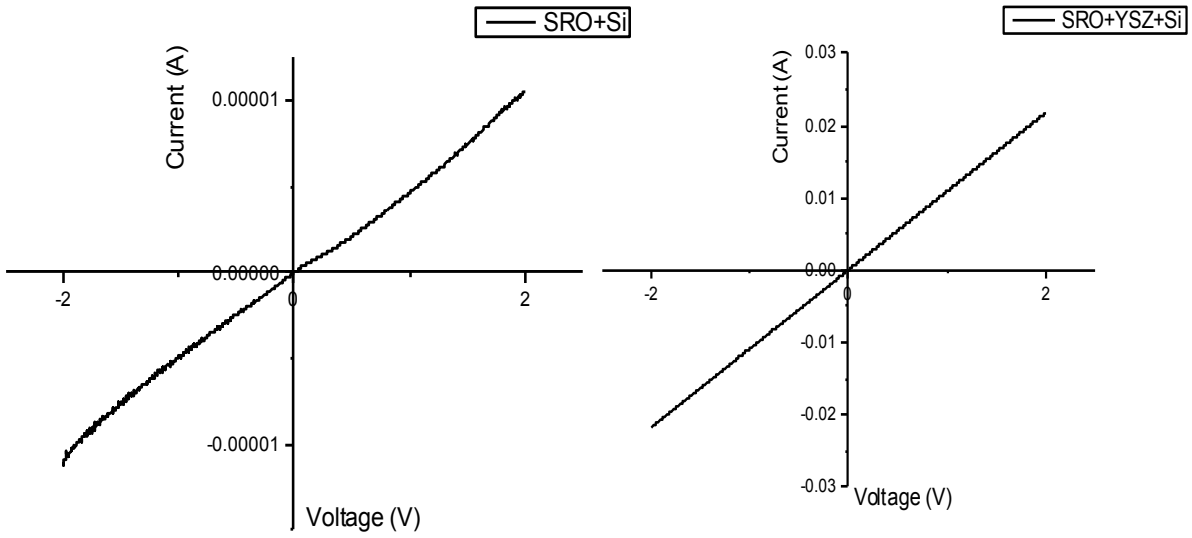


Figure 3.8. The current-voltage curve for the bottom electrode deposited directly on silicon and deposited on YSZ buffered silicon substrate.

The results showed that the epitaxially grown bottom $SrRuO_3$ electrodes on the YSZ buffered Si substrate has better electrical conductivity than the polycrystalline grown $SrRuO_3$ electrodes. This was expected because of the absence of the defects associated with grain boundaries in the epitaxial single crystal materials can improve their electrical properties greatly compared its polycrystalline form. Thus, the growth conditions for depositing epitaxial SRO electrodes were used throughout the fabrication of this novel bulk acoustic wave resonator.

3.4.1 Deposition of Strontium Titanate ($SrTiO_3$) Active Layer by Pulsed Laser Deposition

The quality of the thin film deposited by PLD strongly depends on the deposition parameters such as substrate temperature and oxygen partial pressure. The substrate

temperature can affect the mobility of adatoms on the surface, and thus determines the crystalline quality of the thin films. By increasing the substrate temperature from low to high, the crystalline phase of the thin films usually start from amorphous to polycrystalline and then to highly orientated films. Many studies[147] [148-150]have shown that the epitaxial grown form of STO active layer was known to exhibit superior microwave properties such as piezoelectric coefficients, tunability, electric field dependent dielectric constant and low loss tangent compared to its polycrystalline form, thus the resonator characteristics would be greatly improved.

The STO films were first deposited directly on SRO/Si substrates, so the deposition parameters of substrate temperature and oxygen partial pressure were varied to determine the conditions for growing crystalline films of desired orientation. 100nm thick $SrTiO_3$ thin films were deposited at various temperatures from 800-1000℃ on $SrRuO_3$(grown at 750℃ and oxygen partial pressure 75mTorr)/Si substrate with all other deposition parameters kept constant. The oxygen partial pressure was 75mTorr. The comparison of $SrTiO_3$ films at different substrate temperatures is shown in Figure 3.9 and the growth at 850℃ was the only condition that resulted STO growth in the (100) orientation. Next, only the oxygen partial pressure was varied from 50-100 mTorr at constant substrate temperature 850℃ and the comparison of $SrTiO_3$ films at different partial pressures is shown in Figure 3.10.

However, the results displayed polycrystalline STO film of preferred orienations, which exhibit poor electrical characteristics compared to the epitaxial grown single crystal STO film. 10nm thin YSZ buffer layer was deposited on the substrate prior to the $SrTiO_3/SrRuO_3$ multilayer deposition and this solved the problem. Epitaxial $SrTiO_3$ thin films of (110) orientation was grown on top of the $SrRuO_3$ electrodes of (110) orientation with YSZ buffer Si substrate at 850℃ and 150mTorr O_2 partial pressure, which is shown in the XRD scan graph of Figure 3.11.

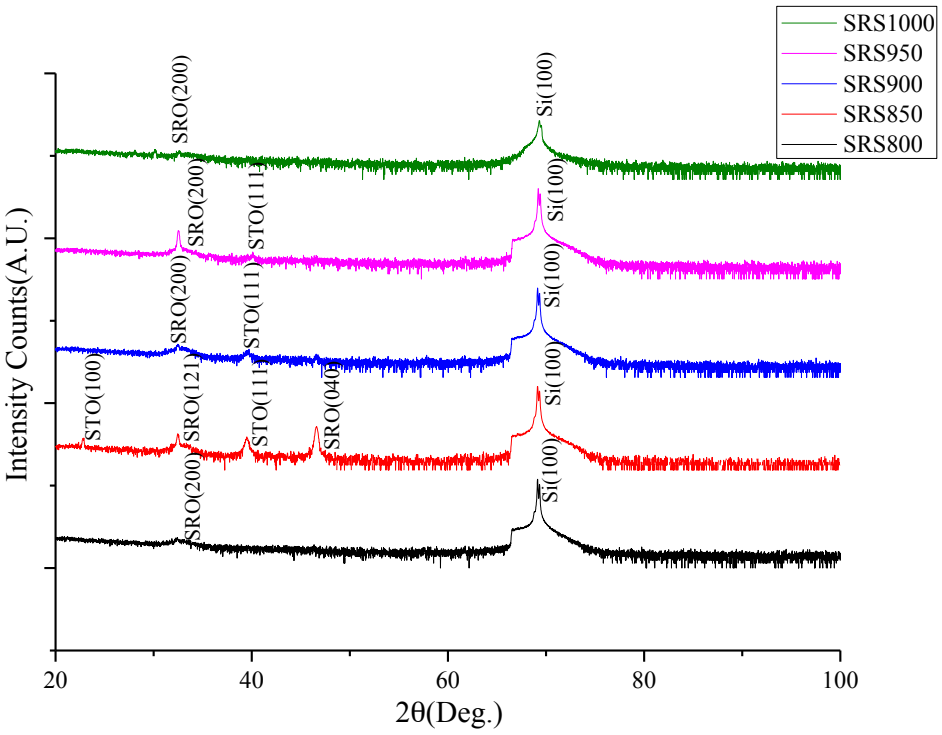


Figure 3.9. X-ray $\theta - 2\theta$ diffraction pattern of STO thin films grown on SRO electrodes on Si substrate at different substrate temperature (800-1000°C) and at constant oxygen partial pressure 75mTorr

From the Figure 3.9, the effect of substrate temperature during the growth of Strontium Titanate films had great influence on the orientation and the film crystalinity. The STO (111) peak only appears when the substrate temperature has reached above 850℃, which suggests it can only crystallize when above this substrate temperature. The intensity of the STO(111) peak decreases when the temperature has increased above 850℃ and this shows that 850℃ was the only suitable substrate temperature for growing high quality $SrTiO_3$ thin films on $SrRuO_3$ electrodes on Si substrate.

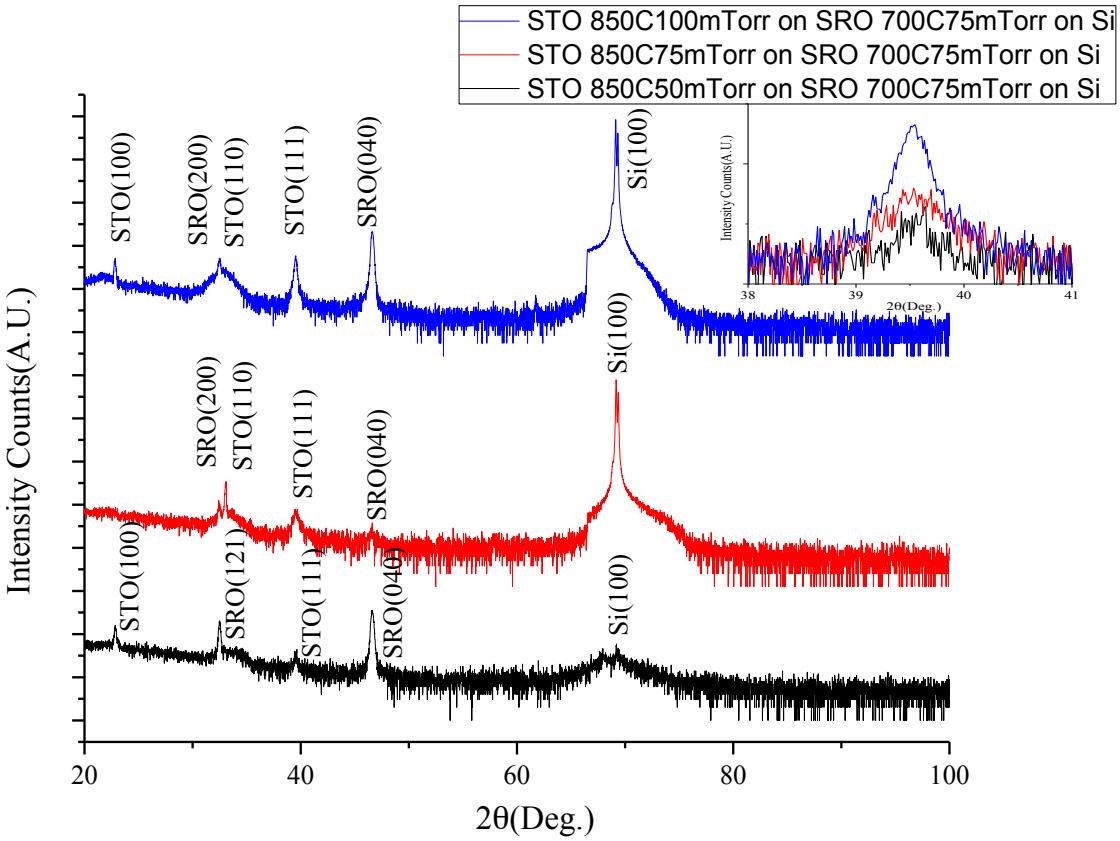


Figure 3.10. X-ray $\theta - 2\theta$ diffraction pattern of STO thin films grown at 850°C on SRO/Si at different oxygen partial pressures from 50-100mTorr and (inset) an enlarged comparsion XRD graph at STO(111)peak.

From the Figure 3.10, the effect of oxygen pressure during the growth of Strontium Titanate films is observed to exert a great influence on the orientation and the film crystallinity. As the oxygen pressure was increased from 50mTorr to 100mTorr, the (110) STO peak have begun to appear and the intensity of the (111) STO peak have increased. This was due to the oxygen relaxation of the $SrTiO_3$ film and the decrease in the oxygen defects in the film.

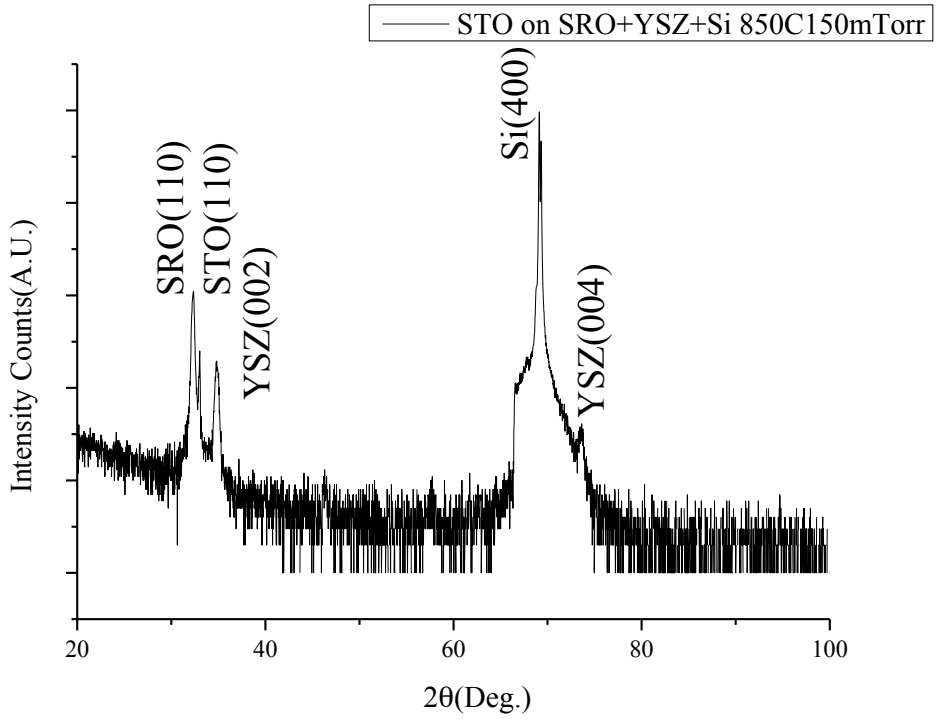


Figure 3.11. X-ray $\theta - 2\theta$ diffraction pattern of STO thin films grown on SRO electrodes on YSZ buffered Si substrate at 850℃ *and 150mTorr O_2 partial pressure.*

Figure 3.11 shows the epitaxial growth of (110) orientated STO films deposited on top of (110) oriented SRO films with YSZ buffered Si substrate using substrate temperature of 850 and oxygen partial pressure 150mTorr. These growth conditions were used throughout the fabrication of the multilayer structure for TFBAR application.

3.4.2 Tunability vs. Frequency Measurement Results

The variation of capacitance with externally applied voltage was measured for the fabricated resonator with the following configuration 300nm SRO/500nm STO/300nm SRO/10nm YSZ on Si substrate and active area of 50×50μm. The bias voltage was applied from -2V to 2V and the capacitance value was measured for every 0.5V interval at frequencies 10MHz to 1GHz. The tunability of the device at various frequencies during this capacitance measurement was shown together with the CV curve in Figure 3.12.

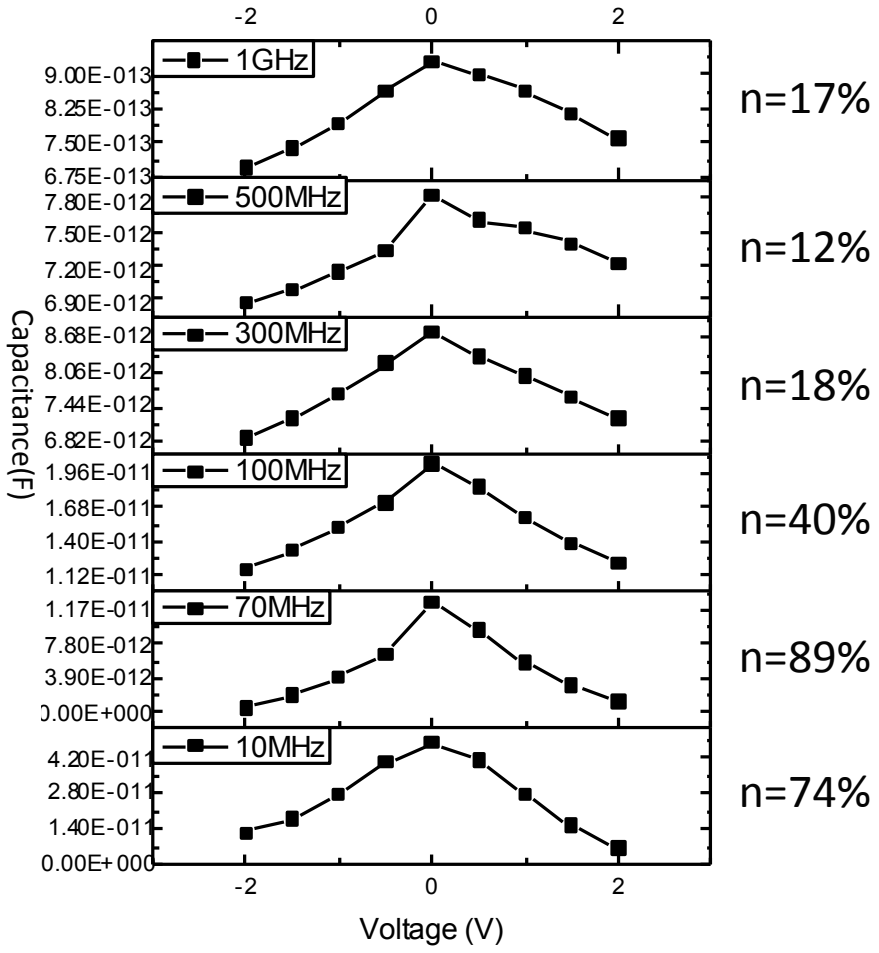


Figure 3.12. The Capacitance-voltage behaviour of the resonator device at various frequencies with applied voltage from -2V to 2V

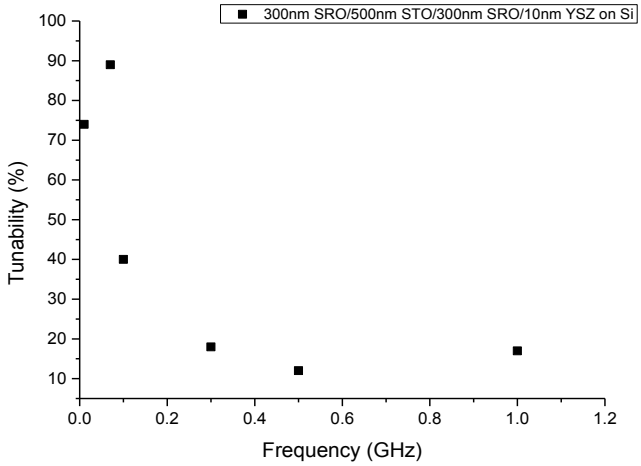


Figure 3.13. Frequency vs Tunability of the 300nm SRO/500nm STO/300nm SRO/10nm YSZ on Si multilayer structure

As seen in the Figure 3.12, the capacitance value decreased monotonically as the bias field was increased and this result was also independent of the polarity of the bias field. This demonstrated the possibility of tunable characteristic of the resonator to vary the dielectric constant of the high permittivity STO thin film materials with respect to the application of a DC electric field. The decrease in the tunability value as the frequency increases shown in Figure 3.13, because the contact resistance and finite sheet resistance of the electrodes and the quality of thmaterial deposited and the electrode-ferroelectric interface. From the results, the multilayer structure displays reasonable tunable behaviour and can be used for the resonator applications.

3.5 Metal Layer Deposition

Metal thin films were used as masking layers for the silicon substrate micromachining process, which is described in detail at the next subchapter. They were deposited using the DC and RF magnetron sputtering technique. The system used for this deposition process was the Mantis QPrep Deposition System with *in-situ* rate and thickness QCM (Quartz Crystal Microbalance) monitor. The metal films were produced in vacuum using this technique has advantages such as multilayer growth, good adhesion, smaller grain size, increased cleanness and uniform thickness compared to other fabrication techniques. However, the source material was limited to sheet form only and the deposition rate was lower than others. The deposition conditions for each metal mask material are summarized in Table 3.3

Material	**Argon Flow(Sccm)**	**DC/RF**	**Current/Power(mA/W)**	**Deposition Rate(Å/s)**
Au	120	DC	28mA	0.62
Ti	200	DC	1000mA	0.73
Nb	200	DC	100mA	0.25
Cr	100	RF	120W	0.62
Ag	200	DC	40mA	0.37
Al	80	RF	180W	0.61

Table 3.3. The sputtering conditions for different metal mask materials

This table shows that the growth of metal thin films can be controlled and varied with respect to the requirement of the silicon substrate micromachining process. This was very important when growing multilayer metal thin films and the substrate etching process is dependent on the metal mask layers.

3.6 Conclusions

In this chapter describes the deposition process of the multilayer SRO/STO/SRO thin film structure on YSZ buffered HRS substrates using PLD. The multilayer structures were epitaxially grown on the YSZ buffered HRS substrates and this buffer layer is key to achieving this epitaxy. The electrical conductivity measurements of the SRO bottom electrode with and without YSZ buffer layer were compared and the latter setup displayed poorer results. The tunability of the STO active layer (area of 50×50μm) was measured at frequency 10MHz to 1GHz and its value decreased with increasing frequency. These electrical measurements were performed without the silicon substrate cavity etching, thus these results are only to ensure that the tunable characteristic of the active layer in the multilayer structure could be further implemented in TFBAR applications.

Chapter 4. Deep reactive ion etching of Silicon

This chapter investigates the etching steps to develop a successful method to create a free standing tunable bulk acoustic wave resonator on the silicon substrate. An alternative silicon deep etching process using metal mask and reactive plasma of CF_4+Ar+O_2 gases was developed to etch through 500 μm thick Si substrate and protect the device side at the same time. This etching technique is cost effective and alternative to the Bosch and Cryogenic DRIE techniques in terms of fast Si etch rate.

4.1 Optimisation of the Si reactive ion etching process

In order to accurately understand the etching behaviour of silicon under reactive ion etching with variation of process parameters such as pressure, RF bias and gas additions. 500 microns thick of single crystal Silicon wafer were patterned with photoresist and etched under different combinations of etchant gas for 15 minutes-Tetraflouromethane(CF_4)+Argon and the mixture was mixed in different ratios of 1:3, 2:2 and 3:1. The etching of silicon was carried out at total CF_4 gas flow of 40sccm,beacuse CF_4 is mainly responsible to creating the etchant of the silicon and at higher pressures as more reactive etchant would require higher gas flows, thus achieving higher silicon etch rates. The etch depth profile are measured by using contact profilometry(Dektak) and the etch rates calculated by dividing the etch depth by 15 minutes. The etch depth profile is measured three times and averaged value is plotted in the following graphs with error bars. In some of the graphs, the error bars are very small and are often covered by the size of the point.

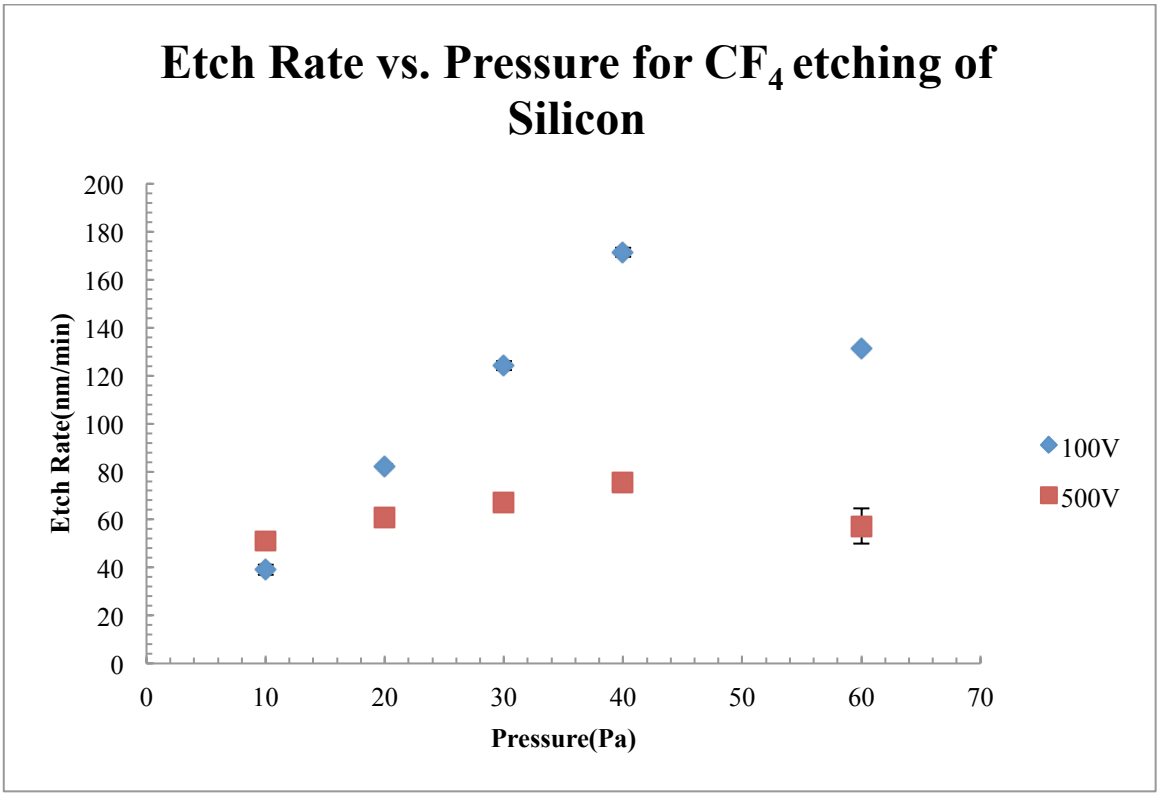


Figure 4.1. Etch Rates of Silicon vs. Pressure under CF_4 Plasma

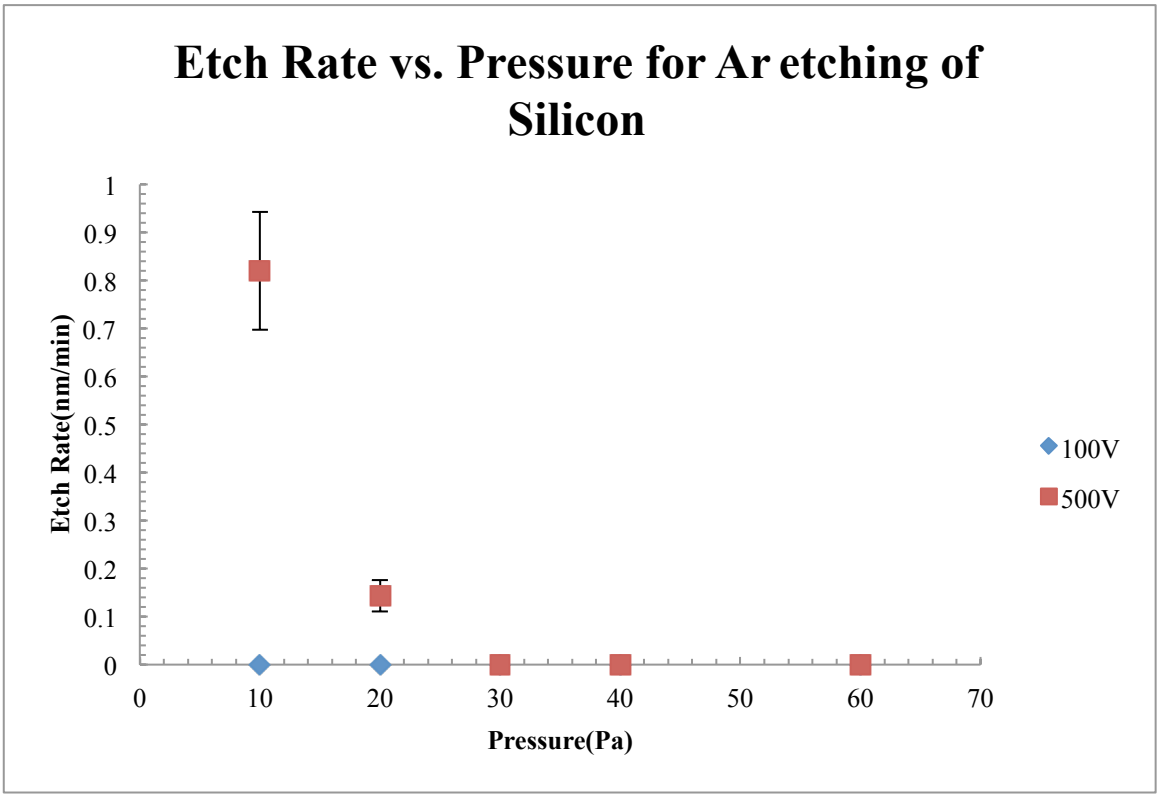


Figure 4.2. Etch Rates of Silicon vs. Pressure under Argon Plasma

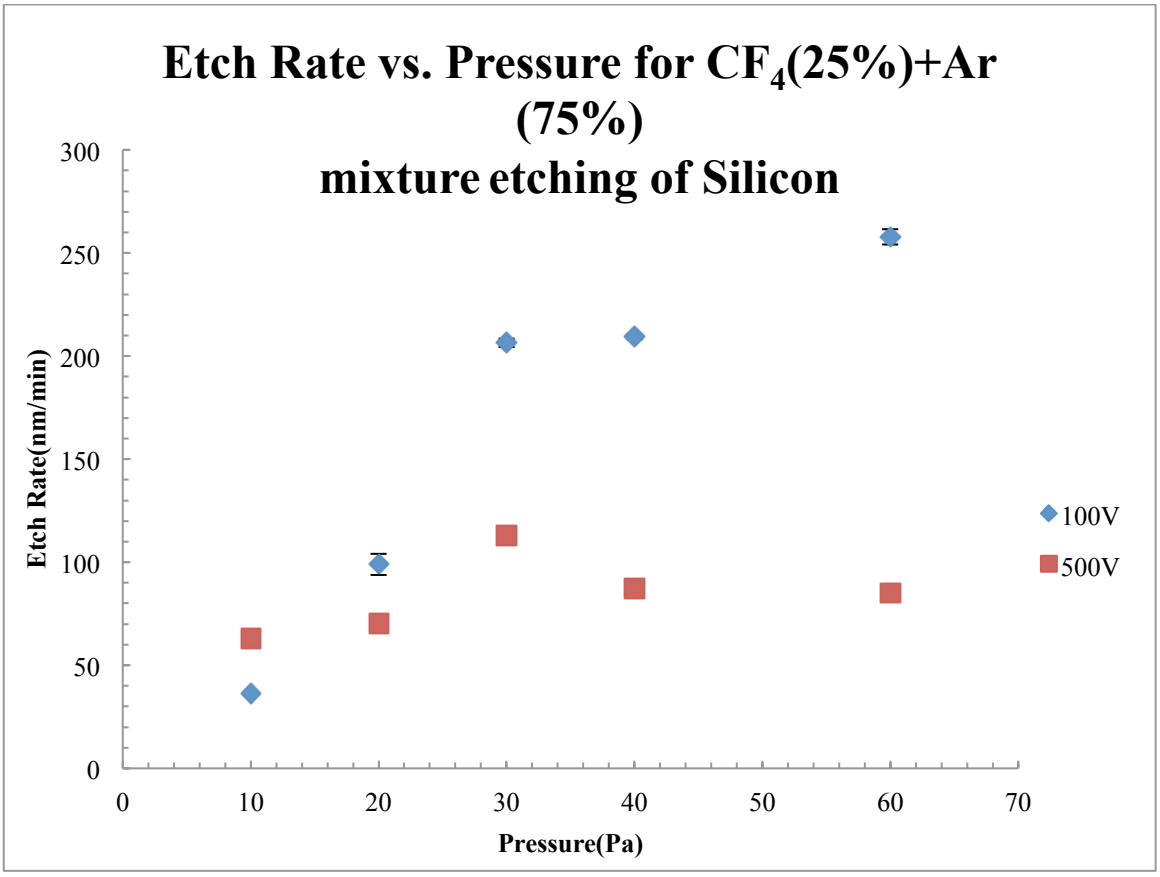


Figure 4.3.Etch Rates of Silicon vs. Pressure under CF_4(25%)+Ar(75%) Plasma mixture

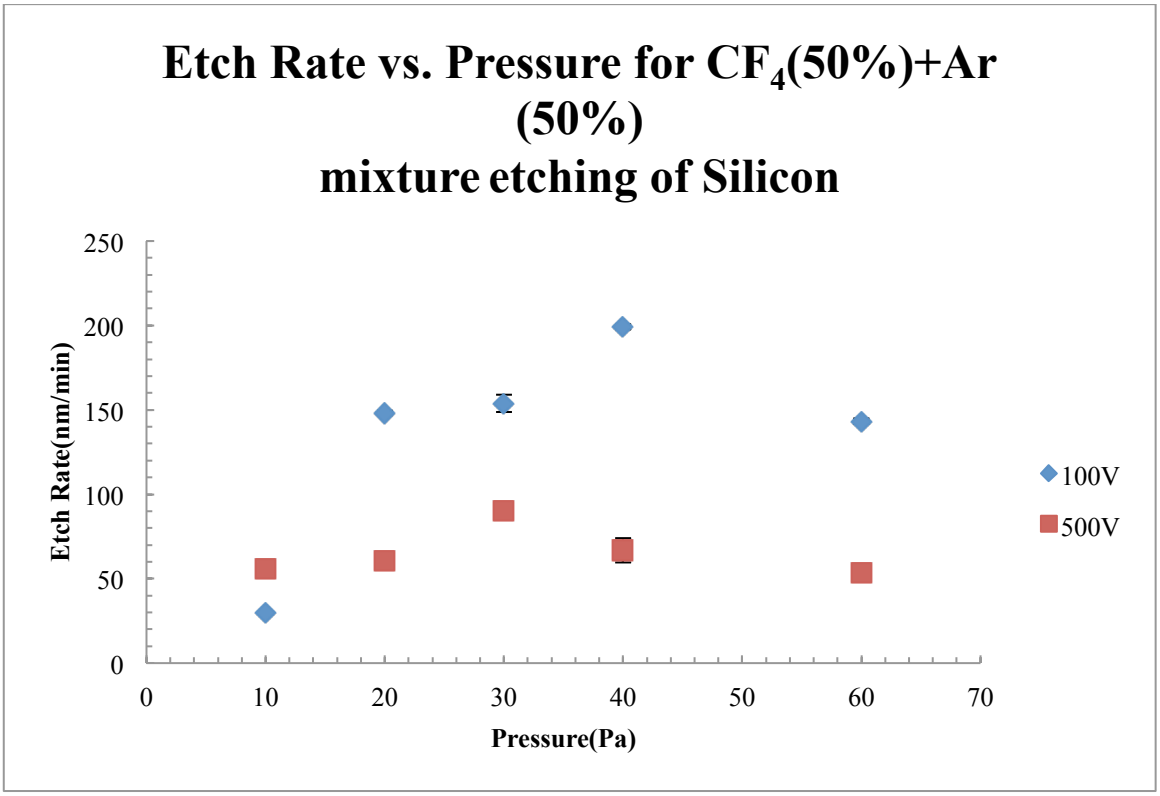


Figure 4.4.Etch Rates of Silicon vs. Pressure under CF_4(50%)+Ar(50%) Plasma mixture

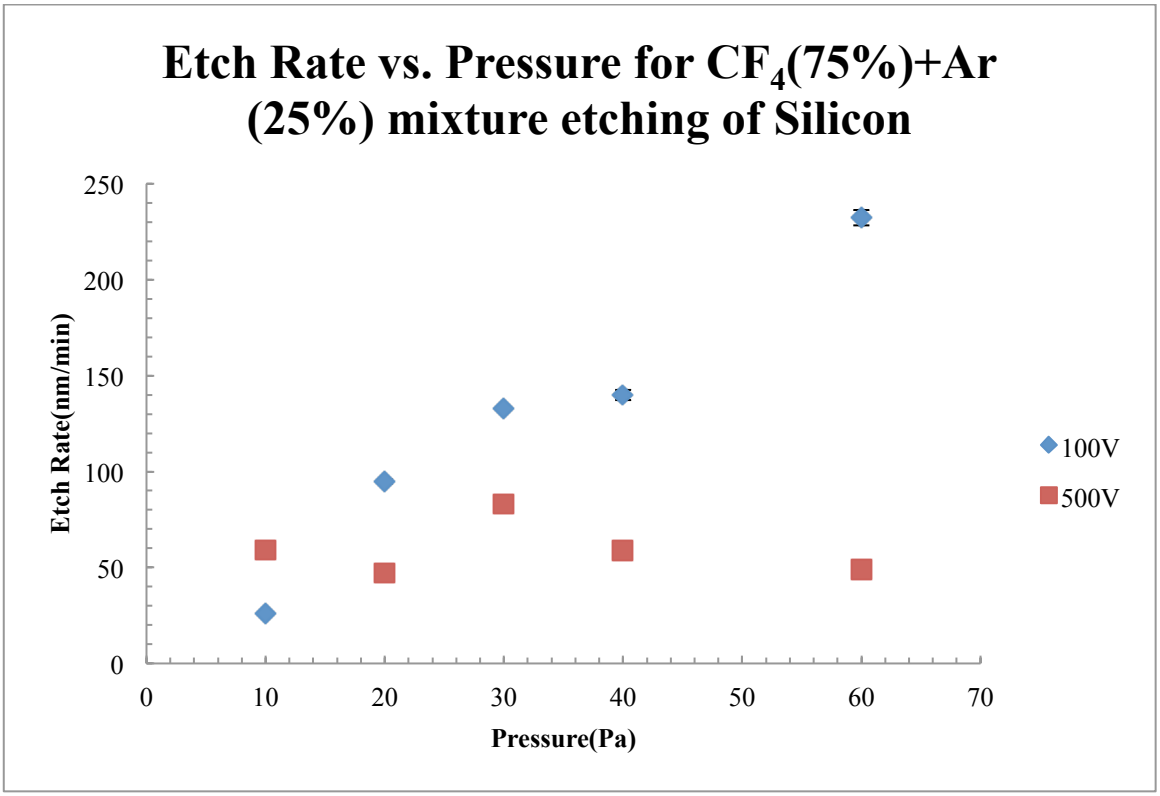


Figure 4.5. Etch Rates of Silicon vs. Pressure under CF_4(75%)+Ar(25%) Plasma mixture

From the measurment results, the highest etch rate of silicon by using only Tetraflouromethane(CF_4) gas as the chemical etchant is around 0.17µm/min. The highest etch rate of silicon by using only Argon(Ar) gas as the ion bombardment etchant is around 2nm/min. The ion bombardment is similar to the sputtering mechanism, where the material is removed from a surface by energy and momentum transferred in energetic ion bombardment. This process is unselective and generally slow. The chemical etching process is crucial to fabricating high aspect ratio MEMs structures, because the reactive neutral free radicals are mainly responsible for the etching the silicon wafer as they are more abundant and arrive at the cathode surface by non-directional diffusion. These free radicals are generated at lower threshold energy typically less than <8eV, whereas the Ar is ionized at 15.7eV and they have longer lifetime in the plasma than the charged ions. This etching mechanism is not limited by the ion current to the surface nor by the mean free path unlike the ion bombardment mechanism. Figure 4.1 shows the relationship between the etching rate and the pressure and the RF bias for CF_4 etchant, the etching rate is generally higher for etching process operated at low RF bias, because high RF bias direct CF_x^+ ions towards the Si that may produce sputter contamination which passivates the surface and prevents further etching. With increasing pressure, the number of fluorine radicals

in the plasma increases, which results in increased etching rates of silicon. Figure 4.2 demonstrates the relationship between the etching rate and the pressure and the RF bias for Argon etchant, the highest etching rate is achieved at low pressure and high RF bias, because the charged Ar^+ ions are accelerated at high bias with higher bombardment energy and the pressure is low enough for the high energetic ions travel across the reactor with few collisions.

From Figure 4.3 to 4.5, the etch rate of silicon at 50Pa have been removed from the results, because there is a repetitive decrease at this specific pressure and it has been tested for CF_4 etching gas specifically. Samples were repeated at 50Pa initially to validate the results and the results were similar to the previous results. Thus, the samples were etched at 48Pa, 49Pa, 51Pa and 52Pa to examine the results, and it shows that the etch rate at 49 and 50Pa do not fit the trend and appears to be an anomaly from the rest of the results. The possible explanation for the decreasing etch rate can be due to the photoresist being not fully dissolved in the developer or the pressure gauge in the reactive ion etcher is inaccurately calibrated.

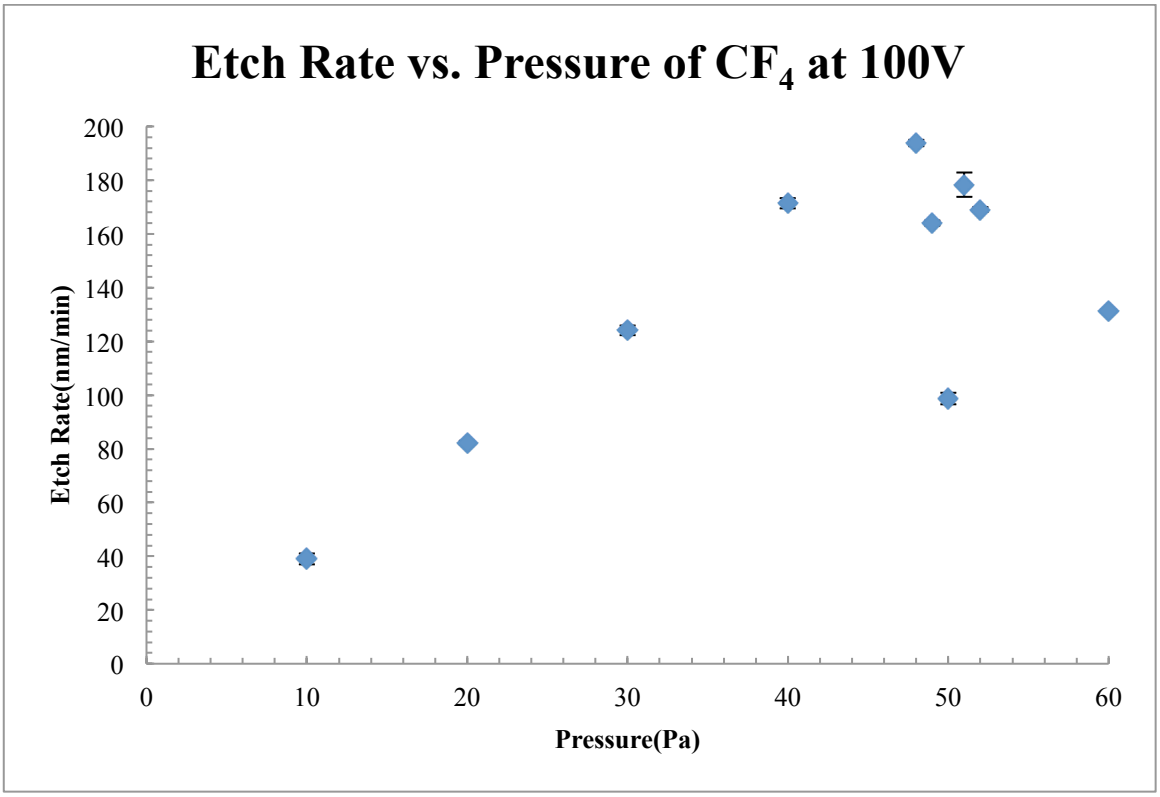


Figure 4.6. Etch Rates of Silicon vs. Pressure under CF_4 at 100V RF bias

By using a combined plasma mixture of Tetraflouromethane(CF_4) and Argon(Ar) gas, the highest etching rate of silicon was around 0.25µm/min. This ion bombardment assisted plasma etching mechanism is based on the principle of ion bombardment

enhancing the chemical etching process, where the argon ion bombardment increase the number of adsorption sites by destroy a large number of Si-Si and Si-F bonds inside of the SiF_x surface and replace them with SiF_4 and SiF_2 molecular groups that are weakly bound to the surface, thus allowing the chemical reactions of CF_4 with silicon to take place more easily. Silicon etching rate of 0.23 μm/min was achieved with CF_4(75%)+Ar(25%) mixture plasma compared to other ratio mixtures, because it is important to allow the reactive chemical species to remain as main etchant for silicon and use ion bombardment only as an enhancement step to the etching reaction. When adding small amount of oxygen to this mixture of CF_4 and Ar plasma, the etch rate increased dramatically, because the oxygen reacts with CF_x radicals to form CO_2 and COF_2, which reduces the recombination of F atoms with CF_3 again increasing the density of fluorine atoms available for chemical etching. However, at a higher oxygen addition, a passivating inorganic $Si_xO_yF_z$ film is formed on the Si surface and the etch rate is related to the thickness of the passivating film rather than the density of the fluorine atoms, so the etch rate falls. Excess amount of oxygen will decrease the density of the fluorine atoms due to dilution. The effect of oxygen addition was compared for CF_4(25%)+Ar(75%) plasma mixture and CF_4(75%)+Ar(25%) plasma mixture at 60Pa to find the optimal oxygen levels to add to the mixture to reach the highest etching rate, which is of 5sccm O_2 added to CF_4(75%)+Ar(25%) mixture. In Figure 4.7 and 4.8, the experiment is carried out at RF bias of 100V and Pressure 60Pa, because the experimental results show that higher etching rate is achieved at lower accelerating voltage for the ion enhanced reactive ion etching process as the ion will induce damage/weakening of the chemical bond of silicon. The effect of oxygen addition to the ion enhanced plasma was tested at 60Pa, because the pressure is in the middle of the reactor's pressure range and the final reactive ion etching conditions chosen for fabricating the air cavity was performed at 60Pa.

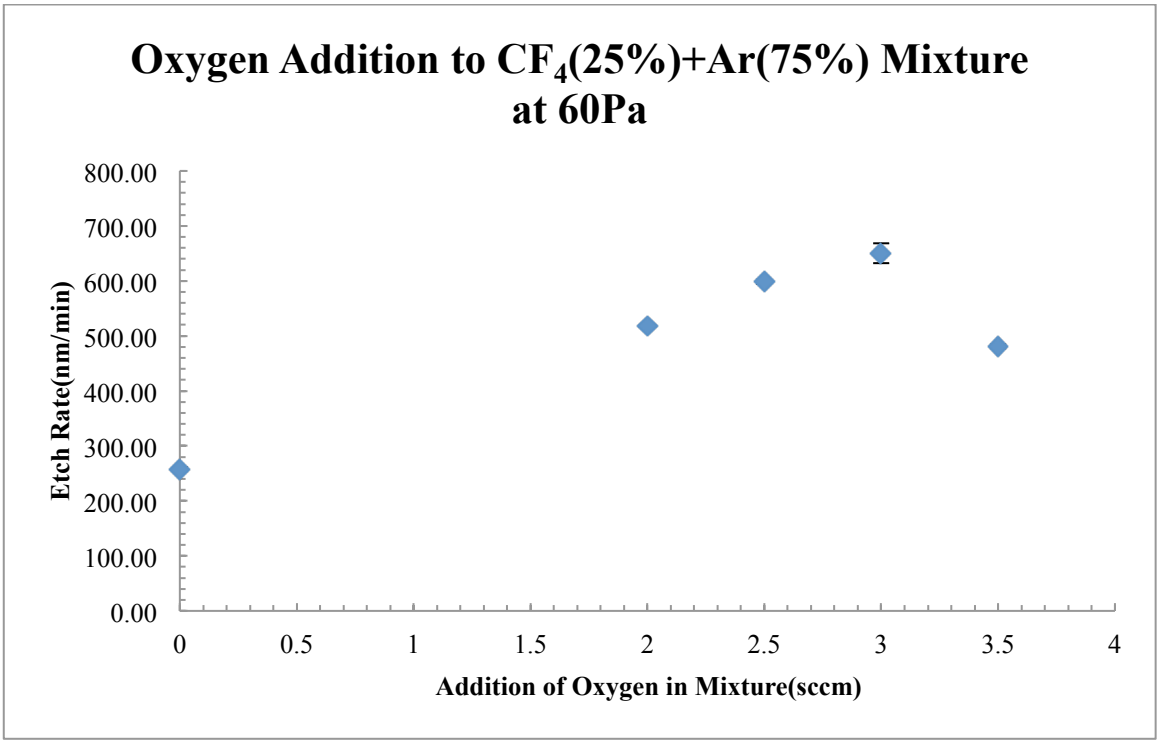


Figure 4.7. Etch Rates of Silicon vs. Addition of Oxygen in CF_4(25%)+Ar(75%) Plasma mixture at 60Pa

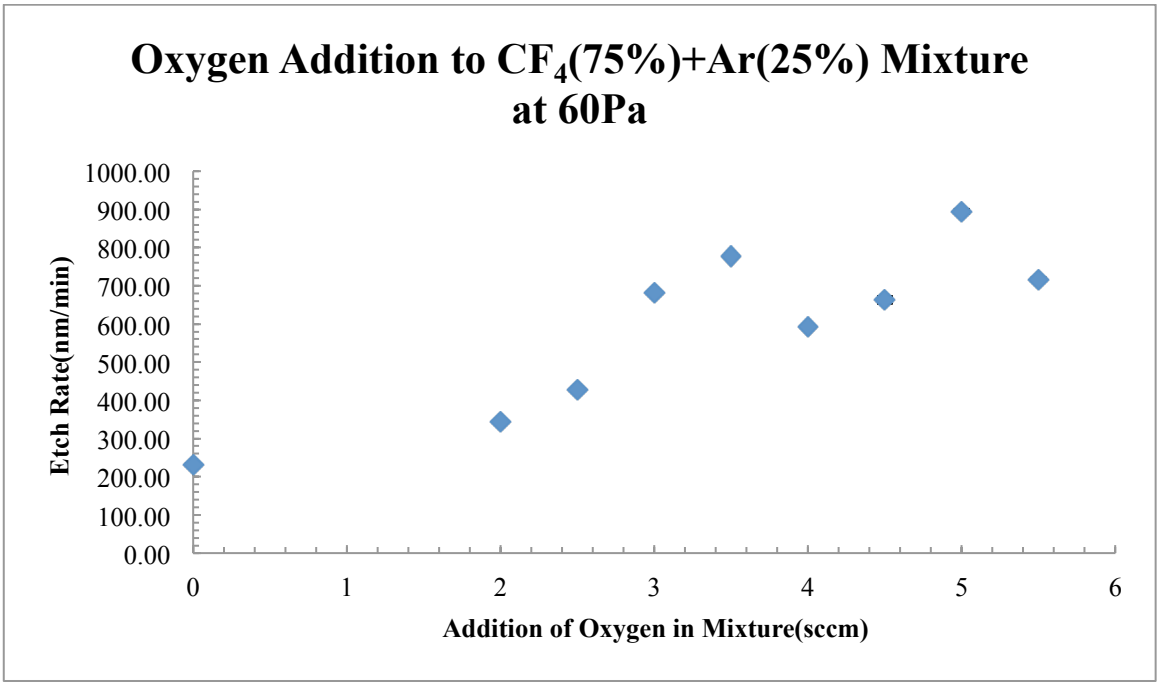


Figure 4.8.Etch Rates of Silicon vs. Addition of Oxygen in CF_4(75%)+Ar(25%) Plasma mixture at 60Pa

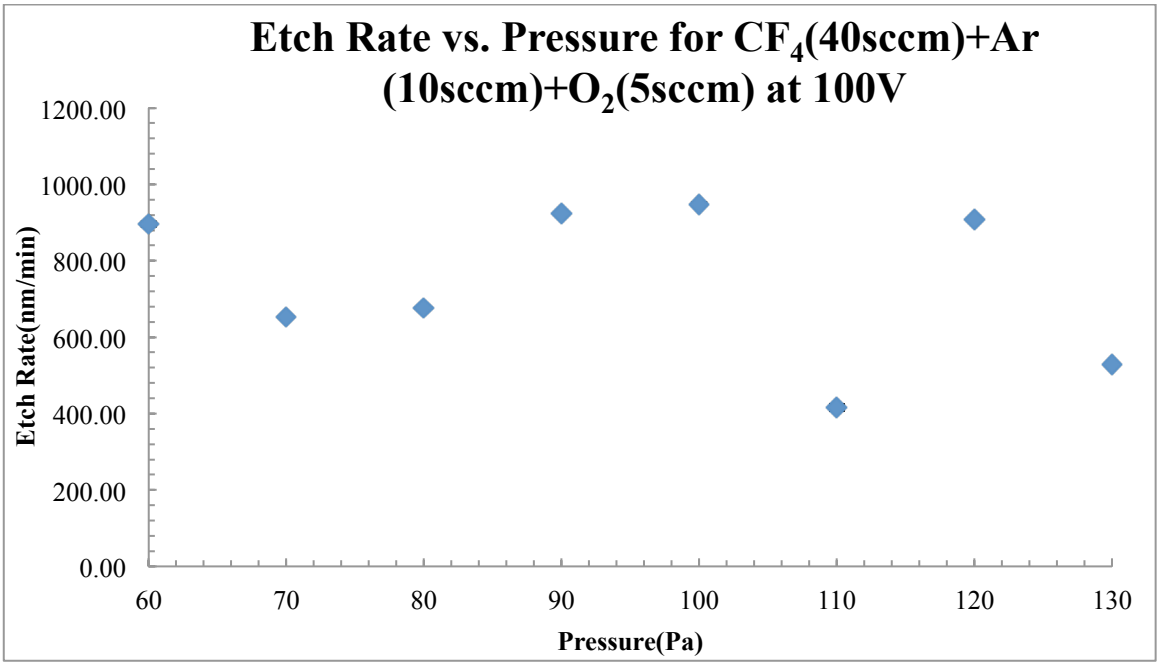


Figure 4.9.Etch Rates of Silicon vs. Pressure in CF_4(40sccm)+Ar(10sccm)+O_2(5sccm) Plasma mixture at 100V RF bias

Figure 4.9 shows that the effect of pressure on the etch rate using determined etching mixture of CF_4(40sccm)+Ar(10sccm)+O_2(5sccm) and the etch rate between the 60Pa, 90Pa, 100Pa and 120Pa are similar. At this point, the etch rate of silicon is maximized at around 1 µm/min using etching mixture of CF_4(40sccm) +Ar(10sccm) +O_2(5sccm) at 60Pa pressure and 100V RF bias voltage.

4.2 Choice of the masking material for Si reactive ion etching

Dry etching of Si substrate was require to be tested and optimized before the resonator fabrication, because overetching of the silicon substrate may destroy the resonator device on the other side. After the device patterning of the resonator multilayer structure on the substrate, the substrate has to be etched from the backside to eliminate the undesirable effects of substrate clamping to the resonator. Wet etching of Si substrate was not used in this process, because it has a relatively slow etch rate of 0.5 µm/min and may introduce contaminants to the surface and there is a difficulty to protect the device.

The silicon substrate was etched using a new deep silicon etching process involving a plasma of CF_4+Ar+O_2 with the assistance of metal masking using a reactive ion etcher system(Sentech Etchlab 200). This technique is an alternative to the Bosch and Cryogenic DRIE methods, where the silicon etch rate is comparable with compromising isotropy. This is developed as it is cost effective and the expensive DRIE system was not readily accessible at Imperial College. It was found that an

optimized etching recipe of around 1µm/min with a aspect ratio of 5:1 could be achieved using a gas mixture of CF_4 (40sccm)+Ar (10sccm)+O_2 (5sccm) under 100V RF bias and 60Pa mixture gas pressure. The optimization results was previsouly discussed in subchapter 4.1. The reactions occur during the etching process of the silicon substrate is shown in Figure 4.10.

$$CF_{4(g)} + e^- \leftrightarrow CF_3^+ + F^* + 2e^-$$

$$Si_{(s)} + 4F^* \rightarrow SiF_{4(g)}$$

$$Ar_{(g)} + e^- \rightarrow Ar^+ + 2e^-$$

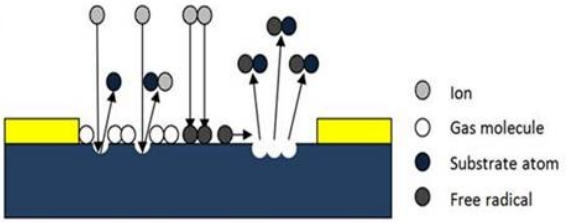


Figure 4.10. The chemical and physical reactions occurring during the etching process

A photoresist mask was initially used for etching the Si substrate, but the addition of O_2 has decreased its lifetime significantly in the process, thus in this study it was replaced by metal mask.

The metal masking layer for the substrate micromachining was made through the following route shown in Figure 4.11.

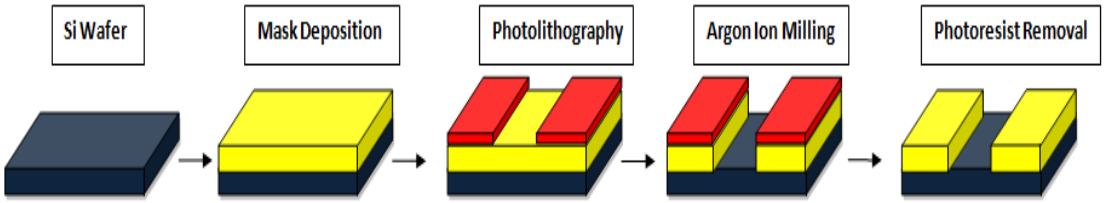


Figure 4.11. The mask fabrication processing route

Several metal masks were compared with the photoresist mask in this etching process, Table 4.1 compares the different mask materials for one layer setup and multilayer setup. As one can see some of the metal masks have longer lifetimes during the reactive ion process than the conventional photoresist (AZ 5214 E). Also, it is seen that certain metals (e.g. gold) enhance the silicon etch rate, due to its dehalogenation catalytic ability i.e. the ability to assist production of fluorine free radicals from the fluorinated metal surface.

Gold appears to be the best silicon masking material because it was the strongest catalyst (i.e. enhances silicon etch rate); it was both chemically and physically resilient, it was easy to pattern, and it can be selectively removed (e.g. using wet chemistry) after the etching process.

Etching Mask Material	Etch Rate of Mask (nm/min)	Etch Rate of Silicon (μm/min)	Etch Selectivity
Photoresist	93	0.9	10:1
Gold	5	3.8	760:1
Titanium	7	0.03	5:1
Niobium	150	0.3	2:1
Chromium	2	0.9	450:1
Silver	10	1.0	100:1
Aluminium	1.3	0.9	690:1
100nm Au/100nm Ti	7	5.3	760:1
50nm Au/50nm Ti/50nm Au/50nm Ti	8	7.5	940:1
100nm Au/100nm Ti/100nm Au/100nm Ti	9	11	1200:1

Table 4.1. The etch rates of Si and different masking materials

Below we will briefly explain the dehalogenation process that occurs on the silicon sample surface covered with gold mask. When CF_4 gas was introduced to the reactor and plasma was sparked, the metal (i.e. Gold) surface become partially or fully fluorinated, which in turn catalyzes the dehalogenation process.

$$CF_4+e^-\rightarrow CF_3^++F^*+2e^-$$

$$CF_4+e^-\rightarrow CF_3^++F^-+e^- \quad (4.1)$$

$$Au+CF_3^++O_2\rightarrow AuF_3+CO_2 \quad (4.2)$$

$$AuF_3\rightarrow AuF+F_2 \quad (4.3)$$

$$F_2\rightarrow 2F^* \quad (4.4)$$

The level of metal surface fluorination process depends on the electronegativity, while the dehalogenation process (that dependents on the bonding energy of the metal fluoride compound) governs the creation of free fluorine radicals, necessary for the silicon etching process.

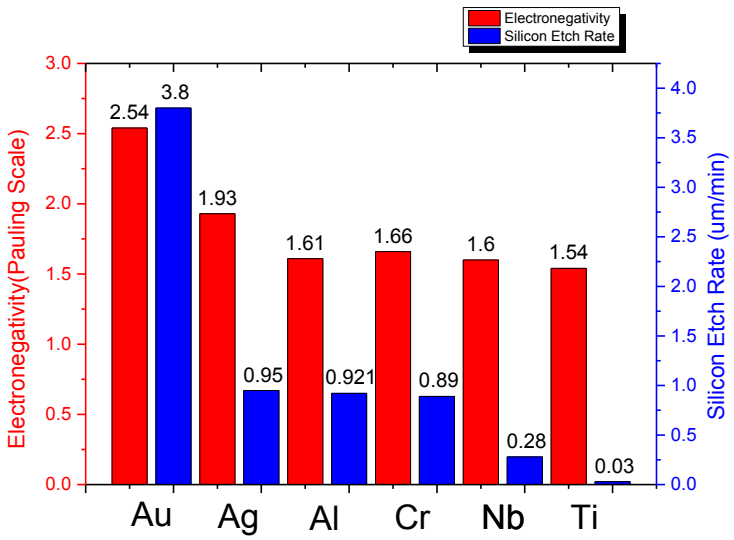


Figure 4.12. The relationship between Electronegativity (left (red in colour) bars, corresponding to the left Y-axis) and the Silicon Etch Rate (right (blue in colour) bars, corresponding to the right Y-axis). The X-axis (not to scale) shows the masking material symbol.

Figure 4.12 graphically represents the relationship between the electronegativity (left (red in colour) bars, corresponding to the left Y-axis) and the Si etch rate (right (blue in colour) bars, corresponding to the right Y-axis). The X-axis (not to scale) shows the masking material symbol. As one can see, there was a clear trend of increased silicon etch rate when masking metal with higher electronegativity is used. The Cr metal fluoride is found to be more reactive and thermally unstable than the Nb metal fluoride even though the electronegativity values between them are similar.

The obtained values for the metallic multilayer masks etching rates and corresponding Si etch selectivity coefficient are presented in table 4.2.

Mask Multilayer	**Initial Feature**	**Feature Depth(µm)**	**Sidewall Slope(°)**	**Undercut(µm)**	**Degree of Anisotropy[1]**

	size(µm)				
100nm Au/100nm Ti	129	145	55	120	15%
50nm Au/50nm Ti/50nm Au/50nm Ti	129	100	50	120	9%
100nm Au/100nm Ti/100nm Au/100nm Ti	129	165	60	130	14%

[1] Degree of Anisotropy is calculated by the following formula- $A_f = 1 - \frac{r_{lat}}{r_{ver}}$, where r_{lat} is the lateral etch rate and r_{ver} is the vertical etch rate.

Table 4.2. The etching rates of different multilayer masking structures against the reactive plasma

Gold was used as the top layer in all multilayer structures as it exhibited the highest silicon etch rate. Titanium displayed the lowest etch rate in the reactive plasma and it was known for its role as good adhesive layer for metal multilayers. The results also showed that Ti/Au multilayer is a good mask for deep silicon etching exhibiting higher selectivity even though the mask lifetime slightly decreased. Also, the multiplication of the Ti/Au bilayer stacks and the increase of the gold layer thickness in the multilayer mask structure improved the etching selectivity by nearly a factor of two.

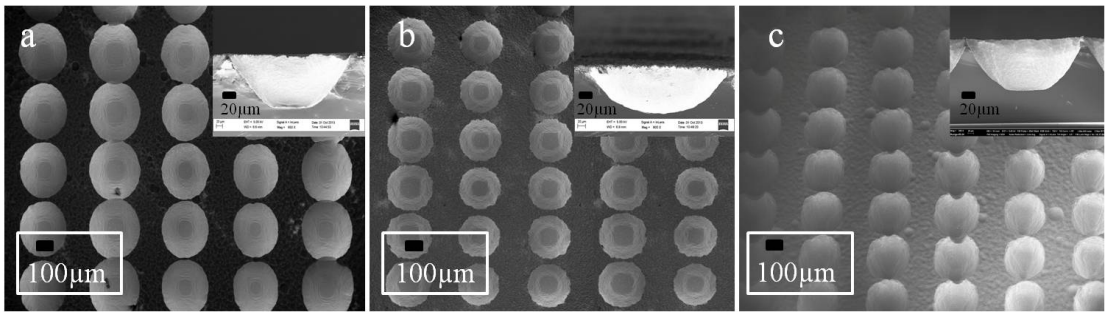


Figure 4.13. The SEM Images of Si etching profiles using different masking multilayer structures: (a) Top and Cross Section Images after 15mins Etching with 100nm Au/100nm Ti Mask;, (b)- Top and Cross Section Images after 15mins Etching with 50nm Au/50nm Ti/50nm Au/50nm Ti, (c)-Top and Cross Section Images after 15mins Etching with 100nm Au/100nm Ti/100nm Au/100nm Ti Mask.

From Figure 4.13, the SEM images have shown that the 100nm Au/100nm Ti (Multilayer 1) masking catalyzes production of the F* free radicals more significantly than the 50nm Au/50nm Ti/50nm Au/50nm Ti(Multilayer 2), because the Gold atoms on the top layer of the multilayer structure 1 are in direct contact with the CF_4 atoms, so the rate of catalysis will be higher. The etch rate of the Si has decreased when the

number of multilayers in the masking structure increased. However, the aspect ratio of the Si etched by using multilayer masking structure 2 is improved to 8:1 from 4:1 by using multilayer masking structure 1. The etch selectivity of the Si etch process is also increased with the increase in the number of layers in the mask multilayer structure. This is because the direct contact between the gold layer with the fluorine free radical will cause instanteous dehalogenation reaction rather than controlled reaction in applying multilayer mask structure. The contact between the gold layer and the fluorine radical is more controlled as the Titanium layer separates them. For Si etching with all multilayer masking structures, the trend is as the etching time increases, the time allowed for the catalysis reaction is also increased, thus the Si etching rate is gradually increased.

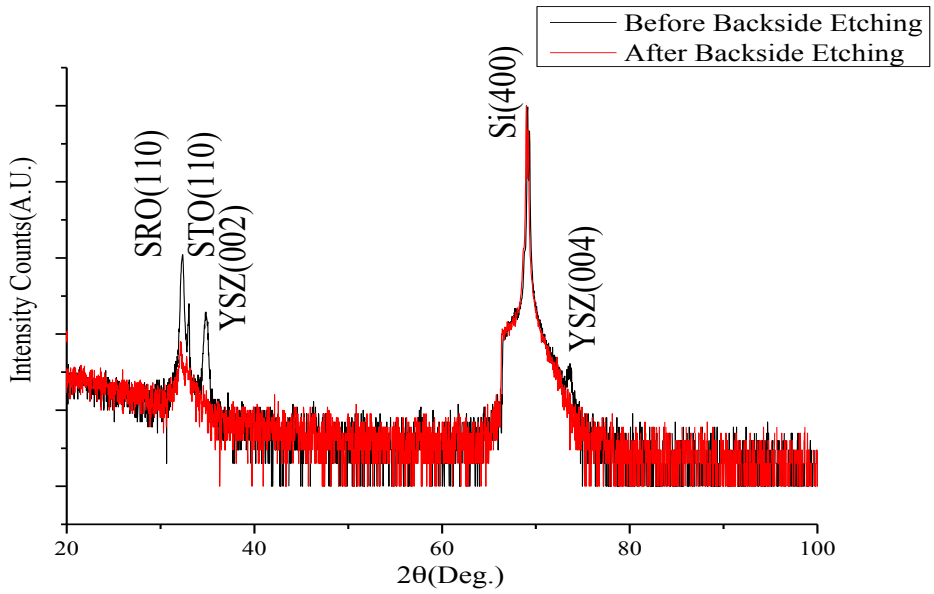


Figure 4.14. X-ray diffraction pattern of the multilayer structure before and after the backside etching process

After the etching process of the Si substrate was performed with the protection of the resonator devices, it was characterized using X-ray diffraction to examine whether any of the multilayer films have been etched away. The result was shown in Figure 4.14, which shows the intensity of the film peaks were all lower after the substrate backside etching, this was inevitable due to possible etching reaction between the reactive plasma and the films, which deteriorated the film quality. Aluminum was chosen as the best protection layer out of the metal and oxide films in this alternative etching process, because it was found to be resistant against the plasma and can be easily removed after use by acid etchants. This will solve the problem of protecting the device side while maintaining the functionality of the free standing resonator structure.

4.3 Conclusions

In this chapter describes the MEMS patterning process and explains the process of substrate air cavity formation using selective deep silicon etching. A new technique of metal assisted reactive ion etching of silicon substrate was developed during this project.

The selective removal of Si underneath the resonator device would eliminate the substrate clamping effect and damping of the acoustic wave resonance. Also, the aluminum metal will protect the device side while the substrate was selective etched from the backside. These findings will be important to the success of fabricating a novel freestanding tunable bulk acoustic resonator on silicon substrate.

The next chapter will present the resonance characterization results of this novel bulk acoustic wave resonator using paraelectric state strontium titanate film in a multilayer structure.

Chapter 5. Fabrication of a ferroelectric based tunable thin-film bulk acoustic wave resonator

This chapter introduces the device design of an electrically switchable bulk acoustic wave resonator employing two stacking structure and the fabrication of ferroelectric thin film based multilayer structure for the tunable bulk acoustic wave resonator. The measurement of the acoustic resonance of the fabricated bulk acoustic wave resonator employing one stacking structure is presented and compared with the theoretical modelling.

5.1 Device Design

The simplest switchable resonator device design was based on two tunable bulk acoustic wave resonator stacked together where the central electrodes are electrically grounded. The configuration was shown in Figure 5.1.

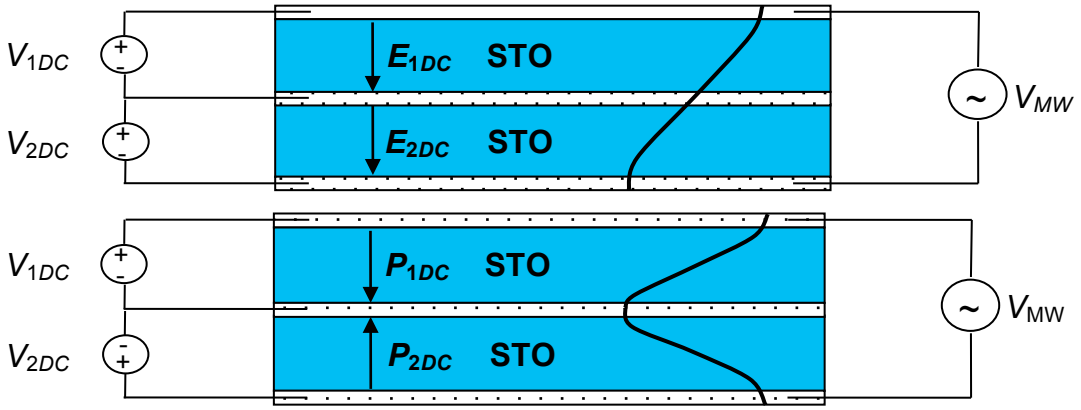


Figure 5.1. Bulk Acoustic Wave Resonator Configuration

The acoustic resonance was induced by applied a microwave signal to the entire resonator structure. By applying same magnitude of electric field in the same direction in the mode A, the resonance at approximately quarter wavelength across each ferroelectric layer is excited. By applying same magnitude of electric field in the opposite direction in the mode B, the resonance at half wavelength across each ferroelectric layer was excited. The application of opposite electric field to each ferroelectric layer can result in the suppression of parasitic resonances(in terms of microwave power losses). Along with the possibility to suppress the parasitic resonance losses in the ferroelectric layer, this resonator design was considered an electronically switchable bulk acoustic wave resonator.

By using this device design, the transformation of microwave energy into acoustic vibrations (under application of electrical field) were utilized to produce a novel tunable bulk acoustic

wave resonator. This bulk acoustic wave resonator setup was also switchable between two different frequencies, making it very promising in the demanding communications industry today.

The details of the device performace modelling are provided in the Appendix I.

5.2 Device Mask Design

The first steps of the resonator fabrication process were the device design and mask fabrication. Different sized resonator design were drawn up and repeated over a 8×8mm active mask area.

Three sets of mask patterns with alignment grids were designed for each layer of the multilayer structure, one for the bottom electrode, one for the ferroelectric layer and one for the top electrode. There was one more set of mask pattern for the backside etching of the silicon substrate only. The microscopic images of these mask pattern designs are shown in Figure 5.2-5.5.

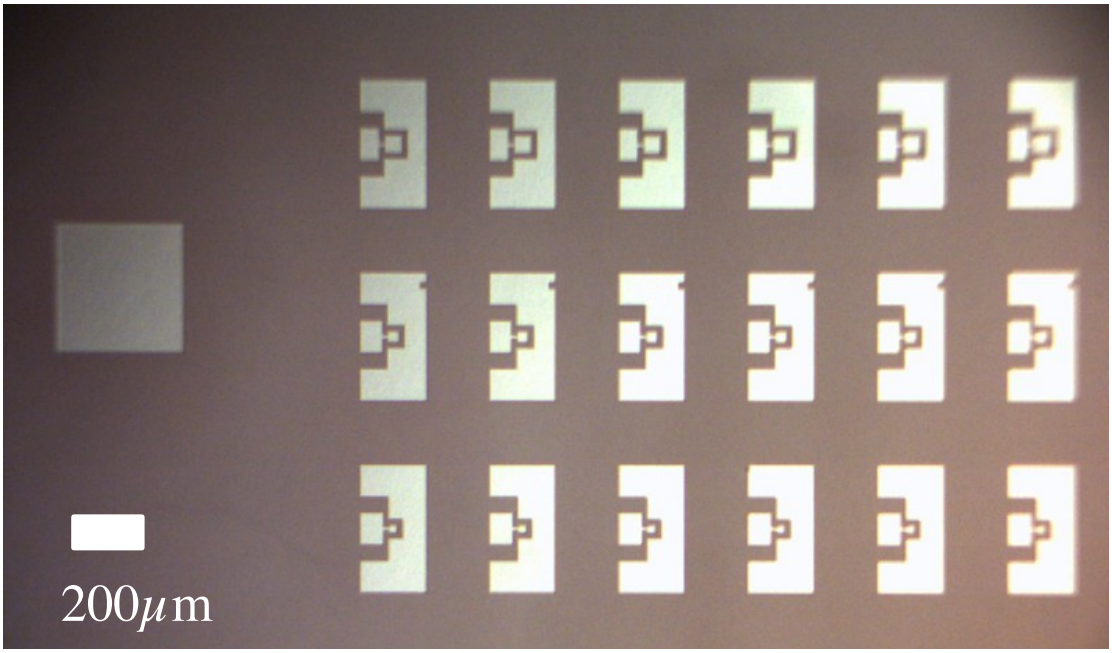


Figure 5.2. Microscopic image of the bottom electrode pattern

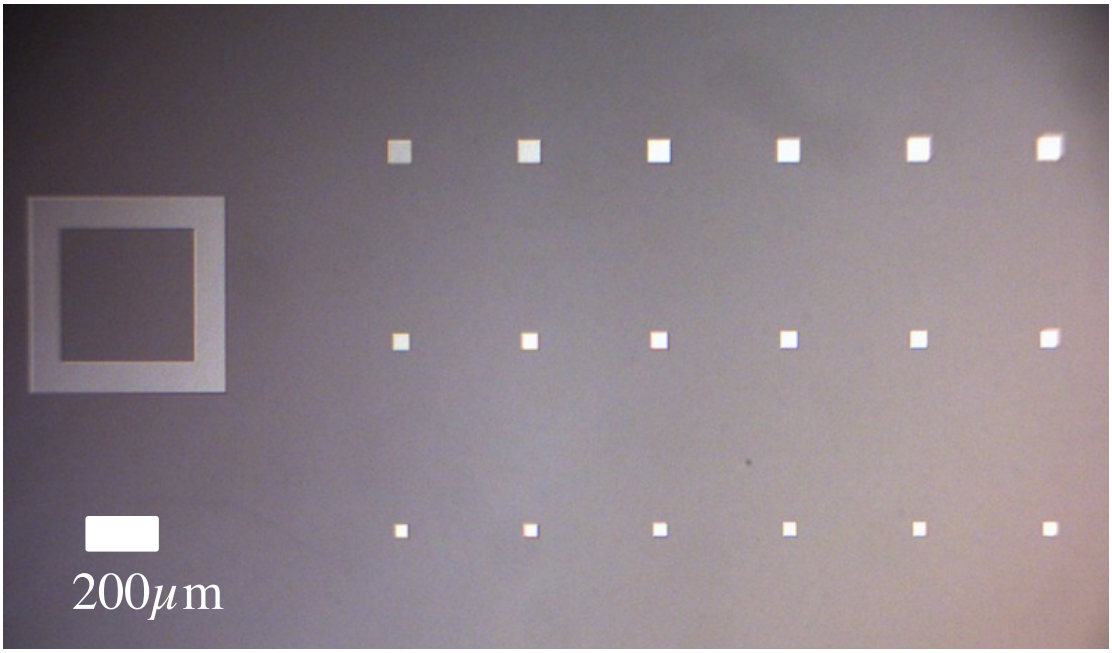


Figure 5.3. Microscopic image of the ferroelectric layer pattern

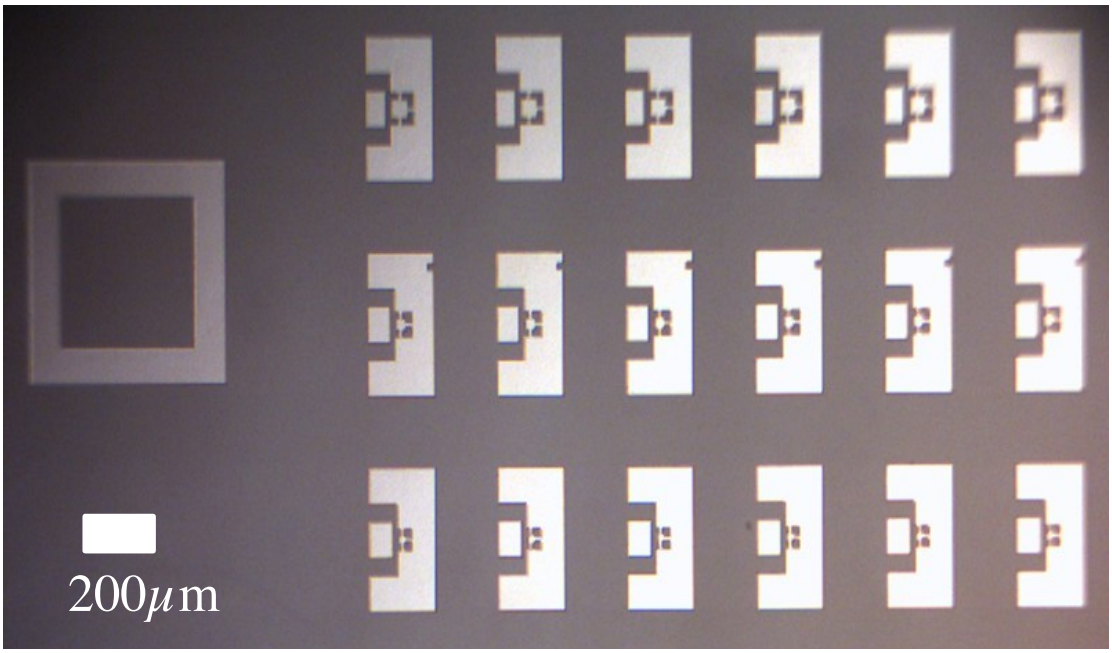


Figure 5.4. Microscopic image of the top electrode pattern

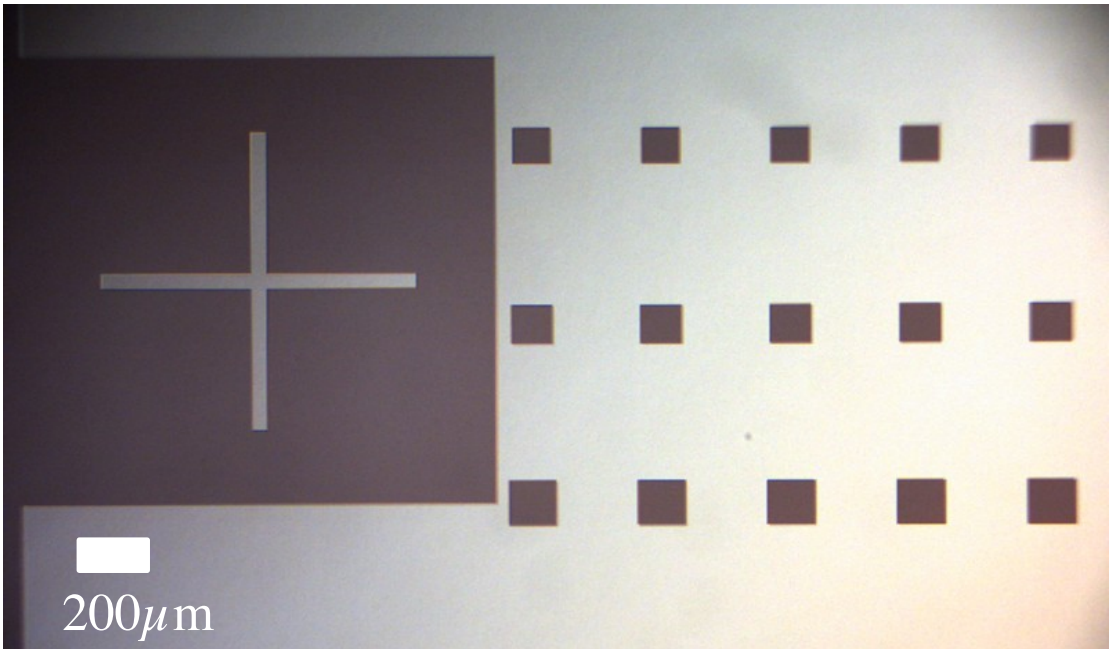


Figure 5.5. Microscopic image of the substrate backside etching pattern

These images of the photomask patterns showed that the pattern alignment required after deposition of each layer in the multilayer resonator structure. They must be accurately aligned to in the following sequence-BE(Bottom Electrode)/ AL(Active Layer)/ TE(Top Electrode) and at last the substrate etching pattern must be aligned from backside. These patterning processes must be accurately performed to ensure the successful fabrication of the multilayer resonator device.

5.3 Resonator Patterning

The device patterning process included photoresist spin coating, photomask alignment and U.V exposure, pattern development and ion beam milling. The photomask alignment and U.V exposure were performed using a Karl Suss MJB3 contact mask alignment system. Photoresist AZ 5214E was spin coated onto the thin films at a speed of 4000rpm for 30 seconds using Suss Microtech spin coater. The coated films were exposed under 400nm UV light source for 35 seconds and then developed for 10s in the AZ 400K developed solution from Microchemicals GmbH. When the patterning was completed, then ion beam milling step was performed to etch the metal oxide thin films using Oxford Applied Research IM 150. These steps were repeated for each layer of the multilayer resonator structure.

In the following Figure 5.6 to 5.9, each step of fabricating the resonator device were shown and labeled, thus provide a detailed step by step guide to the process and depicts any possible difficulties encountered.

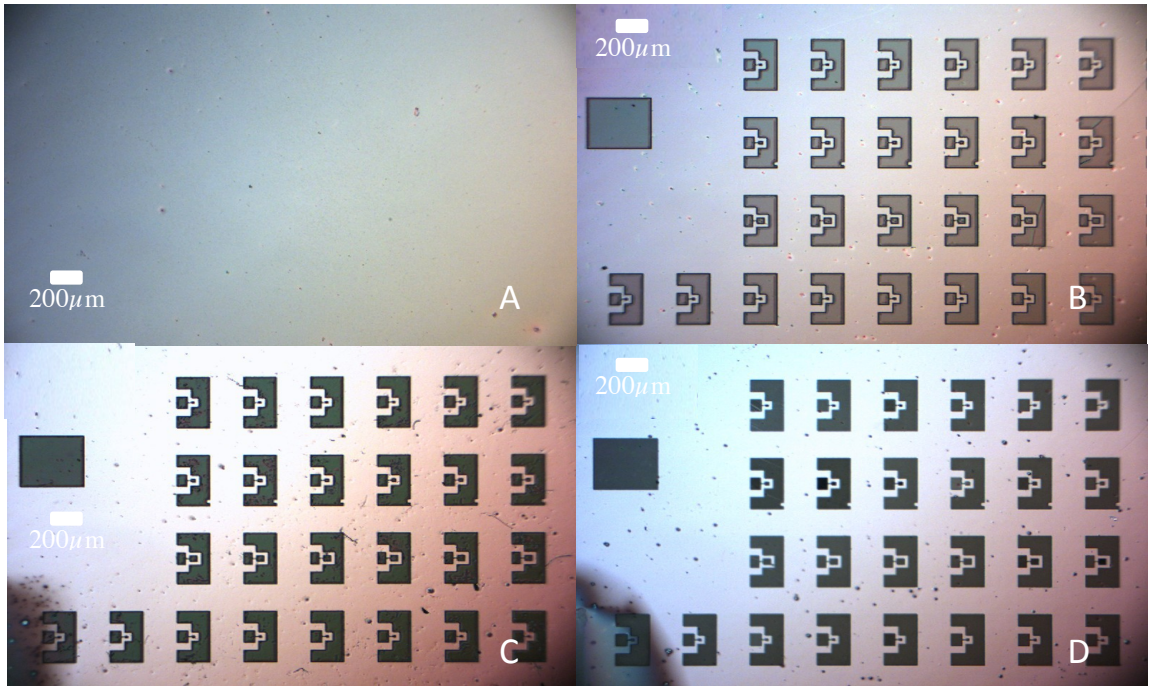


Figure 5.6. Microscopic image of the Bottom Electrode Layer patterning on the $SrRuO_3$+YSZ layer, A) $SrRuO_3$+YSZ film on Si substrate, B) After Photolithography Patterning on $SrRuO_3$+YSZ film on Si substrate, C) After Ion Beam Milling of $SrRuO_3$+YSZ film on Si substrate and D) After Photoresist Liftoff on $SrRuO_3$+YSZ film on Si substrate

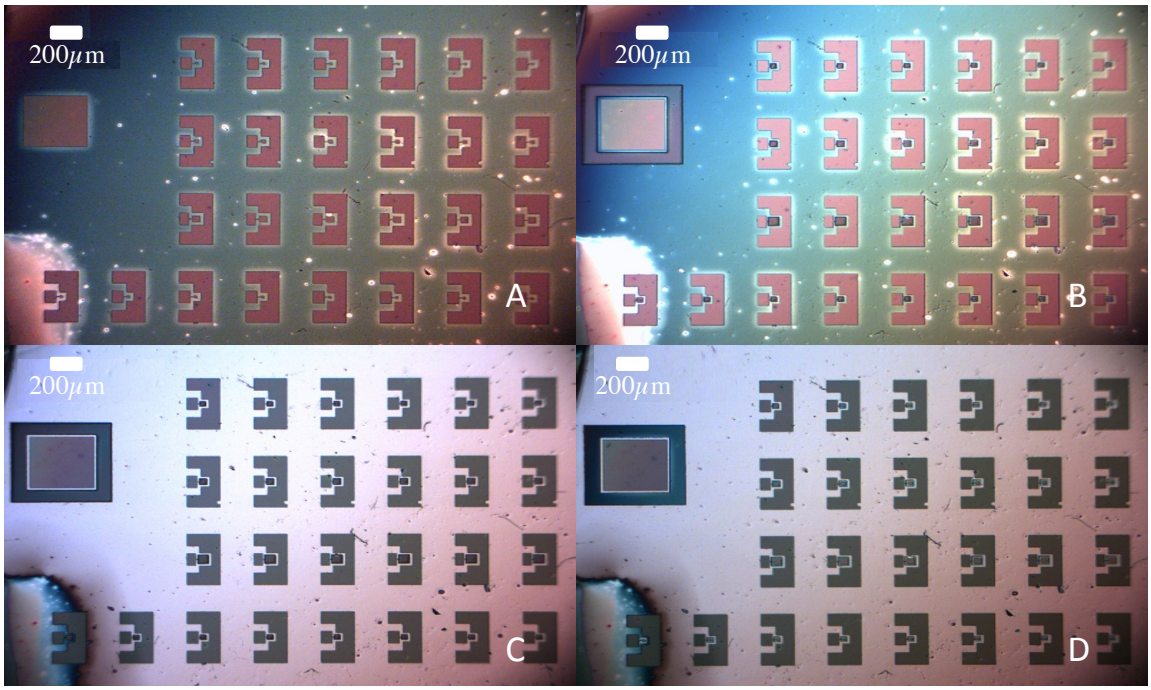


Figure 5.7. Microscopic image of the Active Layer patterning on the $SrTiO_3$+$SrRuO_3$+YSZ layer, A) $SrTiO_3$ deposited on patterned $SrRuO_3$+YSZ film on Si substrate, B) After Photolithography Patterning on $SrTiO_3$+$SrRuO_3$+YSZ film on Si substrate, C) After Ion

Beam Milling of $SrTiO_3$+$SrRuO_3$+YSZ film on Si substrate and D) After Photoresist Liftoff on $SrTiO_3$+$SrRuO_3$+YSZ film on Si substrate

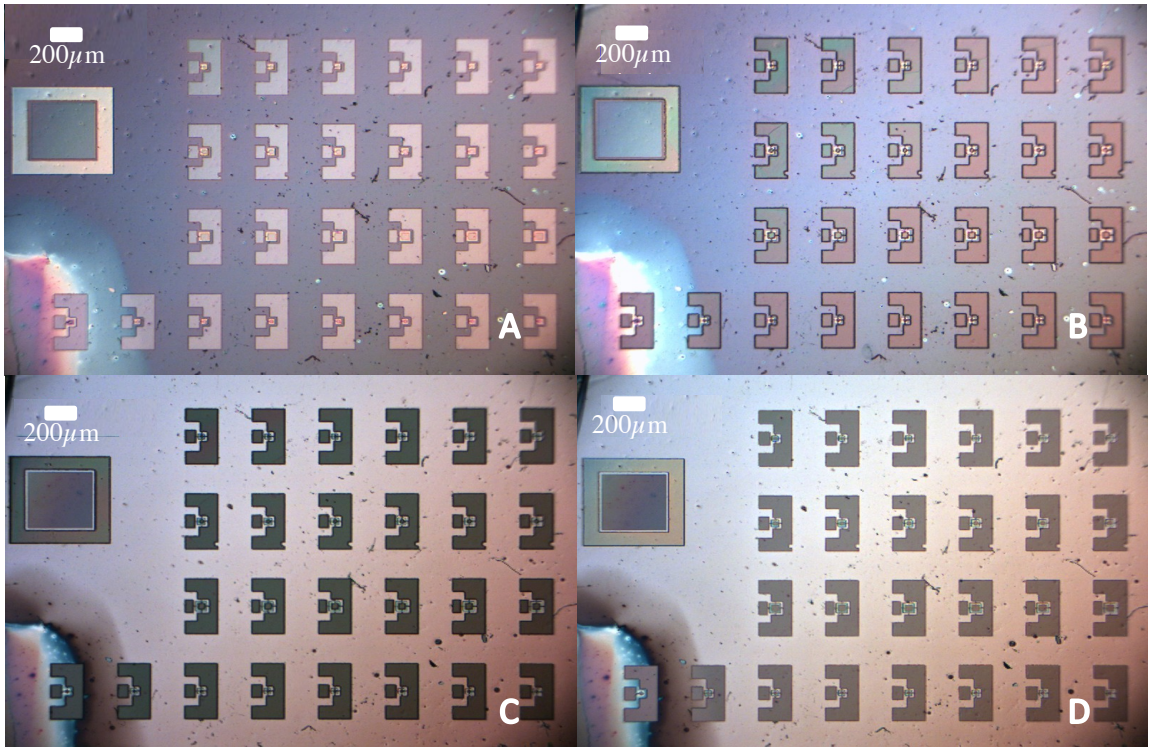


Figure 5.8. Microscopic image of the Top Electrode Layer patterning on the $SrRuO_3$+$SrTiO_3$+$SrRuO_3$+YSZ layer, A) $SrRuO_3$ deposited on patterned $SrTiO_3$+$SrRuO_3$+YSZ film on Si substrate, B) After Photolithography Patterning on $SrRuO_3$+$SrTiO_3$+$SrRuO_3$+YSZ film on Si substrate, C) After Ion Beam Milling of $SrRuO_3$+$SrTiO_3$+$SrRuO_3$+YSZ film on Si substrate and D) After Photoresist Liftoff on $SrRuO_3$+$SrTiO_3$+$SrRuO_3$+YSZ film on Si substrate

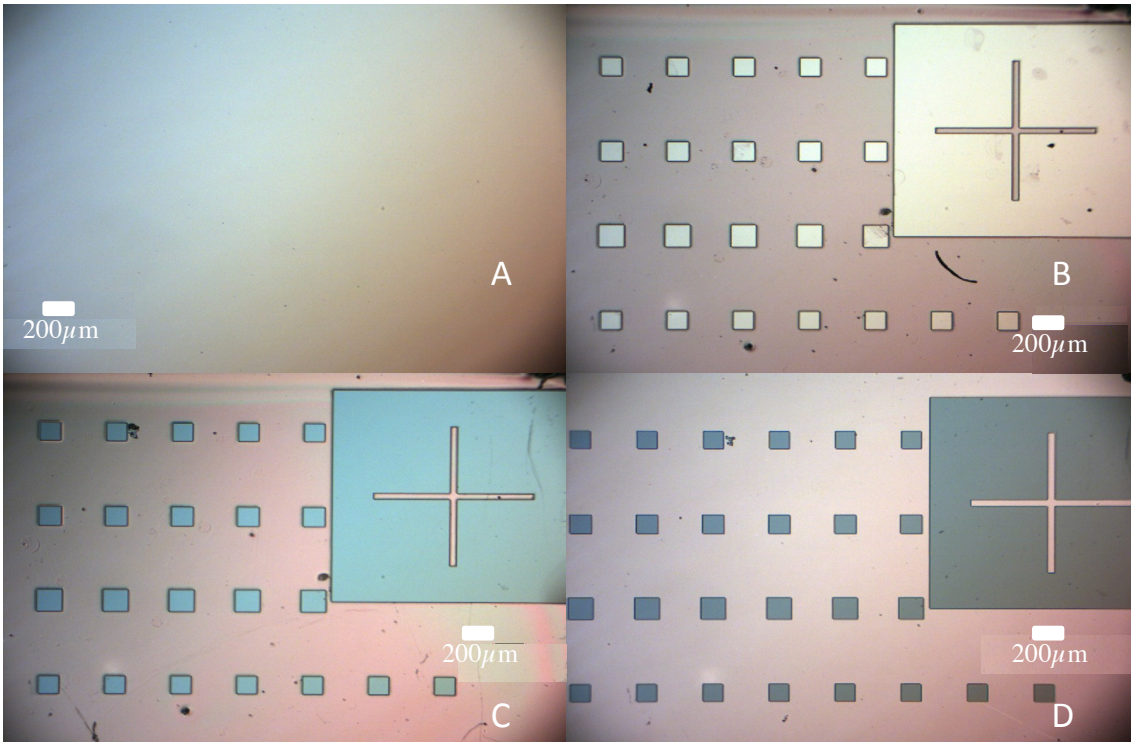


Figure 5.9. Microscopic image of the Silicon Substrate Backside patterning on the Silicon Substrate, A)Au+Ti Masking Layer Deposited on Si substrate, B) After Photolithography Patterning of Au+Ti Masking Layer on Si substrate, C) After Ion Beam Milling of Au+Ti Masking Layer on Si substrate and D) After Photoresist Liftoff on Au+Ti Masking Layer on Si substrate

The following parameters were used for the etch process of the metal oxide layers shown in Table 5.1.

Material	**Argon Gas Flow**	**RF Power**	**Accelerating Voltage**	**Screen Voltage**	**Ion Current**	**Etch Rate**
$SrRuO_3$	20sccm	70W	0.2kV	0.5kV	30mA	6.7nm/min
$SrTiO_3$	20sccm	70W	0.2kV	0.5kV	30mA	4.2nm/min

Table 5.1. The experimental parameters for etching the ferroelectric materials.

The bottom electrode thickness was increased to 300nm.[i] The final device structure was shown in Figure 5.10 and there were three different active area dimensions-20×20μm, 30×30μm and 50×50μm. The lithography patterning and ion beam milling process were performed for each layer of the multilayer structure. From the microscopic image in Figure 5.10, it has shown that photolithography patterning and ion beam milling process can

[i] Initially, the test structure was going to consist of 100nm thin $SrRuO_3$ electrodes, but its etch rate is faster than the etch rate of $SrTiO_3$ layer. From the mask pattern, there is no protection

introduce contaminants to the film surface, which can deteriorate the quality of the films in the multilayer structure.

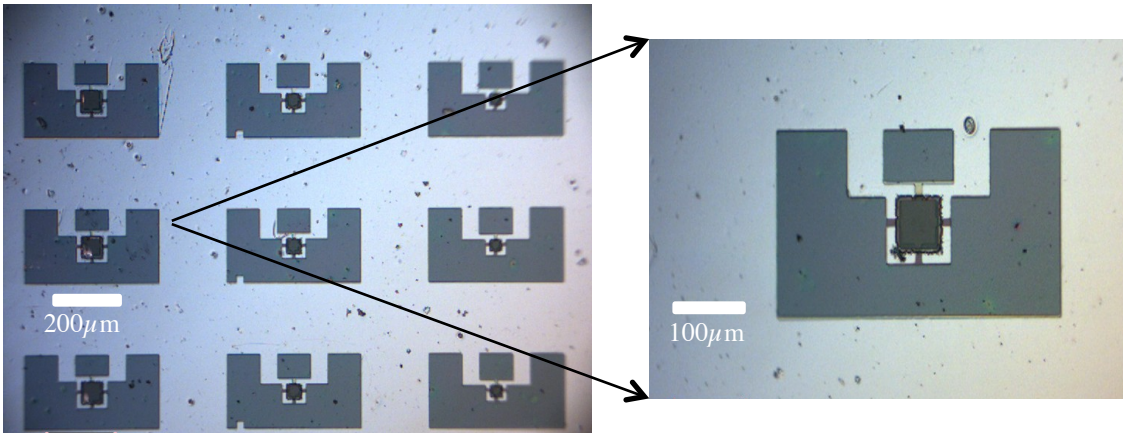


Figure 5.10. Microscopic image of the three different active area dimenisons(left) and final device structure 50×50μm after photolithography patterning and ion beam milling steps

After completing all these patterning steps illustrated in this subchapter, the multilayer resonator structure was still attached to the silicon substrate and the acoustic resonance induced within will become severely damped. Thus, the multilayer resonator structure must be selectively patterned and etched to fabricate a free standing on top of the silicon substrate.

5.3 Resonator device measurement results

In the previous subchapter, the tunability characteristics of the one stacking resonator device was investigated without selective substrate etching, so the tunability characteristics of the freestanding resonator at high frequency operation still remained a doubt. This one stacking multilayer resonator of SRO/STO/SRO was fabricated to experimentally confirm the theory of transforming electrical energy into acoustic vibrations in paraelectric state $SrTiO_3$ thin film, so the fabrication and testing of the electrically switchable bulk acoustic wave resonator employing two stacking structure have been moved to future works This section details the results of one multilayer stack of SRO/STO/SRO resonator device after selective substrate etching and its acoustic resonance measured through network analyzer technique.

The silicon substrate of the resonator device was selectively etched using the developed alternative deep silicon etching method in the reactive ion etcher with metal masks. Current-Voltage and Capacitance-Voltage measurement was carried out to determine the leakage current, dielectric constant and tunability of the resonator device after silicon substrate backside etching.

The dielectric constant of this $SrTiO_3$ film was approximated below by the following equation,

$$\varepsilon_r = \frac{C \times d}{A \varepsilon_0} \qquad (5.1)$$

where the ε_r is the dielectric constant, C is the measured capacitance, d is the thickness of the STO film,A is the area of the resonator device and $\varepsilon_0$is the electric constant(8.854×10^{-12}Fm^{-1}).

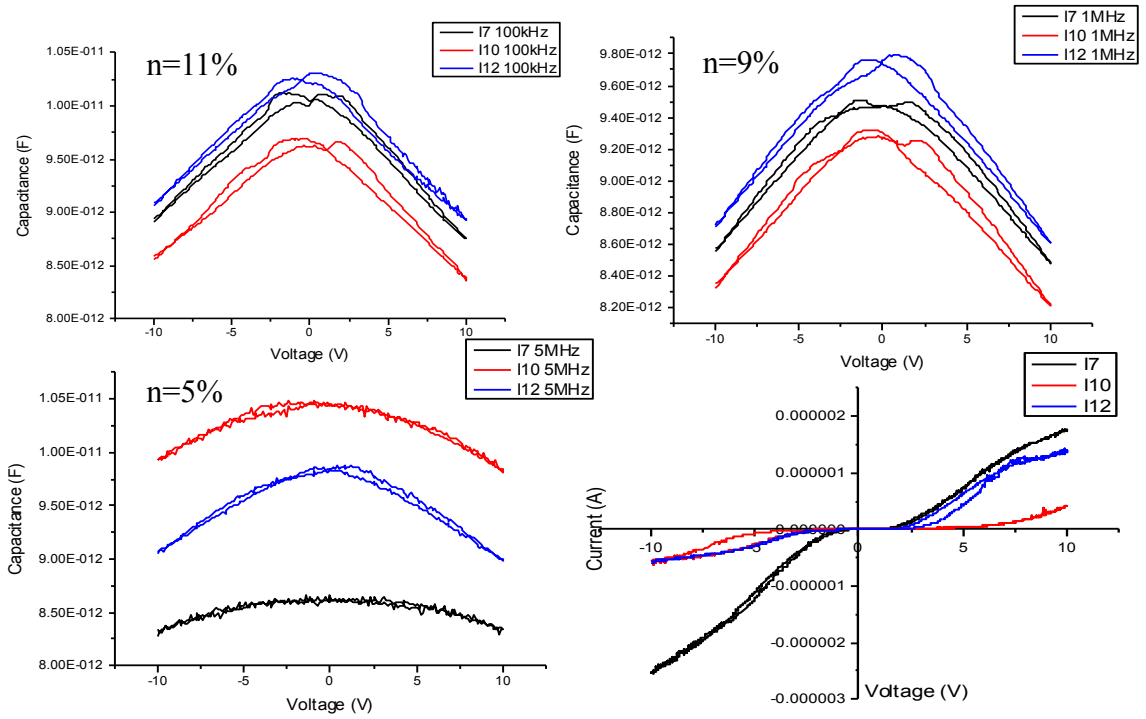


Figure 5.11. The Capacitance-Voltage and Current-Voltage Measurement at different frequencies for the entire resonator device after silicon substrate backside etching [ii]

The dielectric constant of the Strontium Titanate Oxide layer was calculated from the C-V curve using the equation 5.1 to be between 205 to 230. The dimension of the resonator device tested was 50×50μm and this was the largest out of the three different resonator dimensions. From Figure 5.11, the capacitance-voltage measurement demonstrated the tunability of the resonator device after the substrate backside etching at lower frequencies and the tunability is significantly decreased compared to the capacitance voltage measurement carried out before the etching process. This was possibly due to the decrease in active STO area due to device patterning and device side protection during backside etching. If the active area is reduced, the tunbility of the device is also likely to decrease. As the frequency increases, the number of domains and mechanisms available to become polarized also decreases.

[ii] The Legend I7, I10 and I12 are the number of the test resonator device located in the centre of all the different resonator devices fabricated on the 10×10mm wide Si substrate.

Figure 5.12 shows the one port microwave measurements of the characterization of the acoustic properties of the $SrTiO_3$ films in the tunable FBAR. By the application of 10V dc bias voltage to the resonator device, the resonance peak is observed at approximately 1.3GHz. This observation fits the modelling developed[1] on this switchable FBAR based on paraelectric state ferroelectric films. The detailed introduction of the modelling is shown in Appendix I.

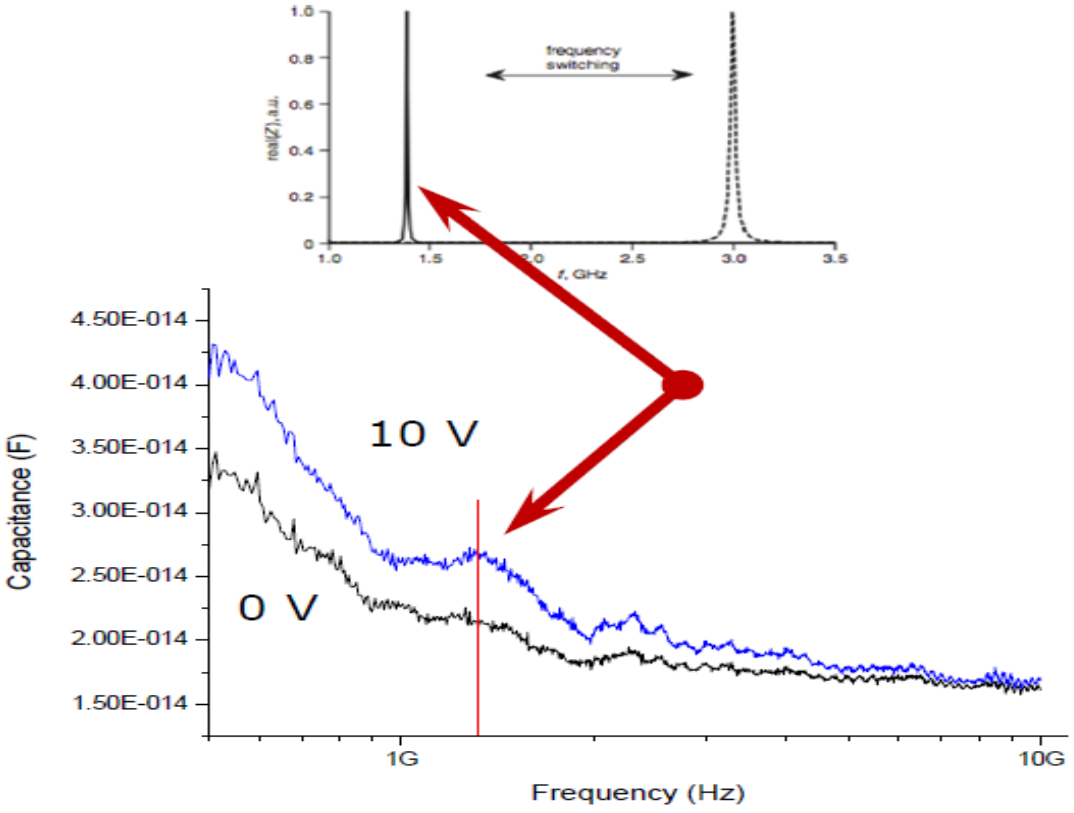


Figure 5.12. The Capacitance-Frequency measurement (bottom) from the one port reflection setup compared with the modelling (top)

The Figure 5.12 shows that the paraelectric state $SrTiO_3$ film being polarized by external applied DC bias and exhibit piezoelectric properties that can transform the electrical oscillations into acoustic waves when microwave signal is applied. Thus by switching the DC bias on and off, the piezoelectric coupling can be turned on and off. This transformation of electrical oscillations into acoustic waves were considered as the interaction between the electric field and the phonons(lattice vibrations) in an ideal crystalline lattice. The phonons can be viewed as weakly damped waves of atomic displacements and the interaction of an AC perturbation with them is related to the intrinsic losses of energy.

For our device, the field induced Quasi-Debye mechanisms can be used to explain the intrinsic losses of energy and transformation to acoustic waves through phonon interactions.

This mechanism is forbidden by the centrosymmetric materials and becomes active due to the breaking of central symmetry by the application of a DC bias field. Once quasi-Debye mechanism was activated, this contribution will dominate the intrinsic loss in the frequency range $\omega \leq 100GHz$, shown in Figure 5.13.

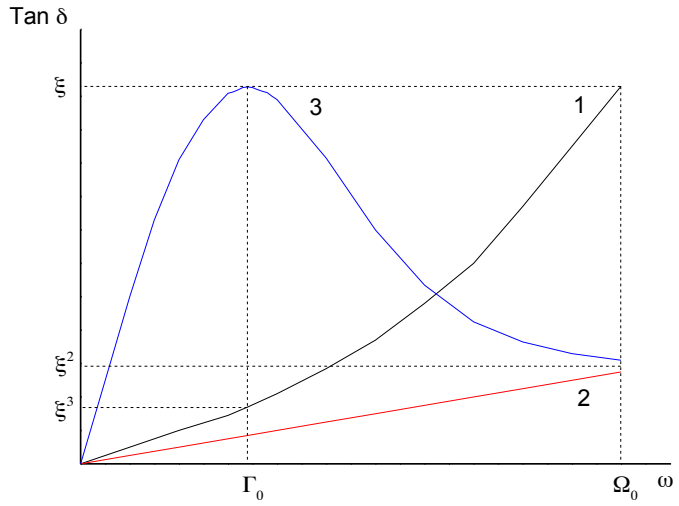


Figure 5.13. Results of phonon transport theory. The diagram shows the offscale plot of the frequency dependence of (1) three quantum, (2) four quantum and (3) quasi Debye contributions to the loss tangent due to the interaction of the ac electric field with the phonons of the soft mode of a displacive type ferroelectric. Ω_0 and Γ_0 are the soft mode frequency and damping, $\xi = \Gamma_0/\Omega_0$.The applicability range of the theory is $\Gamma_0 << \Omega_0$ and $\omega << \Omega_0$.

The phonon frequencies were linear functions of the electric field applied to the crystal in a non-centrosymmetric crystal, so the AC field perturbation can induces a deviation of the phonon distribution function from its equilibrium value. In the microwave frequency range, the field induced quasi-Debye contributions to the loss tangent is presented here,

$$\mathrm{Tan}\delta_{\mathrm{QD}}(\mathrm{E}_0) = \mathrm{AfI}(\mathrm{E}_0)\mathrm{T}_\varepsilon \qquad (5.2)$$

where T_ε is the relative tunability of dielectric permittivity under DC bias E_0. As the function of $I(E_0)$ approaches 1 in the limit of $T_\varepsilon \ll 1$, the parameter A is temperature dependent. For DC fields corresponding to small relative tunability T_s, the equation 5.2 suggests a quadratic field dependence of the DC field induced contributions to the loss tangent- $Tan\delta_{QD}(E_0)$. From theoretical estimates this dependence with experimental data for $SrTiO_3$ and $Ba_{0.6}Sr_{0.4}TiO_3$, the difference was mainly due to the strength of the flexoelectric coupling between the soft mode and acoustic branches. The non monotonic field dependence of the loss tangent in STO was related to the contribution of the acoustic phonon to the quasi-Debye loss, which is activated through flexoelectric coupling. This coupling was responsible for the

transformation of the AC field energy dissipiation into acoustic branches. In $Ba_{0.6}Sr_{0.4}TiO_3$, the flexoelectric coupling was much smaller and thus the contribution was relatively small. From these measurement results, it was shown that free standing resonator displays tunability and acoustic resonance at frequencies in agreement with the modelling predictions. Thus, the fabrication of this novel bulk acoustic resonator is successful and the modelling was proven correct with the measurement results.

5.4 Conclusions

This chapter presented the latest research and device characterisation results including device design, electrical characteristion, microwave measurements and modeling of the device. A free standing single stack of $SrRuO_3$ /$SrTiO_3$ /$SrRuO_3$ /YSZ (300nm /500nm/300nm/10nm) on high resistive Si substrate was examined. The tunability of this resonator was measured before selective substrate etching and after etching. The tunability of the resonator decreased significantly from 20% to 5% as the frequency was increased The high frequency measurements revealed also an acoustic resonance appears with application of 10V DC bias. The measured acoustic resonance frequency was in a good agreement with the frequency predicted by our modelling. Thus, proving the fabrication of this novel bulk acoustic wave resonator and modelling predictions were successful.

Chapter 6. Theory and Device Operation

The aim of this chapter is to explain the theory and device operation of the bulk acoustic wave resonator employing one stacking structure and the desired two stacking structure. The tunability of the serial and parallel resonance in the FBAR by applied electric field are shown and discussed.

6.1 Theory and Device Operation of One Stacking Structure

6.1.1 Introduction

FBAR resonators are devices typically based on piezoelectric thin films sandwiched between two electrodes and they resonates at a certain frequency of the applied ac signal depending on the acoustic velocity and the thickness of the different layers of the device. Piezoelectricity occurs in materials belonging to non-centrosymmetric point groups and materials belonging to centrosymmetric point groups often do not show piezoelectricity. However, all of these materials show electrostriction and the electrostrictive effect is a nonlinear coupling of elastic and electric fields.[151] If a dc electric field is applied to a centrosymmetric material, the symmetry of the material's crystal structure is broken and the material can be considered as a piezoelectric. Ferroelectric thin films in the paraelectric phase are suitable for frequency agile applications due to its dc bias dependent permittivity of materials and if a dc is applied to tune the permittivity of the material, the symmetry will be broken and piezoelectricity is induced. It was found that the dc bias induced resonance phenomenon depends on the applied dc electric field and is therefore tunable.[83] This phenomenon can be used to develop voltage controlled tunable resonators and filters.

The dc bias dependence of acoustic resonance in BST thin films was theoretically reported by Vendik et.al[152], where they derived the field dependent constitutive equations from the free energy D-expansion and the main contribution to the tuning of acoustic resonances was found to be due to the tensor of nonlinear electrostriction. The sign of the shifts of both resonance (Series) and antiresonance (Parallel) frequencies was determined by the sign of the corresponding tensor of nonlinear electrostriction.

In this chapter, the theory of field dependence of the acoustic resonances and the field dependent piezoelectric constitutive equations are presented. This theory is based on the Landau free energy P-expansion and takes linear and nonlinear electrostrictive effects and the background permittivity into account. The difference between series and parallel resonance

will be discussed. The device operation of the two stacking structure for electronically switchable bulk acoustic wave resonator will be presented.

6.1.2 Theory of field dependent acoustic resonances

The concept of this one stacking structure is fabricated to illustrate the possibility of utilizing paraelectric state ferroelectric materials in FBAR resonator application. The one stacking structure consists of two $SrRuO_3$ bottom and top electrodes sandwiching the one active $SrTiO_3$ layer. The active layer is response for the transformation from microwave power to acoustic power. The layout of the one stacking structure is shown in Figure 6.1.

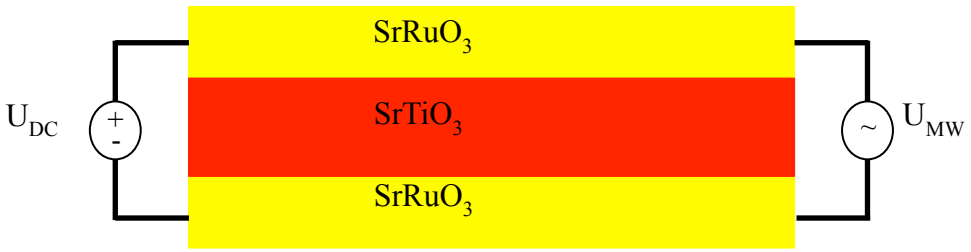


Figure 6.1. Layout of the one stacking structure for FBAR resonator

The electrostrictive strain, S in a dielectric material is a quadratic function of polarization, $S=QP^2$, where Q is the electrostriction coefficient. For a ferroelectric material, the polarization will consist of P_s (Spontaneous polarization), P_{DC} (DC field induced polarization) and P_{AC} (AC field induced polarization), $P=P_s+P_{DC}+P_{AC}$. Then, the resulting strain[153] is

$$S = QP_{DC}^2 + QP_{AC}^2 + QP_s^2 + (2QP_{DC})P_{AC} + 2QP_sP_{DC} + 2QP_sP_{AC} \quad (6.1)$$

The first term in the equation 6.1 is the constant strain caused by the DC field. The second term is the alternating electrostrictive strain associated with the AC field. When $P_{DC}=P_S=0$, this term responsible for the operation of the electrostrictive resonators. The third term is the spontaneous strain. The fourth term is the DC induced piezoelectric effect characterized by the DC dependent piezoelectric coefficient, $g_{DC}=2QP_{DC}$, and linear strain from the AC polarization. The fifth and last term represent static and alternating piezoelectric effects as linearized electrostriction where $2QP_s$ represents the piezoelectric voltage coefficient, $g=2QP_s$.

In paraelectric state ferroelectric material, the spontaneous polarization term is zero, thus the polarization are induced by DC and AC parts, so the resulting strain will be

$$S = QP_{DC}^2 + QP_{AC}^2 + 2QP_sP_{AC} \quad (6.2)$$

An externally applied DC field will polarize the ferroelectric and tune the acoustic parameters (e.g g_{DC}) of the material. The dielectric pretends to be a piezoelectric and the superimposed

AC field will transform the electrical power into acoustic waves. The induced piezoelectric effect and the associated acoustic waves can be "turned off" by removing the DC bias.

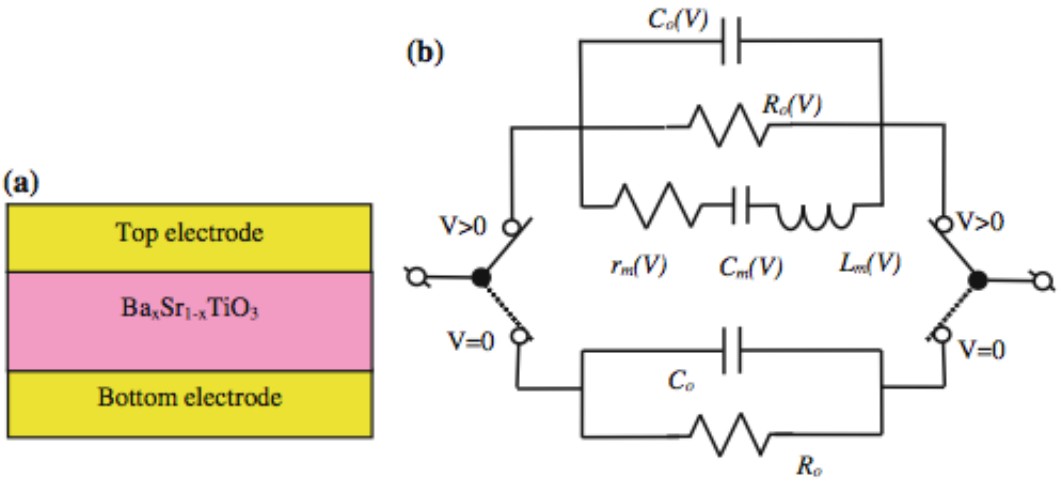


Figure 6.2. Simplified cross section (a) and two terminal equivalent circuit of a tunable FBAR as a frequency selective switch[153]

To excite the acoustic resonances in the thickness excitation mode, the geometry of a parallel plate capacitor in Figure 6.2 is considered. The acoustic resonances associated with a longitudinal acoustic wave travelling in the thickness direction (Cartesian X_3 axis). The following consideration is valid if a pure longitudinal acoustic wave is possible for this direction and this condition is met for epitaxial or textured cubic paraelectric material like STO. The film is considered to be clamped in the in-plane direction and free in the out of plane direction. The field dependent constitutive equations for the TE mode can be written as below[154]:

$$D_3 = \varepsilon_{33}E_3 + e_{33}u_3 \tag{6.3}$$

$$\sigma_3 = c_{33}^E u_3 - e_{33}E_3 \tag{6.4}$$

where $e_{33} = \chi_{33}^f$ and $c_{33}^E = c_{33}^0 - m_{333}\left(P_3^{dc}\right)^2 - h_{33}\chi_3^f h_{33}$.

The admittance Y(or impedance Z) can be derived through the mechanical wave equation, mechanical boundary conditions and the Poisson equation into account:

$$\frac{1}{Y(\omega)} = \frac{1}{i\omega C_0}\left(1 - k_t^2 \frac{Tan\frac{kt}{2}}{\frac{kt}{2}}\right) \tag{6.5}$$

where ω is the angular frequency, C_0 is the clamped capacitance, t is thickness of piezoelectric plate and k is the wave vector of the longitudinal wave. The wave vector k, elastic constant C^D and electromechanical coupling factor k_t^2 are:

$$k = \frac{\omega}{\sqrt{\frac{c_{33}^D}{\rho}}} \tag{6.6}$$

$$c_{33}^D = c_{33}^E + \frac{e_{33}^2}{\varepsilon_{33}} \tag{6.7}$$

$$k_t^2 = \frac{e_{33}^2}{c_{33}^D \varepsilon_{33}} \tag{6.8}$$

So the elastic constant at constant D can be expressed as,

$$c_{33}^D = c_{33}^0 (1 - \frac{m_{333}}{c_{33}^0} \left(P_3^{dc}\right)^2 - \frac{e_{33}^2 \varepsilon_{33}^b}{c_{33}^0 \chi_{33}^f \varepsilon_{33}}) \tag{6.9}$$

In the TE mode, the relations for the antiresonance f_{ares}(parallel) and the resonance frequency f_{res} (series) are given by,

$$f_{ares} = \frac{1}{2t} \sqrt{\frac{c_{33}^D}{\rho}} \tag{6.10}$$

$$f_{res} = \frac{1}{2\pi t} \sqrt{(\pi^2 - 8k_t^2) \frac{c_{33}^D}{\rho}} \tag{6.11}$$

By substitution, the field dependence of antiresonance frequency and the resonance frequency are,

$$f_{ares} = \frac{1}{2t} \sqrt{\frac{c_{33}^D}{\rho} \left(1 - \frac{m_{333}}{c_{33}^0} \left(P_3^{dc}\right)^2 - \frac{e_{33}^2 \varepsilon_{33}^b}{c_{33}^0 \chi_{33}^f \varepsilon_{33}}\right)} \tag{6.12}$$

$$f_{res} = \frac{1}{2\pi t} \sqrt{(\pi^2 - 8k_t^2) \frac{c_{33}^D}{\rho}} \tag{6.13}$$

In practical situations, the electromechanical coupling will be weak meaning the effect of the dc electric field on the elastic parameters of the system is small. Therefore the difference between c_{ij}^D or c_{ij}^E and c_{ij}^0 can be considered small as well. In this case, equation 6.12 and 6.13 can be simplified to,

$$f_{ares} = \frac{1}{2t} \sqrt{\frac{c_{33}^0}{\rho}} \left(1 - k_t^2 (\frac{m_{333} \varepsilon_{33}}{8 q_{33}^2 (\chi_{33}^f)^2} + \frac{\varepsilon_{33}^b}{2\chi_{33}^f})\right) \tag{6.14}$$

$$f_{res} = \frac{1}{2t} \sqrt{\frac{c_{33}^0}{\rho}} \left(1 - k_t^2 \left(\frac{m_{333} \varepsilon_{33}}{8 q_{33}^2 \left(\chi_{33}^f\right)^2} + \frac{\varepsilon_{33}^b}{2\chi_{33}^f}\right) - \frac{4}{\pi^2} k_t^2\right) \tag{6.15}$$

In case of high permittivity materials ($\varepsilon \approx \chi^f \gg \varepsilon^b$), the equations above can be further simplified to[154],

$$f_{ares} = \omega_0 (1 - k_t^2 \left(\gamma_t + \frac{\mu}{2}\right)) \tag{6.16}$$

$$f_{res} = \omega_0 (1 - k_t^2 \left(\gamma_t + \frac{\mu}{2}\right) - k_t^2 \frac{4}{\pi^2}) \tag{6.17}$$

where $\gamma_t \approx \frac{m_{333}}{8q_{33}^2\varepsilon_{33}}$,$\mu \approx \frac{\varepsilon_{33}^b}{\varepsilon_{33}}$,$f_0 = \frac{1}{2t}\sqrt{\frac{c_{33}^0}{\rho}}$ and $k_t^2 = \frac{4q_{33}^2\varepsilon_{33}}{c_{33}^0}(P^{dc})^2$.

The effect of the tuning dc field is introduced through the field dependent variables $\varepsilon_{33}(E^{dc})$ and $P^{dc}(E^{dc})$. These variable dependence can be either obtained from an independent experiment or be calculated from the following equations,

$$E_i^{dc} = \alpha_{ij}^* P_j^{dc} + \beta_{ijkl}^* P_j^{dc} P_k^{dc} P_l^{dc} \quad (6.18)$$

$$(\chi_{ij}^f)^{-1} = \alpha_{ij}^* + 3\beta_{ijkl}^* P_k^{dc} P_l^{dc} \quad (6.19)$$

The differences between $\varepsilon_{33}^f$and χ_{33}^fcan be neglected with the vectors E_i^{dc} and P_i^{dc} being set as $(00E^{dc})$ and $(00P^{dc})$.

6.1.3 Theory of field dependent piezoelectric constitutive equations

The field dependent piezoelectric constitutive equations are valid for the TE mode and ferroelectric material in paraelectric phase. The Landau free energy P-expansion is described in Equation 6.20[154],

$$F = \frac{\alpha_{ij}}{2}P_iP_j + \frac{\beta_{ijkl}}{4}P_iP_jP_kP_l + \frac{1}{2}c_{ijkl}^0 u_{ij}u_{kl} - q_{ijkl}u_{ij}P_kP_l - \frac{1}{2}m_{ijklmn}u_{ij}u_{kl}P_mP_n \quad (6.20)$$

where P_i is the ferroelectric part of polarization, β_{ijkl} is the tensor of the dielectric nonlinearity and c_{ijkl}^0,u_{ij},q_{ijkl} and m_{ijklmn} are the tensors of the elastic constant at constant P, strain, linear electrostriction and nonlinear electrostriction.

The tensor of component α_{ij} is given by:

$$\alpha_{ij} = (\chi_{ij}^{f_0})^{-1} \quad (6.21)$$

where $\chi_{ij}^{f_0}$is the ferroelectric contribution to the susceptibility of the material at zero bias.

The constitutive equations can be found through the following relations:

$$\frac{\partial F}{\partial P_i} = E_i \quad (6.22)$$

$$\frac{\partial F}{\partial u_{ij}} = \sigma_{ij} \quad (6.23)$$

$$D_i = \varepsilon^b E_i + P_i \quad (6.24)$$

where E_i is the electric field, σ_{ij} is the stress tensor and ε^b is the background permittivity. The background permittivity contains all non-ferroelectric contributions to the permittivity of the material. In ferroelectric materials, the relation $\frac{\varepsilon^b}{\varepsilon_0}$ is expected to be of the order of the relative permittivity in non-ferroelectric materials where ε_0 is the vacuum permittivity. In the case of a dc electric field E^{dc} superimposed with a relatively small ac electric field E^{ac}, all the variables of the problem is presented below:

$$E^{tot} = E^{dc} + E^{ac} \quad (6.25)$$

$$P^{tot} = P^{dc} + P^{ac} \quad (6.26)$$

$$\sigma^{tot} = \sigma^{dc} + \sigma^{ac} \quad (6.27)$$

$$u^{tot} = u^{dc} + u^{ac} \quad (6.28)$$

By linearize the constitutive equations 6.22 and 6.23 with respect to the ac components in equations 6.25 to 6.28, the field dependent piezoelectric constitutive equations can be derived:

$$E_i = (\chi_{ij}^f)^{-1} P_j - h_{ikl} u_{kl} \quad (6.29)$$

$$\sigma_{\mathrm{ij}} = c_{ijkl}^P u_{kl} - h_{kij} P_k \quad (6.30)$$

The polarization P^{dc} induced by the dc electric field can be presented as functions of piezoelectric tensor h_{ikl}, the ferroelectric contribution to the susceptibility of the material χ_{ij}^f and the tensor of elastic constant c_{ijkl}^P at constant P,

$$h_{ijk} = 2 q_{iskl} P_s^{dc} \quad (6.31)$$

$$c_{ijkl}^P = c_{ijkl}^0 - m_{ijklmn} P_m^{dc} P_n^{dc} \quad (6.32)$$

where c_{ijkl}^0 is the tensor of the electric constant of the material in the absence of the tuning electric field and in equations 6.31 and 6.32 only lower order terms in P^{dc} were kept.

The polarization induced by the dc field P^{dc} and the ferroelectric contribution to the susceptibility of the material χ_{ij}^f loaded with this electric field can be found from the equation 6.22 and 6.23 through eliminating the elastic variables.

By changing the set of variables from "$P, u \rightarrow E, \sigma$" to "$E, u \rightarrow D, \sigma$" to express the field dependent piezoelectric constitutive equations 6.29 and 6.30 in the standard form for TFBAR,

$$D_i = \varepsilon_{ij} E_j + e_{ijk} u_{jk} \quad (6.33)$$

$$\sigma_{ij} = c_{ijkl}^E u_{kl} - e_{ijk} E_k \quad (6.34)$$

where the tensor of the clamped permittivity ε_{ij}, the tensor of the elastic constant c_{ijkl}^E for constant E and the tensor of the piezoelectric coefficient e_{ijk} are given by the relations below.

$$\varepsilon_{ij} = \varepsilon_{ij}^b + \chi_{ij}^f \quad (6.35)$$

$$c_{ijkl}^E = c_{ijkl}^0 - m_{ijklmn} P_m^{dc} P_n^{dc} - h_{ijp} \chi_{pq}^f h_{qkl} \quad (6.36)$$

$$e_{ijk} = \chi_{is}^f h_{sjk} \quad (6.37)$$

6.1.4 Series and Parallel Resonance

The basic series and parallel resonant circuit is shown in Figure 6.3. The difference between them will be discussed and explained here in this section.

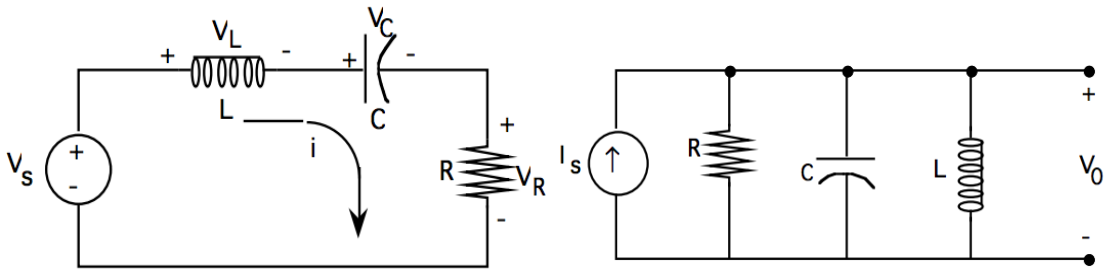


Figure 6.3 (a)The series resonant circuit diagram and (b) The parallel resonant circuit diagram[155]

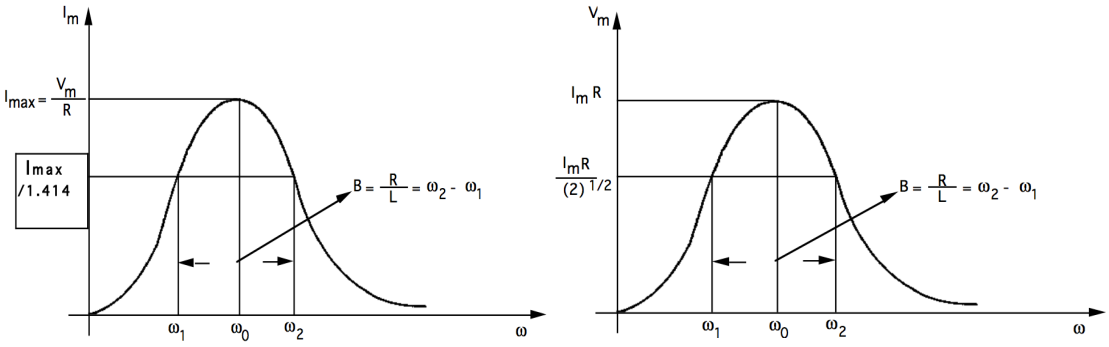


Figure 6.4 (a)The series frequency response and (b) The parallel frequency response[155]

For the series resonant circuit, as the frequency of the source changes, the maximum amplitude of the source voltage V_m is held constant. The variation of steady state amplitude and the phase angle of the current with the frequency of the sinusoidal voltage source is described the following equations[155],

$$V_s = V_m \cos(\omega t) \tag{6.38}$$

$$i = I_m \cos(\omega t + \theta) \tag{6.39}$$

The frequency at which the reactances of the inductance and the capacitance cancel each other out is the resonant frequency of this circuit and it occurs at

$$\omega_0 = \frac{1}{\sqrt{LC}} \tag{6.40}$$

Since $i = \frac{V_R}{R}$, the current i can be obtained by the voltage across the resistor. The current i has the following expression,

$$i = I_m \cos(\omega t + \theta) \tag{6.41}$$

where $I_m = \frac{V_m}{\sqrt{R^2 + (\omega L - \frac{1}{\omega C})^2}}$ and $\theta = -tan^{-1}(\frac{\omega L - \frac{1}{\omega C}}{R})$.

The bandwidth of the series circuit is defined as the range of frequencies in which the amplitude of the current is equal to or greater than ($\frac{1}{\sqrt{2}} = \frac{\sqrt{2}}{2}$) times its maximum amplitude as shown in Figure 6.4a. The bandwidth is

$$B = \omega_2 - \omega_1 = \frac{R}{L} \tag{6.42}$$

where $\omega_{2,1} = \sqrt{(\frac{R}{2L})^2 + \frac{1}{LC}} \pm \frac{R}{2L}$ is the half power frequencies or the 3dB frequencies, i.e the frequencies at which the value of I_m equals the maximum possible value divide by $\sqrt{2}$=1.414.

The quality factor is $$Q = \frac{\omega_0}{B} = \frac{1}{R}\sqrt{\frac{L}{C}} \tag{6.43}$$

For the parallel resonant circuit shown in Figure 6.3b, the steady state amplitude and the phase angle of the output voltage V_0 variation with the frequency of the sinusoidal voltage source can be expressed by the following,

$$I_s = I_m \cos(\omega t) \tag{6.44}$$

$$V_0 = V_m \cos(\omega t + \theta) \tag{6.45}$$

where $V_m = \frac{I_m}{\sqrt{\frac{1}{R^2} + (\omega C - \frac{1}{\omega L})^2}}$ and $\theta = -tan^{-1}(R\left(\omega C - \frac{1}{\omega L}\right))$.

The resonant frequency of the parallel resonant circuit is calculated by the same equation 6.40 for the series resonant circuit. The 3dB frequencies is calculated by following expression,

$$\omega_{2,1} = \sqrt{(\frac{1}{2RC})^2 + \frac{1}{LC}} \pm \frac{1}{2RC} \tag{6.46}$$

The bandwidth of the parallel resonant circuit is

$$B = \omega_2 - \omega_1 = \frac{1}{RC} \tag{6.47}$$

The quality factor of the parallel resonant circuit is

$$Q = \frac{\omega_0}{B} = R\sqrt{\frac{C}{L}} \tag{6.48}$$

From the above discussions, the series and parallel resonances of the FBAR device are demonstrated and explained.

6.2 Device Operation of Two Stacking Structure

The concept of this one stacking structure is fabricated to illustrate the possibility of utilizing paraelectric state ferroelectric materials in FBAR resonator application.

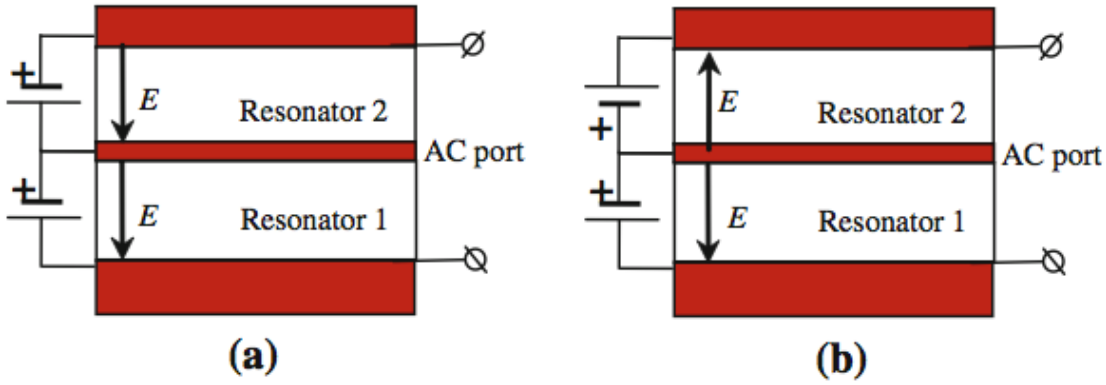


Figure 6.5. Layout of the two stacking structure for the electronically switchable FBAR resonator[153]

The field induced piezoelectric effect and the sign of field induced piezoelectric coefficient can be used to make a frequency switchable FBARs. This device consists of two mechanically coupled multilayer stacks employing paraelectric phase ferroelectric materials. The signs of the field induced piezoelectric coefficient (e_{33}) in each layer are controlled by the orientation of the DC bias induced polarizations. If the signs are the same in both ferroelectric layers in Figure 6.5a, the device acts as a simple FBAR. In this case, the resonant frequency of the first harmonic is defined by the total thickness of the stacked structure. However, if the signs are opposite in the ferroelectric layers in Figure 6.5b, the first harmonic of the stacked structure is suppressed and the resonant frequency of the second harmonic is defined by the thickness of a single layer which, is the first acoustic harmonic of the single layer FBAR. Thus, switching is possible by changing the polarity of the DC bias voltage.

6.3 Conclusion

To summarize, the field dependence of dc bias induced acoustic resonance phenomenon from the Landau free energy expansion respect to the ferroelectric contribution to the polarization and the tuning of the acoustic frequnecies for thickness excitation modes have been derived. The theory of the series and parallel resonance have been discussed briefly. The device operation of the desired two stacking electronically switchable FBAR have also been demonstrated.

Chapter 7. Conclusion and Future Works

This thesis explored the fabrication and characterization of a ferroelectric based MEMS structure for an electrically tunable thin film bulk acoustic wave resonator. The epitaxial film growth of the paraelectric state $SrTiO_3$ thin film on $SrRuO_3$ electrode with YSZ buffer layer on high resistive Si substrate by PLD was crucial to good device performance at microwave frequency. The increased number of required patterning steps after each film deposition can cause contamination on the device surface. A new alternative silicon etching technique was developed to selective etch through the silicon substrate and create a free standing tunable thin film BAW resonator on Si substrate. The development of this technique has overcome the difficulty regarding the integration of ferroelectric based tunable FBARs into standard silicon integrated circuits. Thus succesfully fabricating a tunable BAW resonator employing single multilayer structure consisting of epitaxial grown $SrRuO_3/SrTiO_3/SrRuO_3$/YSZ on the silicon substrate require experimental reproducibility and accuracy.

This novel type of tunable thin film bulk acoustic wave resonator employing one stack multilayer structure was fabricated to experimentally prove the model. By utilizing the intrinsically induced piezoelectric effect by the dc biasd electric field in the tunable paraelectric phase $SrTiO_3$ in a TFBAR, the transformation of the electrical oscillations into acoustic waves was investigated. 500nm thick STO active layer resonator device of area 50×50μm demonstrated decreasing tunability from 20% to 5% as the frequency is increased. The acoustic resonance was detected at the 1.37GHz frequency with application of 10V, which is accurately matched with the modelling results and proves the concept of a bulk acoustic wave resonator using paraelectric state $SrTiO_3$ films.

Further work should be focused on fabricating an electronically switchable bulk acoustic wave resonator employing two stacking multilayer structure of SRO/STO/SRO and experimentally confirming the theoretical modelling. Also, further efforts need to be put on improving the interface roughness of each layers in the multilayer structure which limits the Q factor of the STO resonators. This can be improved by performing all of the experimental work under clean room conditions.

References

1. A.B.Kozyrev;A.K.Mikhaylov;S.V.Ptashnik;S.V.Zinoviev;P.K.Petrov;N.M.Alford;T.Wang, *Electronically switchable bulk acoustic wave resonator based on paraelectric state ferroelectric films.* Electronics Letters, 2011. **47**(24): p. 1326-1327.
2. J.Valasek, *Piezoelectric and Allied phenomena in Rochelle Salt.* Physical Review, 1921. **17**(4): p. 475-481.
3. M.T.Sebastian, *Dielectric Materials For Wireless Communications*. 2008: Elsevier. p.1-688.
4. W.D.Kingergy;H.K.Bowen;D.R.Uhlman, *Introduction to Ceramics*. 1960: John Wiley and Sons. p.1- 1056.
5. H.Campanella, *Acoustic Wave and Electromechanical Resonators-concept to key applications*. 2010: Artech House. p. 1-363.
6. M.J.Lancaster;J.Powe;A.Porch, *Thin film ferroelectric microwave devices.* IEEE transactions on applied superconductivity, 1998. **11**(11): p. 1323-1334.
7. G.Rupprecht;R.Bell;B.D.Silverman, *Nonlinearity and Microwave Losses in Cubic Strontium Titanate.* Physical Review, 1961. **123**(1): p. 97-98.
8. A.F.Devonshire, *Theory of barium titanate.* Philosophical Magzine Series 7, 1949. **40**(309): p. 1040-1063.
9. L.D.Landau, *On the Theory of Phase Transitions II.* Phys.Z.Sowjet 1937. **11**(26): p. 26-545.
10. Z.G.Ban;S.Alpay, *Phase diagrams and dielectric responses of epitaxial barium strontium titanate films: a theoretical analysis.* Journal of Applied Physics, 2002. **91**(11): p. 9288-9296.
11. G.Rupprecht;R.Bell, *Dielectric Constant in Paraelectric Perovskite.* Physical Review, 1964. **135**(3): p. A748-A752.
12. K.A.Muller;H.Burkard, *SrTiO3:An Intrinsic quantum paraelectric below 4K.* Physical Review B(Condensed Matter), 1979. **19**(7): p. 3593-3602.
13. A.K.Tagantsev;V.O.Sherman;K.F.Astafiev;J.Venkatesh;N.Setter, *Ferroelectric Materials for Microwave Tunable Applications.* Journal of Electroceramics, 2003. **11**(1-2): p. 5-66.
14. DoITPoMS. *Variation of the dielectric constant in alternating fields*. Available from: http://www.doitpoms.ac.uk/tlplib/dielectrics/variation.php.
15. L.J.Sinnamon;R.M.Bowman;J.M.Gregg, *Investigation of dead layer thickness in SrRuO3/Ba0.5Sr0.5TiO3/Au thin film capacitors.* Applied Physics Letters, 2001. **78**(12): p. 1724-1726.
16. C.Basceri;S.K.Streiffer;A.I.Kingon;R.Waser, *The dielectric response as a function of temperature and film thickness of fiber textured (Ba,Sr)TiO3 thin films grown by chemical vapour deposition.* Journal of Applied Physics, 1997. **82**(5): p. 2497-2504.
17. V.Gurevich;A.Tagantsev, *Intrinsic dielectric loss in crystals.* Advances in Physics, 1991. **40**(6): p. 142-151.
18. O.Vendik;L.Ter-Martirosyan;S.Zubko, *Microwave losses in incipient ferroelectrics as functions of the temperature and the biasing field.* Journal of Applied Physics, 1998. **84**(2): p. 993-998.
19. O.Vendik;A.Rogachev, *Electrostriction mechanism of microwave losses in a ferroelectric film and experimental confirmation.* Technical Physics Letters, 1999. **25**(9): p. 702-704.
20. B.York, *Tunable Dielectric for RF circuits.* Multifunctional Adaptive Microwave Cirucits and Systems, 2006: p. 1-54.
21. S.Gevorgian, *Ferroelectrics in Microwave Devices,Circuits and Systems*. 2009: Springer. p.1-390.
22. L.B.Kong;S.Li;T.S.Zhang;J.W.Zhai;F.Y.C.Boey;J.Ma, *Electrically tunable dielectric materials and strategies to improve their performances.* Progress in Materials Science, 2010. **55**(8): p. 840-893.
23. S.Trolier-Mckinstry;P.Muralt, *Thin Film Piezoelectrics for MEMS.* Journal of Electroceramics, 2004. **12**: p. 7-17.
24. T.R.Sliker;D.A.Roberts, *A thin film CdS-quartz composite resonator.* Journal of Applied Physics, 1967. **38**(5): p. 2350-2358.
25. D.J.Page, *A cadmium sulfide silicon composite resonator.* Proceedings of the IEE, 1968: p. 1748-1749.

26. M.Hara;T.Yokoyama;M.Ueda;Y.Satoh, *X-band filters utilizing AlN thin film bulk acoustic resonators*, in *IEEE ultrasonics symposium*2007. p. 1152-1155.
27. T.Yokoyama;M.Hara;M.Ueda;Y.Satoh, *K-band ladder filters employing air gap type thin film bulk acoustic resonators*, in *IEEE International Ultrasonic Symposium*2008. p. 598-601.
28. J.F.Rosenbaum, *Bulk Acoustic Wave Theory and Devices*. 1988: Artech House. p. 1-480.
29. J.G.Gualtieri;J.A.Kosiniski;A.Ballato, *Piezoelectric materials for acoustic wave applications.* IEEE transactions on Ultrasonics,Ferroelectrics and Frequency Control, 1994. **1**(41): p. 53-59.
30. W.Pang;H.Zhang;H.Yu;C.Y.Lee;E.S.Kim, *Electrical frequency tuning of film bulk acoustic resonator.* Journal of Microelectromechanical systems, 2007. **16**(6): p. 1303-1313.
31. H.Yu;W.Pang;H.Zhang;E.S.Kim, *Film Bulk Acoustic Resonator at 4.4 GHz with Ultra Low temperature coefficient of resonance frequency*, in *18th IEEE International conference on Micro-Electro-Mechanical Systems*2005. p. 28-31.
32. J.Berge;S.Gevorgian, *Tunable bulk acoustic wave resonators based on Ba0.25Sr0.75TiO3 thin films and a HFO2/SiO2 Bragg reflector.* IEEE transactions Ultasonic,Ferroelectric,Frequency Control, 2011. **58**(12): p. 2768-2771.
33. S.Salgar;G.Kim;D-H.Han;B.Kim, *Modelling and Simulation of the Thin film bulk acoustic wave resonator*, in *IEEE International Frequency Control Symposium and PDA Exhibition*2002. p. 40-43.
34. M.Norton, *Fundamentals of Noise and Vibration Analysis for Engineers*. 1989: Cambridge University Press. p. 1-652.
35. M.Ueda;Y.Satoh, *FBAR and SAW technologies and their application for mobile communications*, in *Asia-Pacific Microwave Conference Workshops and Short Courses Digest*2006. p. 209-212.
36. R.Aigner, *MEMS in RF filter applications: Thin Film Bulk Acoustic Wave Technology.* Wiley InterScience:Sensors Update, 2003. **12**: p. 175-210.
37. X.H.Zhu;J.M.Zhu;S.H.Zhou;Z.G.Liu;N.B.Ming;S.G.Lu;H.L.W.Chan;C.L.Choy, *Recent progress of (Ba,Sr)TiO3 thin films for tunable microwave devices.* Journal of Electronic Materials, 2003. **32**(10): p. 1125-1134.
38. A.B.Kozyrev;E.K.Hollmann;A.V.Ivanov;O.I.Soldatenkov, *Microwave properties of YBa2Cu3O7-x/SrTiO3 Planar Capacitors.* Integrated Ferroelectrics, 1997. **17**(1-4): p. 257-262.
39. D.Galt;J.C.Pricel;J.A.Beall;T.E.Harvey, *Ferroelectric thin film characterization using superconducting microstrip resonators.* IEEE transactions on applied superconductivity, 1995. **5**(2): p. 2575-2578.
40. P.K.Petrov;E.F.Carlsson;P.Larsson;M.Friesel;Z.G.Ivanonv, *Improved SrTiO3 multilayers for microwave application:Growth and properties.* Journal of Applied Physics, 1998. **84**(6): p. 3134-3140.
41. P.M.Suherman;T.J.Jackson;Y.Y.Tse;I.P.Jones;R.I.Chakalova;M.J.Lancaster;A.Porch, *Microwave properties of Ba0.5Sr0.5TiO3 thin film coplanar phase shifters.* Journal of Applied Physics, 2006. **99**(10): p. 104101-104101-7.
42. A.Tombak;F.T.Ayguavives;J.P.Maria;;G.T.Stauf;A.I.Kingon:A.Mortazawi, *Low voltage tunable barium strontium titanate thin film capacitors for RF and microwave applications.* IEEE MTT-S International Microwave Symposium Digest, 2000: p. 1345-1348.
43. S.Stemmer;R.A.York, G.N.S.D.S.B., *Strontium Titanate DC electric field switchable and tunable bulk acoustic wave solidly mounted resonator*, in *IEEE IMS 2008*2008. p. 1263-1266.
44. A.Volatier;E.Defay;M.Aid;A.N'hari;P.Ancey;B.Debus, *Switchable and tunable strontium titanate electrostrictive bulk acousitc wave resonator integrated with a Bragg mirror.* Applied Physics Letters, 2008. **92**(3): p. 032906-032906-3.
45. S.A.Sis;V.Lee;J.D.Philips;A.Mortazawi, *Intrinsically switchable thin film ferroelectric resonator*, in *IEEE IMS 2012*2012. p. 1-3.
46. B.Ivira;A.Reinhardt;E.Defay;M.Aid, *Integration of electrostrictive Ba0.7Sr0.3TiO3 thin films into bulk acoustic wave resonator for RF frequency tuning under DC bias.* IEEE international Frequency Control Symposium, 2008: p. 254-258.

47. J.Berge;M.Norling;A.Vorobiev;S.Gevorgian, *Tunable solidly mounted thin film bulk acoustic resonators based on BaxSr1-xTiO3 films.* IEEE Microwave Wireless Components Letters, 2007. **17**(9): p. 655-657.
48. S.Gevorgian;E.L.Kollberg, *Do we really need ferroelectrics in paraelectric phase only in electronically controlled microwave devices?* IEEE transactions on Microwave Theory and Techniques, 2001. **49**(11): p. 2117-2124.
49. S.Gevorgian;E.Carlsson;E.Wikborg;E.Kollberg, *Tunable microwave devices based on bulk and thin film ferroelectrics.* Integrated Ferroelectrics, 1998. **22**(1-4): p. 245-257.
50. J.H.Haeni;P.Irvin;W.Chang;R.Uecker;P.Reiche;Y.L.Li;S.Choudhury;W.Tian;M.E.Hawley;B. Craigo;A.K.Tagantsev;X.Q.Pan;S.K.Streiffer;L.Q.Chen;S.W.Kirchoefer;J.Levy;D.G.Schlom, *Room temperature ferroelectricity in strained SrTiO3.* Nature, 2004. **430**: p. 758-761.
51. S.Gevorgian;A.Vorobiev;T.Lewin, *Dc field and temperature dependent acoustic resonances in parallel plate capacitors based on SrTiO3 and Ba0.25Sr0.75TiO3 films:Experiment and Modelling.* Journal of Applied Physics, 2006. **99**(12): p. 124112-124112-11.
52. K.Morito;Y.Iwazaki;T.Suzuki;M.Fujimoto, *Electric field induced piezoelectric resonance in the micrometer to millimeter waveband in a thin film SrTiO3 capacitor.* Journal of Applied Physics, 2003. **94**(8): p. 5199-5205.
53. A.Vorobiev;P.Rundqvist;K.Khamchane;S.Gevorgian, *Microwave properties of SrTiO3/SrRuO3/CeO2/YSZ heterostructure on low resistivity silicon.* Journal of the European Ceramic Society, 2003. **23**(14): p. 2711-2715.
54. X.X.Xi;H.Li;A.A.Sirenko;I.A.Akimov;J.R.Fox;A.F.Clark;J.Hao, *Oxide thin films for tunable microwave devices.* Journal of Electroceramics, 2000. **4**: p. 393-405.
55. T.J.Jackson;I.P.Jones, *Nanoscale defects and microwave properties of (BaSr)TiO3 ferroelectric thin films.* Journal of Materials Science, 2009. **44**(19): p. 5288-5296.
56. S.Tappe;U.Bottger;R.Waser, *Electrostrictive resonances in Ba0.7Sr0.3TiO3 thin films at microwave frequencies.* Applied Physics Letters, 2004. **85**(4): p. 624-626.
57. J.Berge;M.Norling;A.Vorobiev;S.Gevorgian, *Field and temperature dependent parameters of the dc field induced resonances in BaxSr1−xTiO3 based tunable thin film bulk acoustic resonators.* Journal of Applied Physics, 2008. **103**(6): p. 064508-1-064508-8.
58. X.Zhu;J.D.Philips;A.Mortazawi, *A DC voltage dependent switchable thin film bulk wave acoustic resonator using ferroelectric thin film*, in *IEEE Microwave Symposium*2007. p. 671-674.
59. A.Noeth;T.Yamada;P.Muralt;A.K.Tagantsev;N.Setter, *Tunable thin film bulk acoustic wave resonator based on BaxSr1-xTiO3 thin film.* IEEE transactions on Ultrasonics,Ferroelectrics and Frequency Control, 2010. **57**(2): p. 379-385.
60. K.M.Lakin, *Thin film resonators and filters.* IEEE Ultrasonic Symposium, 1982: p. 895-906.
61. T.Grudkowski, *Fundamental Mode VHF/UHF Miniature Acoustic resonators and filters on Silicon.* Applied Physics Letters, 1980. **37**(993-995).
62. K.Nakamura;H.Sasaki;H.Shimizu. *A piezoelectric composite resonator consisting of a ZnO film on an anizotropically etched silicon substrate*. in *1st Symposium on Ultrasonics Electronics* 1980.
63. H.Satoh;Y.Ebata;H.Suzuki;C.Narahara. *An air gap type piezoelectric composite thin film resonator*. in *Proceedings of the Annual Symposium on Frequency Control*. 1985.
64. K.Yamanouchi;M.Oba, *New Air gap type piezoelectric composite thin film resonators*, in *Ultrasonics Symposium*1987. p. 415-418.
65. K.M.Lakin;G.R.Kline;R.S.Ketcham;J.T.Martin;K.T.McCarron. *Stacked crystal filters implemented with thin films*. in *Proceedings of the 43rd Annual Symposium on Frequency Control*. 1989.
66. jr, W.R.C., *Electromechanical Coupling Factors*, in *Piezoelectronic, Pyroelectric and Related Constants*, D.F.Nelson, Editor 1993, Springer. p. 10-12.
67. K.M.Lakin;K.T.McCarron;R.E.Rose, *Solidly mounted resonators and filters*, in *IEEE Ultrasonics Symposium*1995. p. 905-508.

68. K.M.Lakin;G.R.Kline;K.T.McCarron, *Development of miniature filters for wireless applications.* IEEE transactions on Microwave Theory and Techniques, 1995. **42**(12): p. 883-886.
69. X.Zhu;J.D.Philips;A.Mortazawi, *A DC voltage dependent switchable thin film bulk acoustic wave acoustic resonator using ferroelectric thin film*, in *IEEE Microwave Symposium*2007. p. 671-674.
70. W.P.Mason, *Piezoelectric Crystals and Their Applications to Ultrasonics*. 1950: D.Van Nostrand. p.1-508.
71. J.F.Rosenbaum, *Bulk Acoustic Wave Theory and Devices*. 1998: Artech House. p. 1-480.
72. D.Feld;R.Parker;R.Ruby, *A new formula for computing Q is warrented.* Ultrasonics Symposium, 2008: p. 431-436.
73. H.W.Bode, *Network Analysis and Feedback Amplifer Design*. 1945: Van Nostrad. p.1-530.
74. D.M.Pozar, *Microwave Engineering*. 1998: John Wiley&Sons. p.1-720.
75. *Radio Frequency Band Designations*. Available from: http://www.radioing.com/eengineer/bands.html.
76. A.G.Fox, *An Adjustable Waveguide Phase Changer.* Proceedings of the IRE, 1947. **35**(12): p. 1490-1498.
77. J.Uher;W.J.R.Hoefer, *Tunable microwave and millimeter wave band pass filters.* IEEE transactions on Microwave Theory and Techniques, 1991. **39**(4): p. 643-653.
78. R.E.Collin, *Foundations for Microwave Engineering*. 1992: McGraw-Hill. p. 1-944.
79. G.L.Matthaei;L.Young;E.M.T.Jones, *Microwave filters,impedance matching networks, and coupling structures*. 1980: Artech House. p. 1-1096.
80. I.C.Hunter;J.D.Rhodes, *Electronically tunable microwave bandpass filters.* IEEE transactions on Microwave Theory and Techniques, 1982. **82**(9): p. 1354-1360.
81. J.F.White, *High power p-i-n diode controlled, microwave transmission phase shifters.* IEEE transactions on Microwave Theory and Techniques, 1965. **13**: p. 233-242.
82. A.Vorobiev;P.Rundqvist;K.Khamchane;S.Gevorgian, *Silicon substrate integrated high Q-factor parallel plate ferroelectric varactors for microwave/millimeterwave applications.* Applied Physics Letters, 2003. **83**(15): p. 3144-3146.
83. N.Setter;D.Damjanovic;L.Eng;G.Fox;S.Gevorgian;S.Hong;A.Kingon;H.Kohlstedt;N.Y.Park; g.B.Stephenson;I.Stolitchnov;A.K.Taganstev;D.V.Taylor;T.Yamada;S.Streiffer, *Ferroelectric thin films:review of materials,properties and applications.* Journal of Applied Physics, 2006. **100**: p. 051606-1-051606-46.
84. J.Wang;Z.Ren;C.T.C.Nguyen, *1.156GHz self-aligned vibrating micromechnical disk resonator.* IEEE transactions Ultasonic,Ferroelectric,Frequency Control, 2004. **51**(12): p. 1607-1628.
85. S.Li;Y.Lin;Z.Ren;C.T.Nguyen, *Self-switching vibrating micromechanical filter bank*, in *IEEE Joint International Frequency Control/Precision time and time interval symposium*2005. p. 135-141.
86. J.Y.Park;Y.J.Yee;H.J.Nam;J.U.Bu, *Micromachined RF MEMS tunable capacitors using piezoelectric actuators*, in *IEEE MTT-S International Micorowave Symposium Digest*2001. p. 2111-2114.
87. T.K.K.Tsang;M.N.El-Gamal, *Microelectromechanical variable capacitors for RF applications*, in *45th Midwest Symposium on cirucits and systems*2002. p. I25-I28.
88. Jun-Bo.Yoon;C.T.C.Nguyen, *A high-Q tunable micromechanical capacitor with movable dielectric for RF applications.* Electron devices meeting technical digest, 2000: p. 489-492.
89. A.Dec;K.Suyama, *Micromachined electro-mechanically tunable capacitors and their applications to RF integrated cirucit.* IEEE transactions on Microwave Theory and Techniques, 1998. **46**(12): p. 2587-2596.
90. W.Sichak;H.Augenblick. *Tunable Waveguide Filters*. in *Proceedings of the IRE*. 1951.
91. F.A.Miranda;C.H.Muller;C.D.Cubbage;K.B.Bhasin;R.K.Singh;S.D.Harkness, *HTS/ferroelectric thin films for tunable microwave components.* IEEE transactions on applied superconductivity, 1995. **5**(2): p. 3191-3194.

92. Ltd, M.D.T.; Available from: http://www.microwavedevicetechnology.com.
93. S.Mahon;R.Aigner, *Bulk Acoustic Wave Devices-Why,How and Where They are going*, in *CS MANTECH conference*2007. p. 15-18.
94. Y.H.Song;S.J.Cho;C.K.Jung;I.S.Bae;J.H.Boo;S.Kim, *The structural and mechanical properties of Ti films fabricated by using RF Magnetron Sputtering.* Journal of the Korean Physical Society, 2007. **51**(3): p. 1152-1155.
95. S.Ayoub;L.Y.Beaulieu, *The surface morphology of thin Au films deposited on Si(001) substrates by sputter deposition.* Thin Solid Films, 2013. **534**: p. 54-61.
96. D.W.Hoffman;J.A.Thornton, *Internal stresses in titanium,nickel,molybdenum, and tantalum films deposited by cylindrical magnetron sputtering.* Journal of Vacumm Science and Technology, 1977. **14**(1): p. 164-168.
97. J.A.Thornton, *Influence of apparatus geometry and deposition conditions on the structure and topography of thick sputtered coatings.* Journal of Vacumm Science and Technology, 1974. **11**(4): p. 666-670.
98. M.Shimizu;M.Okaniwa;H.Fujisawa;H.Niu, *Ferroelectric properties of Pb(Zr,Ti)O3 thin films prepared by low temperature MOCVD using PbTiO3 seeds.* Journal of the European Ceramic Society, 2004. **24**(6): p. 1625-1628.
99. P.Bao;T.J.Jackson;X.Wang;M.J.Lancaster, *Barium strontium titanate thin film varactors for room temperature microwave device applications.* Journal of Physics D:applied physics, 2008. **41**(6): p. 1-21.
100. B.Schwartz;H.Robbins, *Chemical Etching of Silicon.* Journal of the electrochemical society, 1959. **106**(6): p. 505-508.
101. F.Laermer;K.Funk;M.Offenberg, *Bosch deep silicon etching:Improving uniformity and etch rate for advanced MEMs applications.* Micro Electro Mechanical Systems 12th IEE International Conference, 1999: p. 211-216.
102. R.S.Muller, *Etch rates for micromachining processing.* Journal of Microelectromechanical systems, 1996. **5**(4): p. 256-269.
103. G.T.A.Kovacs;K.E.Petersen. *Bulk micromachining of silicon*. in *Proceedings of IEEE*. 1998.
104. S.K.Ray;N.B.Chakraborti, *Rapid plasma etching of silicon, silicon dioxide and silicon nitride using microwave discharges.* Semiconductor Science Technology, 1993. **8**(4): p. 599-604.
105. M.Tsuji;A.Tanaka;Y.Nishimura, *Enhancement of etch rate by the addition of O2 and Ar in chemical dry etching of Si using a discharge flow of Ar/CF4 and CF4/O2 gas mixture.* Japanaese Journal of Applied Physics, 2001. **40**(1): p. 2440-2446.
106. Y.H.Lee;A.A.Bright, *Doping effects in reactive plasma etching of heavily doped silicon.* Applied Physics Letters, 1985. **46**(3): p. 260-262.
107. J.Kiihamaki;S.Franssila, *Deep silicon etching in inductively coupled plasma for MEMs.* Physica Scripta, 1999. **T79**: p. 250-254.
108. M.E.Stewart;M.J.Motala;J.Yao:L.B.Thompson;R.G.Nuzzo. *Unconventional methods for forming nanopatterns*. in *Proceedings of IMechE*. 2006.
109. J.W.Judy, *Microelectromechanical systems(MEMS):fabrication, design and applications.* Smart materials and Structures, 2001. **10**: p. 1115-1134.
110. M.J.Madou, *Fundamentals of Microfabrication:Science of Miniturization*, ed. Taylor&Francis. 2002. p.1-752.
111. S.A.Rosli;A.A.Aziz;H.A.Hamid. *Highly chemical reactive ion etching of silicon in CF4 containing plasmas*. in *ICSE*. 2006.
112. J.G.Goodberlet, *Patterning 100 nm features using deep-ultraviolet contact photolithography.* Applied Physics Letters, 2000. **76**(6): p. 667-669.
113. H.Miyajima, *High aspect ratio photolithography for MEMS applications.* Journal of Microelectromechanical systems, 1995. **4**(4): p. 220-229.
114. Milling, I.B. *About the Ion Beam Milling Process*. 2011; Available from: http://www.ionbeammilling.com/ABOUT_THE_ION_MILLING_PROCESS.
115. R.E.Lee, *Microfabrication by ion beam etching.* Journal of Vacumm Science and Technology, 1979. **16**(2): p. 164-170.

116. S.Somekh, *Introduction to ion and plasma etching.* Journal of Vacumm Science and Technology, 1976. **13**(5): p. 1003-1007.
117. P.G.Gloersen, *Ion-Beam Etching.* Journal of Vacumm Science and Technology, 1975. **12**(1): p. 28-35.
118. P.A.Alvi;V.S.Meel;K.Sarita;J.Akhtar;K.M.Lal;A.Azam;S.A.H.Naqvi, *A study on anisotropic etching of (100) silicon in aqueous KOH solution.* International Journal of Chemical Science, 2008. **6**(3): p. 1168-1176.
119. A.R.Clarke;C.N.Eberhardt, *Microscopy Techniques for Materials Science*, ed. Illustrated. 2002. p.1-424.
120. S.E.Aw;H.S.Tan;C.K.Ong, *Optical absorption measurements of band gap shrinkage in moderately and heavily doped silicon.* Journal of Physics:Condensed Matter, 1991. **3**(42): p. 8213-8223.
121. H.F.W.Dekkers;F.Duerinckx;J.Szlufcik;J.Nijs, *Silicon surface texturing by reactive ion etching.* Opto-Electronics Review, 2000. **8**(4): p. 311-316.
122. R.A.Falk. *Near IR absorption in heavily doped silicon*. in *Proceedings of the 26th ISTFA*. 2000.
123. G.Lawes, *Scanning electron microscopy and X-ray microanalysis:Analytical chemistry by open learning*. 1987: John Wiley&Sons. p. 1-122.
124. S.Franssila, *Introduction to Microfabrication*, ed. J. Wiley&Sons. 2010. p.1-534.
125. H.M.Luo;M.Jain;S.A.Baily;T.M.McCleskey;A.K.Burrell;E.Bauer;R.F.DePaula;P.C.Dowden; L.Civale;QX.Jia, *Structural and ferromagnetic properties of epitaxial SrRuO3 thin films obtained by polymer assisted deposition.* Journal of Physics Chemistry B, 2007. **111**: p. 7497-7500.
126. P.J.Grundy;G.A.Jones, *Electron Microscopy in the study of materials*. 1976: Edward Arnold Publishers Limited. p.1-186.
127. L.V.Azaroff, *X-Ray Diffraction*. 1974: McGraw Hill. p.1-664.
128. S.Franssila, *Introduction to Microfabrication*. 2004: Wiley&Sons. p.1-534.
129. N.Sugii;K.Takagi, *Changes in surface morphologies with pulsed laser deposition temperature for STO and BST70/30 thin films on PT electrodes.* Thin Solid Films, 1998. **323**(1-2): p. 63-67.
130. B.D.Cullity, *Elements of X-ray diffraction*. 1978: Addison Wesley Publishing Co.Inc. p.1-531.
131. L.C.Sengupta;S.Sengupta, *Novel ferroelectric materials for phased array antennas.* IEEE transactions on Ultrasonics,Ferroelectrics and Frequency Control, 1997. **44**(4): p. 792-797.
132. A.Ito;H.Masumoto;T.Goto, *Microstructure and Electrical Conductivity of Epitaxial SrRuO3 Thin Films. Prepared on (001), (110) and (111) SrTiO3 Substrates by Laser Ablation.* Materials Transactions, 2007. **48**(2): p. 227-233.
133. Instruments, V., *Dektak 150 Surface Profiler User's Manual*, 2009.
134. O.Vendik;S.Zubko;M.Nikolski, *Modeling and calculation of the capacitance of a planar capacitor containing a ferroelectric thin film.* Technical Physics, 1999. **44**(4): p. 349-355.
135. Dikin, D.A., *Correction factors for 4 point probe electrical measurements with finite size electrodes and material anisotropy: a finite element study.* Measurement Science and Technology, 2007. **18**: p. 2067-2073.
136. M.B.Heaney, *Electrical conductivity and resistivity*, in *The Measurement, Instrumentation and Sensors Handbook*, J.G.Webster, Editor. 2000, CRC Press LLC. p. 1332-1345.
137. Amorese, G., *LCR/Impedance Measurement Basics*. 1997 Back to Basics Seminar, ed. H. Packard. 1997. p.4.1-4.87.
138. Corp, A.T., *Impedance Measurement Handbook:A guide to measuremnt technology and techniques*. 2003: Agilent Technologies Corp. p.1-5.41.
139. S.H.Oh;C.Park, *Nanoscale characterization of interfacial reactions in SrRuO3 thin film on Si substrate.* Surface and interface analysis, 2001. **31**(8): p. 796-798.
140. J.C.Delgado;F.Sanchez;R.Aguiar;Y.Maniette;C.Ferrater;M.Varela, *ArF and KrF excimer laser deposition of Yttria-stabilized zirconia on Si(100).* Applied Physics Letters, 1995. **68**(8): p. 1048-1050.

141. A.Bardal;T.Matthee;J.Wecker;K.Samwer, *Initial stages of epitaxial growth of Y-stabilized ZrO2 thin films on a-SiOx/Si(001) substrates.* Journal of Applied Physics, 1994. **75**(6): p. 2902-2910.
142. S.J.Wang;S.Y.Xu;L.P.You;S.L.Lim;C.K.Ong, *Microstructural studies on a high quality YBa2Cu3O7-δ/YSZ/Si multilayer prepared by Pulsed laser deposition.* Superconductor Science and Technology, 2000. **13**: p. 362-367.
143. T.Hirai;K.Teramoto;H.Koike;K.Nagashima;Y.Tarui, *Initial stage of growth process of ceria, yttria-stabilized-zirconia and ceria zirconia mixture thin films on Si(001) surfaces.* Japanaese Journal of Applied Physics, 1997. **36**: p. 5253-5258.
144. K.Hashimoto, *RF bulk acoustic wave filters for communications*. 2009: Artech House. p.185-204.
145. J.M.Rondinelli;N.M.Caffrey;S.Sanvito;N.A.Spaldin, *Electronic properties of bulk and thin film SrRuO3:Search for the metal-insulator transition.* Physical Review B(Condensed Matter), 2008. **78**: p. 155107-1-155107-15.
146. H.N.Lee;S.Senz;A.Visinoiu;A.Pignolet;D.Hesse;U.Gosele, *Epitaxial growth of non-c-oriented ferroelectric SrBi2Ta2O9 thin films on Si(100) substrates.* Applied Physics A, 2000. **71**(1): p. 101-104.
147. A.Antons;J.B.Neaton;K.M.Rabe;D.Vanderbilt, *Tunability of the dielectric response of epitaxially strained SrTiO3 from first principles.* Physical Review B(Condensed Matter), 2005. **71**: p. 0241021-10.
148. J.Papapolymerou, S.C.Z.Z.K.C.A.H.a., *Electronically Tunable Ferroelectric Devices for Microwave Applications*. Microwave and Millimeter Wave Tecnologies from Photonic Bandgap Devices to Antenna and Applications, ed. I.Minin. 2010.
149. C.Chen;J.S.Horwitz, *Ferroelectric Thin Films for Microwave Device Applications*. Pulsed Laser Depositon of Thin Films: applications-LED growth of Functional Materials, ed. R.Eason. 2007. p.533-559.
150. S.Gevorgian;P.K.Petrov;S.Abadei;Z.Ivanov, *Strain Induced Ferroelectrosity in Epitaxial SrTiO3 Films.* Integrated Ferroelectrics, 2000. **33**(1-4): p. 311-321.
151. R.E.Newnham, *Electrostriction:Nonliear electromechanical coupling in solid dielectrics.* Journal of Physics Chemistry B, 1997. **101**: p. 10140-10150.
152. I.B.Vendik.et.al, *Modelling tunable bulk acoustic resonators based on induced piezoelectric effect in BTO and BSTO films.* Journal of Applied Physics, 2008. **103**(1): p. 014107-1-014107-6.
153. S.Gevorgian;A.K.Tagantsev;A.K.Vorobiev, *Tuneable Film Bulk Acoustic Wave Resonators*, ed. B.Derby. 2013: Springer. p. 1-238.
154. A.Noth, *Micromachined Tunable Devices Based on Silicon Integrated BSTO Thin Films:Concepts,Fabrication and Characterization*, 2009. p. 1-125.
155. P.Sannuti. *Series and Parallel Resonance*. 2004; Available from: http://www.ece.rutgers.edu/~psannuti/ece224/PEEII-Expt-1-07.pdf.

Appendix I.

Modeling of the Resonator Device

Numerical modeling of the piezoelectric characteristics of the STO TFBAR was performed to validate the acoustic phenonmenon within the resonator device. This modeling was based on solving the one dimensional case for longitudinal waves across the thickness of the structure. The relationship between the potential (φ) of the electric field and mechanical displacement (η) is solved through following classical electromechanical equations:

$$\tilde{n}^{D}\frac{\partial^2\eta}{\partial x^2} = \rho\frac{\partial^2\eta}{\partial t^2} \tag{8.1}$$

$$\frac{\partial}{\partial x}\left(-\varepsilon_0\varepsilon\frac{\partial\phi}{\partial x} + e\frac{\partial\eta}{\partial x}\right) = 0 \tag{8.2}$$

where $c^D = c + \frac{e^2}{\varepsilon_0\varepsilon}$ is the stiffness constant that takes into account the piezoelectric effect. The solutions for the equations above are,

$$\eta(x,t) = Ae^{j(\omega t+kx)} + Be^{j(\omega t-kx)} \tag{8.3}$$

$$\varphi(x,t) = \frac{e}{\varepsilon_0\varepsilon}\eta(x,t) - \frac{D(t)}{\varepsilon_0\varepsilon}x + b \tag{8.4}$$

where ω and k are frequency and wave vectors; D(t) is the homogeneous component of the electric inductions and b is the an arbitrary constant. The structure of the $\varphi(x,t)$ function shows that by applying a homogeneous microwave field to the ferroelectric films, an acoustic mode can be excited within the resonator.

The piezoelectric modulus(e) of the paraelectric state ferroelectric layers was non zero only in the presence of a constant electric field. The relationship between the electric field and the piezoelectric modulus can be established through the phenomenological theory of ferroelectric with second order phase transition, which is shown below,

$$e = 2\varepsilon_0\varepsilon G P_{DC} \tag{8.5}$$

where P_{DC} is the ferroelectric layer polarization induced by the electric field and $\varepsilon_0\varepsilon$ is the permittivity of the ferroelectric layer in the presence of the electric field.

$$\varepsilon_0\varepsilon = \left(\left(\varepsilon_0\varepsilon(0)\right)^{-1} + 3\beta P_{DC}^2\right)^{-1} \tag{8.6}$$

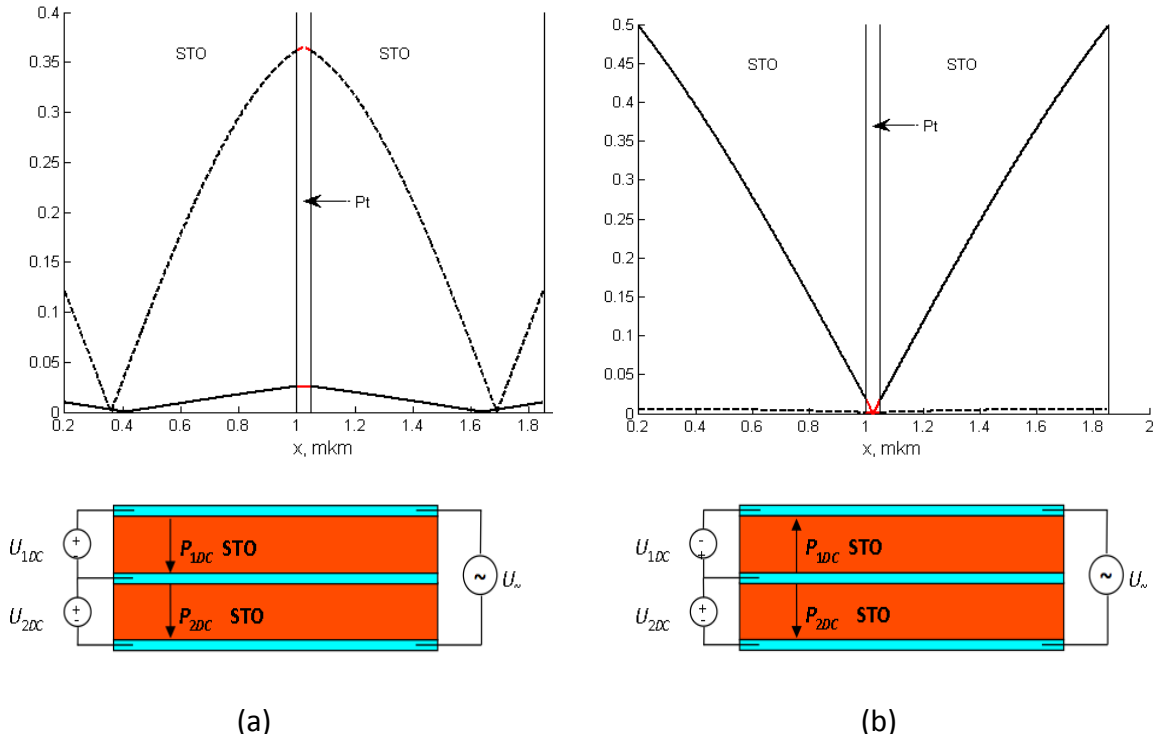
From the Equation 8.5, the sign of the piezoelectric modulus can be both the same and opposite due to different polarities of constant electric field applied to the ferroelectric layers. The calculation of the field of hypersonic displacements in a five layer resonator based on the solution of a system of equations describing the continuity of mechanical displacements(η)

and the mechanical stresses(σ) at the interfaces(x=x_j) between the adjacent layers, where i=1 to 5,

$$\eta_i(x_j) = \eta_{i+1}(x_j) \tag{8.7}$$

$$\sigma_i(x_j) = \sigma_{i+1}(x_j) \tag{8.8}$$

The numerical solutions to equations 8.7 and 8.8 determines the complex amplitudes of the acoustic waves in various parts of the five layer multilayer resonator structure.



(a) (b)

Figure 8.1. Profiles of the moduli of the standing waves of mechanical displacement amplitude η in a five layer acoustic resonator excited at the frequencies of mode 1 (f=1.37GHz solid line) and mode 2(f=2.96GHz dashed line) when the control fields in each ferroelectric layer are applied in the same (Figure 8.1a) and opposite directions (Figure 8.1b)

The results of the modeling calculations demonstrated the possibility to excite or suppress either symmetric or antisymmetric mode by changing the direction of E_{dc} field applied to each ferroelectric layer. Thus a multilayer structure that consists of at least two ferroelectric films in the paraelectric state can be considered a bulk acoustic wave (BAW) resonator with a switchable operating frequency.